1-1-1986

The magnetic and turbulent evolution of the Taurus Molecular Cloud.

Mark C. Hemeon-Heyer

University of Massachusetts Amherst
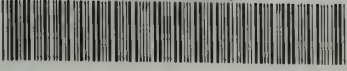
Follow this and additional works at: https://scholarworks.umass.edu/dissertations_1

The Magnetic and Turbulent Evolution of the Taurus Molecular Cloud

A Dissertation Presented

by

Mark C. Hemeon-Heyer

Submitted to the Graduate School of the
University of Massachusetts in partial fulfillment
of the requirements for the degree of

DOCTOR OF PHILOSOPHY

September, 1986

Department of Physics and Astronomy

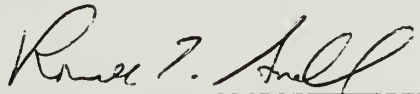The Magnetic and Turbulent Evolution of the Taurus Molecular Cloud

A Dissertation Presented
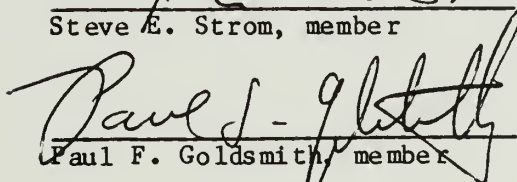
by

Mark C. Hemeon-Heyer

Appoved as to style and content by:

_____
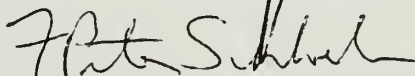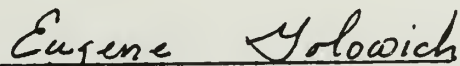Ronald L. Snell, Chairperson

_____
Steve E. Strom, member

_____
Paul F. Goldsmith, member

_____
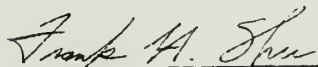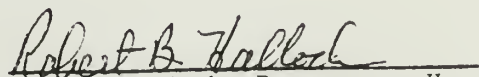F. Peter Schloerb, member

_____
Eugene Golowich, member

_____
Frank H. Shu, member

_____
Robert Hallock, Department Head
Department of Physics and Astronomy

ACKNOWLEDGMENTS

It is a pleasure and an honor to have been associated with the Five College Radio Astronomy Observatory. The dedication of its staff and administration has allowed scientists using the facility to think about science. In particular, I would like to acknowledge the proposal committee for the generous allotment of observing time required for this large scale project. In addition, I would like to express my eternal gratitude to Sally Rule for the repeated times in which she pulled me from the deathly grasp of the CPT printer and her efforts in untangling the bureaucratic webs.

Fred Vrba was responsible for obtaining the polarization measurements which made this dissertation unique and for whose efforts I grateful. Bob Dickman has provided me with insight into interstellar turbulence and the intricacies of the auto correlation function. Dan Clemens offered the basis for the separation of cloud cores described in Chapter III from his efforts to "bust" the Galactic Plane Survey. Phil Myers has provided many useful discussions with regards to cloud cores and star formation.

Graduate student existence becomes a metaphysical experience because of the friends and colleagues developed along the way who share the same wretched life but for some unexplained reason, love it. While it is impractical to list everyone here, it is possible to state that I have enjoyed the friendship and company of all of my fellow graduate students

ABSTRACT

The Magnetic and Turbulent Evolution of the Taurus Molecular Cloud

(September 1986)

Mark C. Hemeon-Heyer

B.S. Boston College

M.S., Ph.D., University of Massachusetts

Directed by: Ronald L. Snell

The role of the interstellar magnetic field in the dynamics of
molecular clouds is investigated from extensive mapping of the ^{13}CO
J=1-0 emission to delineate gas morphology and kinematics and
polarization of background starlight to determine the magnetic field
direction within the Taurus Molecular Cloud Complex. The signature for
a dynamically significant magnetic field is a rotating, flattened cloud
with the rotational and minor axes parallel to the direction of the
magnetic field. We find that molecular regions characterized by mean
densities less than 10^3 cm^{-3} exhibit such magnetic signatures and are
likely a result of magnetically dominated evolution.

A method to spatially and kinematically isolate the subcondensations
within the clouds is developed. These cores are characterized by mean
densities greater than 10^4 cm^{-3} and are the sites of star formation.
However, based on core morphology and kinematics, it appears the

magnetic field no longer provides a significant stress to the mostly neutral gas. Therefore, a constraint on the mean density at which the magnetic field decouples from the gas is a molecular density of less than 10^4 cm^{-3}.

The role of stellar winds from pre-main sequence stars as an internal energy source for molecular clouds is investigated from ^{12}CO and ^{13}CO mapping of star forming regions delineated by point sources of far infrared emission. Evidence for mass outflow is found toward three of the thirty sources surveyed. The outflows are dominated by red shifted emission. We also find from the ^{13}CO map of B18 evidence for large scale (> 1 pc) expansion based on the distribution of multiple velocity components in the observed spectra. The mean energy associated with stellar winds from pre-main sequence stars represent a significant fraction of the Taurus Cloud's internal energy and may provide the necessary mechanism to support the cloud long after the magnetic field has ceased to be the dominant support mechanism.

TABLE OF CONTENTS

LIST OF TABLES

LIST OF ILLUSTRATIONS

CHAPTER I.

PREVIEW

The formation of a star is the result of gas evolving from a diffuse interstellar cloud to the high densities required for thermonuclear fusion. However, the details of this evolution are still not well determined. While our understanding has been greatly broadened since the late 1960's with the advent of millimeter radio spectroscopy which has permitted the study of the dense gas phases of the interstellar medium, there remain several fundamental yet unanswered questions. Among these are:

1) what mechanisms provides support of the cloud against its own self gravity?

2) what is the lifetime of a molecular cloud?

3) what mechanism accounts for the broad velocity line widths of spectral lines which probe the molecular gas?

4) how is angular momentum of the cloud redistributed to account for the small values of stellar angular momentum observed?

5) how is the magnetic flux of the cloud redistributed to account for the values of surface stellar magnetic fields observed?

1

It is evident from earlier studies that molecular clouds are supported against self-gravitational forces by some as-yet-undetermined non-thermal pressure (Zuckerman and Evans 1974). Specifically, some have attributed prominent roles to the interstellar magnetic field and turbulence in the evolution of molecular clouds (Mouschovias 1976; Larson 1981). While it is difficult to interpret observations which directly probe the magnetic field, its influence upon the gas ought to leave an imprint upon the gas distribution and kinematics. Thus detailed observations of the gas properties supplemented by measurements of the magnetic field direction offer an indirect probe of the significance of the magnetic stress in these regions. While turbulent motion can account for some observed properties of molecular clouds, it is expected to be rapidly dissipated. Thus, if it is to be a significant factor in the evolution of a molecular cloud, an energy source is required to replenish the dissipated energy. One possible source present in these regions is the energy associated with stellar winds from recently formed young stars within the cloud.

To assess the relative importance of the magnetic field and turbulent motion in the dynamics of molecular clouds, we have undertaken a study of the star forming region in Taurus from extensive mapping of the molecular gas and the magnetic field direction, and a survey of young stellar objects within the cloud for the signatures of energetic mass outflow. In Chapter II, observations of the large scale gas distribution and kinematics and magnetic field geometry are presented.

The role of the magnetic field in the denser regions is investigated in Chapter III. In Chapter IV., we discuss our search for evidence of mass outflow associated with recently formed stars to determine the contribution of stellar winds to the energy budget of the molecular cloud.

CHAPTER II.

The Magnetic Evolution of the Taurus Molecular Cloud:
Large Scale Properties

INTRODUCTION

As astronomers probe the interstellar medium with increasingly
higher spatial resolution, molecular clouds reveal themselves to be
structures of extraordinary complexity. Such complexity is manifest in
both the clumpy nature of the clouds on all resolvable size scales and
in the chaotic motions of the gas inferred from molecular line widths.
While molecular clouds are possibly self-gravitating objects, the
gravitational force alone cannot account for these observed structures.
Essential to our understanding of the star formation process is the
determination of the relevant stresses in addition to gravity which
contribute to the evolution of a molecular cloud.

It was recognized over a decade ago that clouds must support
themselves against their own gravitational forces (Zuckerman and Evans
1974). Estimates of the lifetime of molecular clouds range from
10^7 years based on the ages of associated stellar clusters (Bash et al.
1977; Blitz and Shu 1980) to greater than 10^8 years from the formation
rates of massive cloud complexes due to collisional coalescence (Kwan
1979). Since the free fall time scale for a typical molecular cloud is
10^6 years, the cloud must be supported for at least ten free fall time

scales. Localized collapse of the cloud is possible, but the global equilibrium must be maintained. From observed average temperatures of molecular clouds (10 - 20 K), thermal pressure is unable to provide the necessary stress to support the cloud from self-gravitational forces except on the smallest size scales (Dickman and Clemens 1983; Myers 1983). The centrifugal stress due to rotation could be present but is generally not observed, or is dynamically insignificant on large size scales associated with molecular clouds (Arquilla and Goldsmith 1986).

It is observed that molecular clouds and their associated fragments are in approximate virial equilibrium (Larson 1981; Myers 1983). As a consequence, most models of molecular clouds have considered turbulent pressure as the primary means of support (Larson 1981; Fleck 1981). In the context of this picture, the observed suprathermal line widths are a signature of macroscopic motions of clumps which generally comprise the molecular cloud. The energy associated with such motions is comparable to the gravitational energy of the cloud itself. However, since these motions are supersonic ($\Delta v/c \sim 10$, c being the local sound speed) turbulence would be expected to dissipate rapidly as a result of clump collisions and the ensuing radiative energy losses (Zuckerman and Evans 1974). Hence, for turbulent motion to be dynamically important, its energy must be replenished at the same rate as it is dissipated. N-body calculations of interacting clumps show that most clump-clump collisions are oblique and presumably, non-radiative (Scalo and Pumphrey 1982). Thus the dissipation time scale is lengthened and the requirement of

energy sources is reduced. Several mechansims to power the turbulent motion have been proposed such as stellar winds, rotational shear, and gravitational torques although their coupling to the non-linear processes associated with turbulence is less well understood (Norman and Silk 1980; Fleck 1981; Henrikson and Turner 1984).

An alternative to the support of molecular clouds by turbulent pressure is the effective pressure provided by the interstellar magnetic field. This pressure is produced by the viscous tension derived from collisions between the ionic and neutral gas components of the cloud (Mestel and Spitzer 1956). The ion-neutral slip (ambipolar diffusion) creates a stress which slows the rate of collapse and contributes to the global cloud support of the cloud. The asymptotic result of ion-neutral slip is an accumulation of dense pockets of mostly neutral gas (cores) which are largely devoid of magnetic fields (Shu 1983). The cloud kinematics may also be subject to the interstellar magnetic field tension. Angular momentum is redistributed by coupling rotational motion of the cloud to the outer envelope via torsional Alfven waves. Such magnetic activity may be occurring within the globule B5 in which the inner core exhibits retrograde rotation with respect to the outer envelope (Young et al. 1982). In addition, the component of the angular momentum perpendicular to the magnetic field is more efficiently redistributed so that one is more likely to observe angular momentum parallel to the magnetic field direction if the field has not decoupled from the gas (Mouschovias and Paleologou 1981).

Both turbulent and magnetic stresses must be present at some level within a molecular cloud. The questions to address are (1) on what size scale does each stress play a dominant role, (2) is there a smooth transition (if there is one at all) between the two regimes where each dominate and (3) are the two stresses coupled to one another, that is turbulence driven by Alfvenic or magnetosonic disturbances. It is clear that the two stresses are fundamentally different. The magnetic field introduces an anisotropy into cloud morphology and gas motions (Mouschovias 1976). In contrast, turbulence is a stochastic process and expected to contribute isotropic disturbances to the cloud's configuration and gas motions (Kleiner and Dickman 1985).

Our knowledge of molecular clouds has been primarily based on the observations of bright, distant giant molecular clouds and coarsely sampled maps of nearby regions. More detailed studies of nearby individual molecular clouds can provide insight into the structure of less well resolved and more distant giant molecular clouds where most of the star formation takes place in the Galaxy. In particular, it is important to achieve spatial resolution less than 0.1 pc since such a scale denotes a Jeans' length in a typical star forming region.

We report here the results of a detailed study of the Taurus Molecular Cloud Complex to distinguish the roles, if any, that the interstellar magnetic field and turbulent stresses play in the evolution of the complex. The Taurus complex is a valuable cloud to study because it is one of the nearest star forming regions (140 pc), and is isolated

from the galactic plane emission (b=-15°). With the great improvement in millimeter receiver sensitivity, finely sampled maps of molecular clouds covering many square degrees are now possible. Such maps provide information of the detailed morphology and velocity structure over a wide range of size scales and allow one to determine systematic properties throughout the cloud. ^{13}CO J=1-0 emission in 17000 spectra was observed from the isolated clouds which make up the Taurus complex. The ^{13}CO J=1-0 transition was selected because it is readily detectable and the integrated intensity is a reasonably good linear tracer of gas column density.

In order to assess the role played by the magnetic field in cloud evolution, we have carried out polarization measurements of starlight from backgound or embedded stars (Vrba et al. 1976; Davis and Greenstein 1951). From the local direction of the magnetic field, anisotropy of cloud properties with respect to the field can be determined. In particular, the signature of the presence of a dynamically important magnetic field are (1) flattening of the clouds along the field lines and (2) alignment of rotational axes parallel to the magnetic field direction. Properties of the embedded subcondensations within the clouds and the role of stellar winds as a source of turbulent energy are discussed in later papers (Heyer 1986; Heyer et al. 1986).

OBSERVATIONS

a) ^{13}CO, C^{18}O, and HC$_3$N

All molecular line observations were obtained with the 14 meter telescope of the Five College Radio Astronomy Observatory. A quasi-optical sideband filter and a 256 channel spectrometer with 100 kHz resolution per channel were employed with a cryogenic Schottky diode mixer receiver. Calibration of the data was obtained using a chopper wheel which allowed for switching between the sky and an ambient load.

Measurements of the Moon and Jupiter were used to determine the half power beam width (θ_{FWHP}) and the efficiency on a spatially extended source (η_{FSS}) much larger than the main beam. At the rest frequencies of the carbon monoxide J=1-0 transitions of ^{13}CO (110.20137 GHz), and C^{18}O (109.78218 GHz), the values for θ_{FWHP} and η_{FSS} are 47" and 0.70 respectively. For the J=10-9 transition of HC$_3$N (rest frequency 90.9814 GHz), these values are 58" and 0.70. Temperatures (T_R^*) quoted in this study have been corrected for ambient temperature losses, effects of the Earth's atmosphere, and for forward spillover and scattering losses (η_{FSS}, Kutner and Ulich 1981). To determine the radiation temperature T_R, no further correction is required since the sources observed here fill the error pattern of the telescope.

The observations of the ^{13}CO J=1-0 emission in Heiles Cloud 2, L1517, and L1544 were taken by frequency switching. The maps of the B18 and B216-B217 regions were taken by position switching between the

source and a position absent of emission. For the position switched data, many scans share a single reference observation to reduce the overhead in time of position switching. While such reference sharing greatly increases the efficiency of mapping, changes in the atmospheric opacity between reference positions may introduce further calibration uncertainty. Such calibration errors are evident in the striping of these maps. A summary of the ^{13}CO observations is given in Table 1.

Additional observations of the $C^{18}O$ J=1-0 emission were made toward Heiles Cloud 2, L1517, L1544, and B18 where strong ^{13}CO emission was found to determine the optical depth of the ^{13}CO emission. The J=10-9 transition of the HC_3N molecule was observed toward L1517 and L1544 and the CS J=2-1 transition was observed toward L1517. These transitions have a large spontaneous decay rate and are expected to probe higher densities than those probed by CO. Comparison of the ^{13}CO and $C^{18}O$ emission with that of HC_3N and CS allows one to determine whether the CO emission is tracing regions of both enhanced column and space density.

b) Polarimetry

In order to sample the magnetic field geometry, we obtained measurements of stars located near the periphery of the B216-B217 and B18 clouds. The polarization measurements were made with the Vatican Polarimeter mounted at the Cassegrain focus of the 70 inch reflector of the Lowell Observatory in Flagstaff, AZ. The details of the Vatican Polarimeter are given by Magahles et al. (1984). The effective

Table 1

^{13}CO Observing Characteristics

Name	Observing Mode	No. of Spectra	Dates
Heiles Cloud 2	frequency switch	3600	1982
B216-B217	position switch	3700	1985
B18	position switch	7700	1984
L1517	frequency switch	1000	1982
L1544	frequency switch	1200	1982

Figure 1 - Outer contour of the ^{13}CO J=1-0 integrated intensity of

a) Heiles Cloud 2, b) B216-B217, c) B18, d) L1517, and

e) L1544. The positions of the embedded (triangle) and T

Tauri (square) stars are overlayed upon the maps of ^{13}CO

emission. Identification of the young stellar objects are

based on infrared colors from IRAS observations and

similarities to known objects of those types (Emerson 1985).
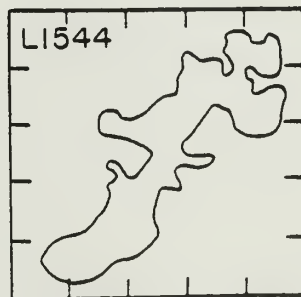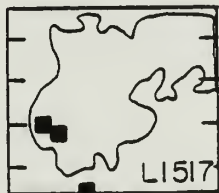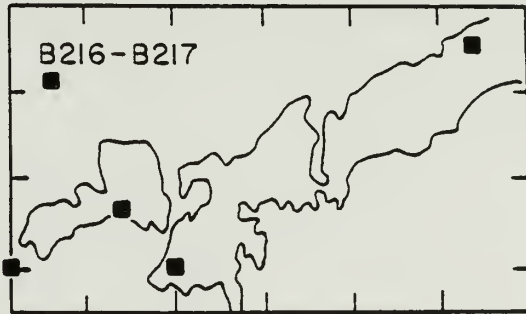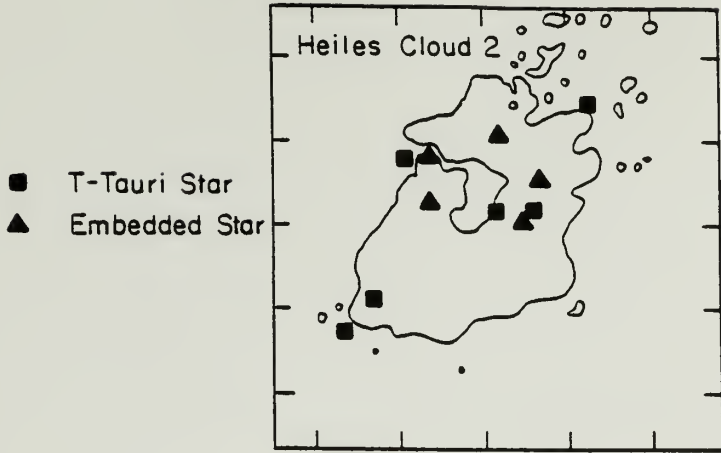
wavelength of these observations is set by the spectral energy distribution of the star and the unfiltered response of a GaAs photomultiplier. The stars observed were selected to have magnitudes, $M_R \sim 10$; and at a distance of the Taurus clouds, nearly all such objects should be background to the cloud. The absence of such objects in the opaque core regions of the clouds confirms this statistical expectation. The position, observed percent polarization, 1σ error, and position angle of the measure electric field vector, measured east from north, for each star are given in Tables 2 and 3.

RESULTS

Most star formation activity in the Taurus Cloud Complex occurs within the central region which is composed of several distinct clouds each containing several hundred solar masses (Heiles Cloud 2, B216-B217, and B18). The positions of T Tauri stars and embedded objects distinguished by far infrared spectra associated with the clouds studied here are given in Figure 1. (IRAS Point Source Catalog 1985; Emerson 1985).

a) Heiles Cloud 2

The gas associated with the Heiles Cloud 2 region has been studied previously by Schloerb and Snell (1984). The mass of Heiles Cloud 2 is estimated to be 645 M_O using an empirically determined relation between ^{13}CO integrated intensity and H_2 column density (see Appendix) and the data of Schloerb and Snell (1984). They proposed that the observed

morphology and kinematics are consistent with a rotating ring. The ring was interpreted by Schloerb and Snell (1984) to be tilted toward the observer. The orientation of the cloud, θ, defined by the direction of the minor axis measured East of North in the plane of the sky is 60°. The ringlike nature of Heiles Cloud 2 is reinforced by the detection of an associated velocity shear across the cloud indicative of rotation about an axis with a position angle also of 60°. The calculated velocity gradient is $0.8 \text{ km s}^{-1} \text{ pc}^{-1}$. The ring appears to be fragmenting as evidenced by regions of both increased column density (Schloerb and Snell 1984) and space density (Myers and Benson 1983; Cernicharo et al. 1984). Some of these fragments have evolved to form stars as indicated by the presence of six T Tauri stars and four highly obscured, embedded objects (Figure 1).

The magnetic field geometry of the Taurus complex has been studied by Moneti et al. (1984) and Hsu (1985) from visual polarization observations of bright stars. We have estimated a mean magnetic field direction described by the position angle $50^{\circ} \pm 30^{\circ}$ for the Heiles Cloud 2 region based on these earlier studies.

b) B216-B217

The region associated with B216 and B217 condensations form the southeast portion of a long filament which extends to L1495. Within the filament, there are three young stellar objects (DG Tau, HH31, and Haro6-5) which exhibit evidence for mass outflow and shock excited nebulosity (Mundt and Fried 1983; Strom et al. 1986). Previous

observations of molecular emission have suggested a systematic velocity gradient along the length of the filament (Clark and Johnson 1978). Localized regions exhibiting multiple velocity components are observed in the ^{13}CO spectral line and were interpreted as fragments along the line of sight in orbital motion (Clark, Giguerre, and Crutcher 1977).

We have mapped the ^{13}CO emission from the filament at 1' spacing. The image constructed from the intensities of 3700 spectra summed over the velocity interval 4 to 8.25 km s^{-1} is displayed in Figure 2. Comparison of the radio image with the Palomar Sky Survey red plate of the region and visual extinction maps (Cernicharo et al. 1985) indicate a high degree of correlation of morphological features. The estimate of the mass contained within the region observed is 190 M_0 using the relation between ^{13}CO integrated intensity and molecular hydrogen column density described in the Appendix. Although the filament extends well beyond the region mapped, evidence for clumpiness, perhaps indicative of fragmentation is readily seen along the major axis.

The velocity structure of the cloud is displayed in Figure 3 as a sequence of maps of the mean intensity within each of the velocity intervals. At low velocities, the emission is concentrated in the northwest portion of the map. At higher velocities, the emission centroid shifts to the southeast. A spatial velocity map (Figure 4) cut along the length of the filament denotes a shift in mean velocity between cores indicating that the inferred gradient is not continuous. At higher velocities (7.25 km s^{-1}), there remains weak emission in the

Figure 2 – A map of the ^{13}CO J=1-0 integrated intensity of the B216-B217

cloud over the velocity interval 4 to 8.25 km s^{-1}. The cloud

is composed of several fragments along the major axis and

extends to the northwest, well beyond the region mapped.
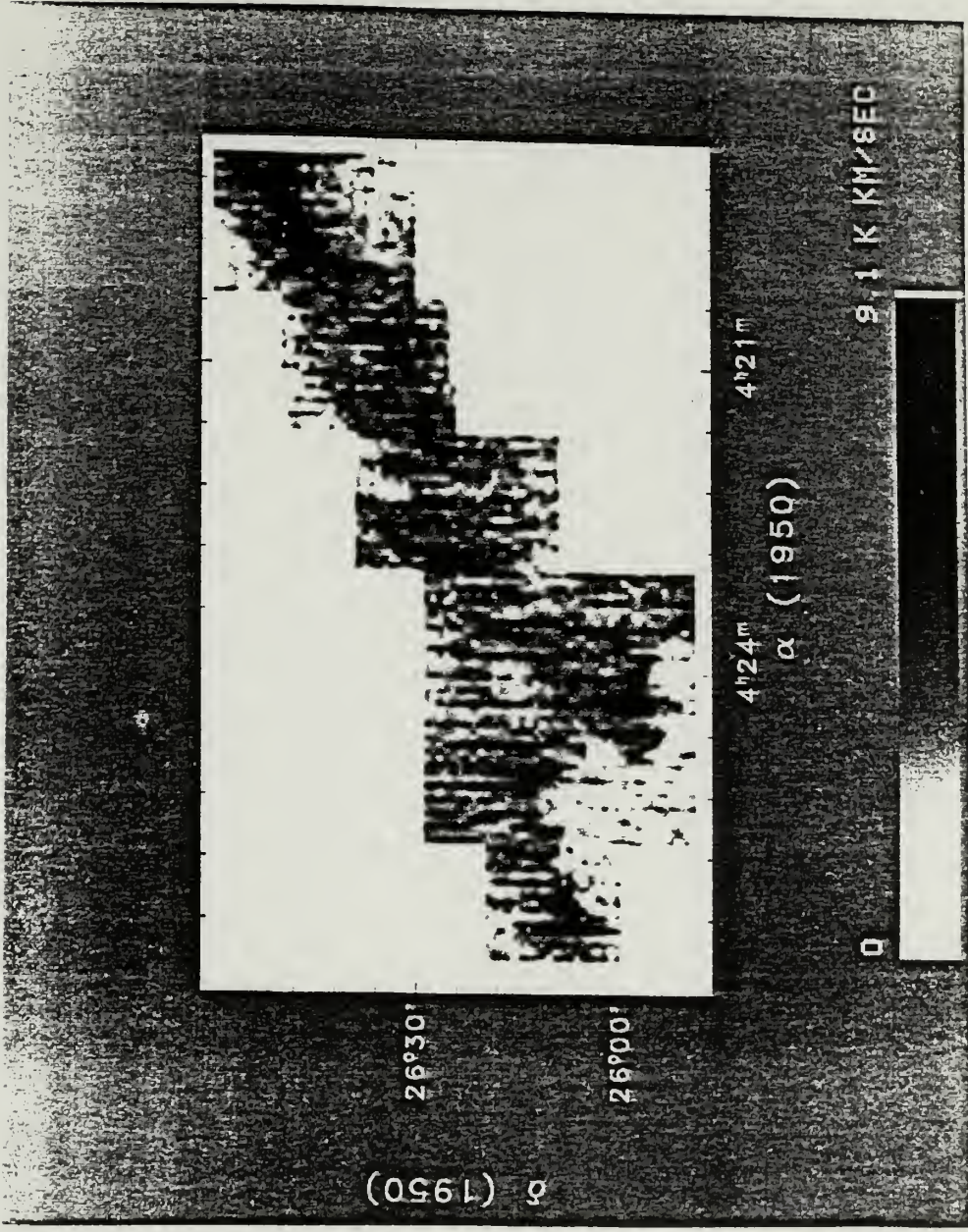
Figure 3 - A sequence of maps of the mean ^{13}CO J=1-0 intensity within

each velocity interval demonstrating the large scale velocity

structure of B216-B217. Rotation of the cloud is indicated

by the shift of the emission centroid from the northwest at

low velocities to the southeast at higher velocities.
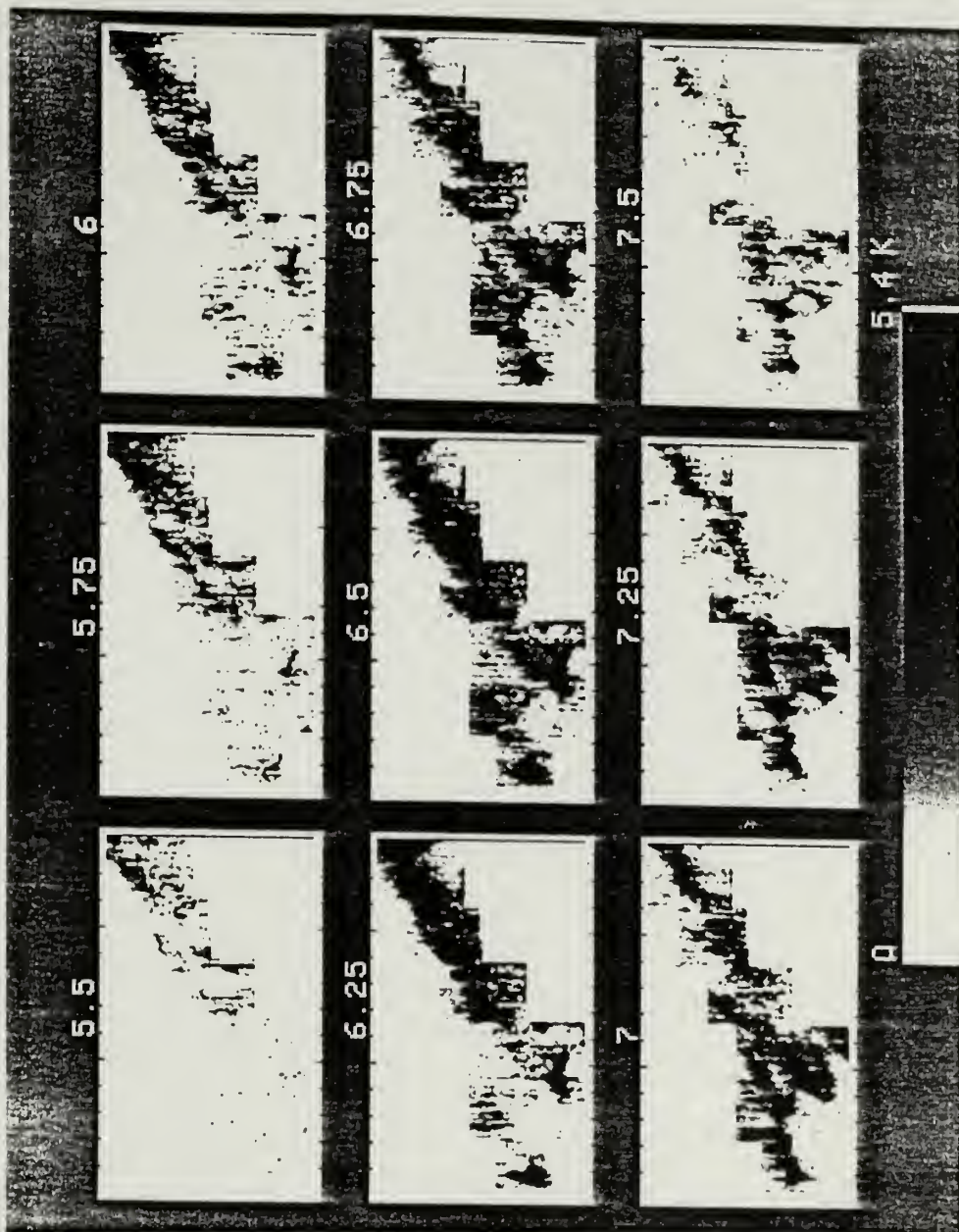
Figure 4 - A spatial velocity diagram of the ^{13}CO emission along a
strip. The center and direction of the strip is shown in the
insert to the Figure.
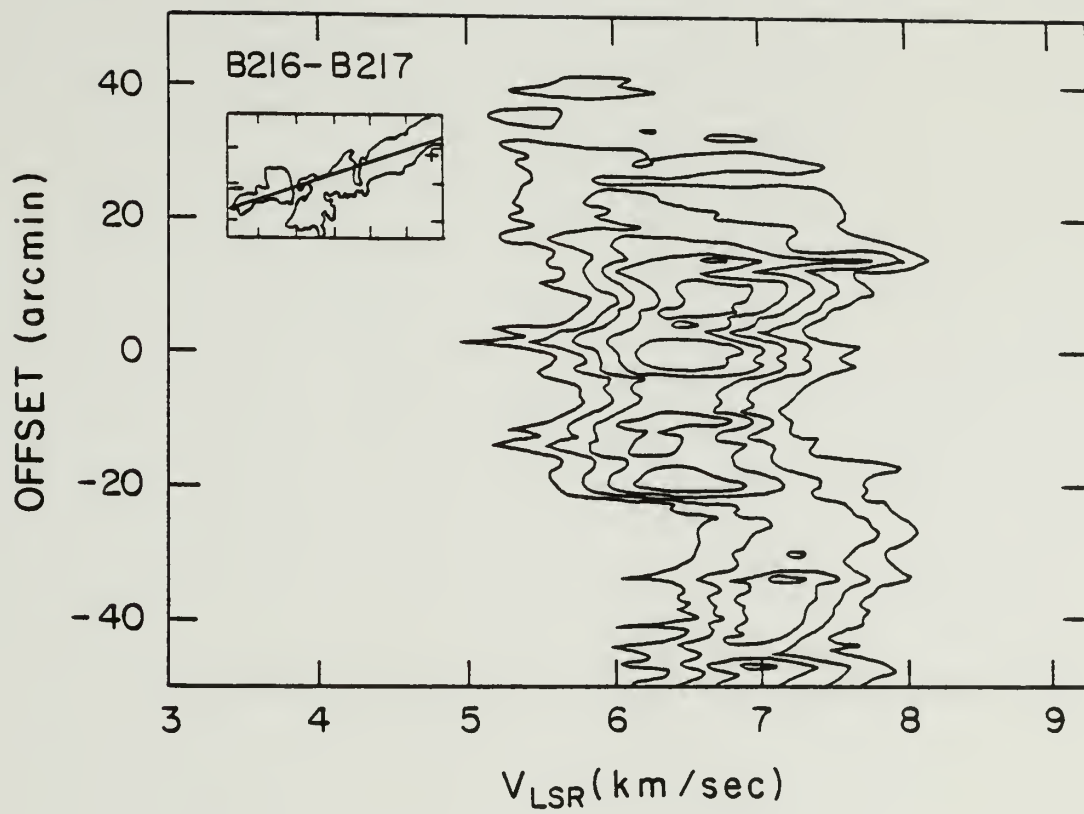
northwest indicating enhanced ^{13}CO line widths with respect to most regions within the cloud. The direction of the rotational axis is determined from the apparent velocity shear seen in Figures 3 and 4 and the absence of any appreciable velocity shear orthogonal to the length of the filament. We estimate the position angle of the rotational axis to be -145° with a 1 uncertainty of 10°. We note that the rotational axis direction is anti-parallel to that of the Taurus Cloud Complex (Kleiner and Dickman 1985) and of Heiles Cloud 2 (Schloerb and Snell 1984), located 3.5 degrees (8.4 pc) to the east. With the exception of the northwest region of the map, there are no multiple peaked lines over the regions observed in contrast to ^{13}CO J=1-0 spectra observed toward B213, a fragment to the northeast of B217 (Clark, Giguerre, and Crutcher 1977).

Previous polarization observations in Taurus have been concentrated toward Heiles Cloud 2 (Moneti et al. 1984; Hsu 1985). In order to determine the magnetic field direction closer to the B216-B217 clouds, we have obtained polarimetric measurements toward 60 stars located near the periphery of the region (Table 2). In Figure 5, we present a map of our polarization measurements in the direction of B216-B217. The plotted vector depicts the direction of the measured electric field component of the detected starlight. Under the assumption of the Davis-Greenstein alignment mechanism for dust grains, such vectors also describe the magnetic field direction within the cloud. The length of each vector is proportional to the measured percentage polarization.

Table 2

Polarimetry for B216-B217

Star	α(1950)	δ(1950)	P	e(p)	θ
1	04 15 05.1	27 03 25.0	2.72	0.07	78
2	04 15 35.9	26 55 24.0	1.56	0.09	49
3	04 15 41.7	26 59 33.0	2.86	0.06	44
4	04 16 11.6	26 45 59.0	2.15	0.14	33
5	04 16 24.0	26 57 14.0	4.63	0.25	33
6	04 16 41.0	26 46 39.0	1.54	0.22	21
7	04 16 46.2	27 12 54.0	3.64	0.09	21
8	04 17 10.4	26 53 38.0	2.68	0.09	35
9	04 17 15.9	26 44 49.0	1.50	0.09	21
10	04 17 31.0	26 49 21.0	1.69	0.09	35
11	04 17 43.5	27 05 41.0	1.79	0.14	14
12	04 17 54.5	26 48 01.0	1.96	0.12	26
13	04 18 09.5	27 00 25.0	2.16	0.05	72
14	04 18 13.0	27 11 36.0	5.08	0.19	171
15	04 18 23.5	27 06 28.0	1.55	0.06	11
16	04 18 32.3	26 44 30.0	1.82	0.11	30
17	04 18 39.3	26 40 20.0	0.08	0.05	00
18	04 18 46.3	27 47 42.0	0.52	0.17	53
19	04 18 55.3	27 03 53.0	1.93	0.09	18
20	04 18 59.4	26 39 07.0	2.61	0.05	22
21	04 19 13.0	26 54 43.0	1.79	0.08	17
22	04 19 13.9	26 27 15.0	0.21	0.05	33
23	04 19 21.6	26 28 06.0	1.46	0.13	43
24	04 19 28.0	26 23 11.0	1.64	0.04	51
25	04 19 29.5	26 44 40.0	1.59	0.14	37
26	04 19 52.0	26 53 09.0	1.83	0.11	29
27	04 20 10.9	26 54 45.0	2.39	0.11	15
28	04 20 11.8	26 19 23.0	2.13	0.05	47
29	04 20 28.0	26 50 12.0	0.84	0.04	19
30	04 20 28.1	26 20 51.0	2.25	0.17	52
31	04 20 37.3	26 45 33.0	1.15	0.09	3
32	04 20 45.5	26 40 16.0	1.82	0.05	9
33	04 21 00.7	26 42 55.0	1.82	0.06	12
34	04 21 29.3	26 47 28.0	1.96	0.08	12

35	04 21 34.6	26 19 59.0	4.04	0.13	46
36	04 21 44.9	26 31 07.0	1.20	0.11	26
37	04 21 46.0	26 22 05.0	3.33	0.09	35
38	04 21 56.2	26 29 02.0	1.76	0.18	10
39	04 22 15.4	26 10 13.0	2.62	0.20	52
40	04 22 26.6	26 05 44.0	0.06	0.07	-
41	04 22 33.4	26 34 16.0	2.14	0.17	11
42	04 23 00.0	26 33 33.0	2.37	0.15	22
43	04 23 03.7	26 11 03.0	1.37	0.12	54
44	04 23 18.0	26 27 53.0	1.63	0.08	22
45	04 23 22.6	26 21 48.0	1.99	0.10	32
46	04 23 35.0	26 03 28.0	0.72	0.14	33
47	04 23 43.1	26 18 43.0	1.90	0.16	41
48	04 23 49.4	25 54 48.0	2.74	0.12	30
49	04 24 08.0	26 20 21.0	1.37	0.11	34
50	04 24 36.5	26 21 40.0	1.39	0.08	20
51	04 24 44.7	26 05 20.0	1.43	0.14	30
52	04 24 54.8	26 04 29.0	0.31	0.16	118
53	04 25 09.1	26 11 00.0	3.29	0.16	29
54	04 25 12.9	26 18 59.0	2.30	0.19	19
55	04 25 38.3	26 07 37.0	1.72	0.11	29
56	04 25 44.2	26 18 02.0	1.31	0.08	8
57	04 25 53.2	26 10 06.0	2.03	0.10	19
58	04 26 01.7	26 15 34.0	2.64	0.10	22
60	04 26 13.1	26 17 38.0	2.82	0.16	23

Figure 5 - A map of the magnetic field geometry determined from visual

polarization measurements of starlight from background stars

toward B216-B217. The direction of the measured electric

field component is denoted by the plotted vectors

superimposed on a Palomar Sky Survey red print and the

magnitude of which is proportional to the measured percent

polarization.

The mean direction of the magnetic field determined from the distribution of polarization position angles over the surface of the cloud is 28° with a dispersion of 13°. The observed orientation of the filament and the rotational axis are well aligned with the magnetic field direction.

c) B18

Barnard 18 is the southernmost major cloud in the Taurus Complex. It has been the subject of many previous investigations because of its association with numerous T Tauri stars (see Figure 1). Early radio studies of the OH 18 cm line found a velocity gradient along the length of B18 indicative of rotation (Crutcher 1973). Later observations of formaldehyde suggested the gas motions were too complex to be entirely due to the rotation of the cloud (Heiles and Katz 1976). More recently, Murphy and Myers (1985) have reported a ring of enhanced ^{12}CO line widths with a radius of 0.8 pc centered on a cluster of T Tauri stars. They interpreted this ring as a shell of gas presumably driven by stellar winds from the T Tauri stars associated with B18.

An image constructed from the ^{13}CO integrated intensity over the velocity interval 4 to 8.25 km s^{-1} is diplayed in Figure 6. The image consists of 7700 spectra sampled at 1' spacing. The position angle of the B18 cloud is determined to be 10°. B18 appears to have fragmented into six cores along its major axis which are embedded within a diffuse envelope delineated by low level, ubiquitous emission. From the sum of

Figure 6 - A map of the ^{13}CO J=1-0 integrated intensity of the B18 cloud over the velocity interval 4 to 8.25 km s^{-1}.
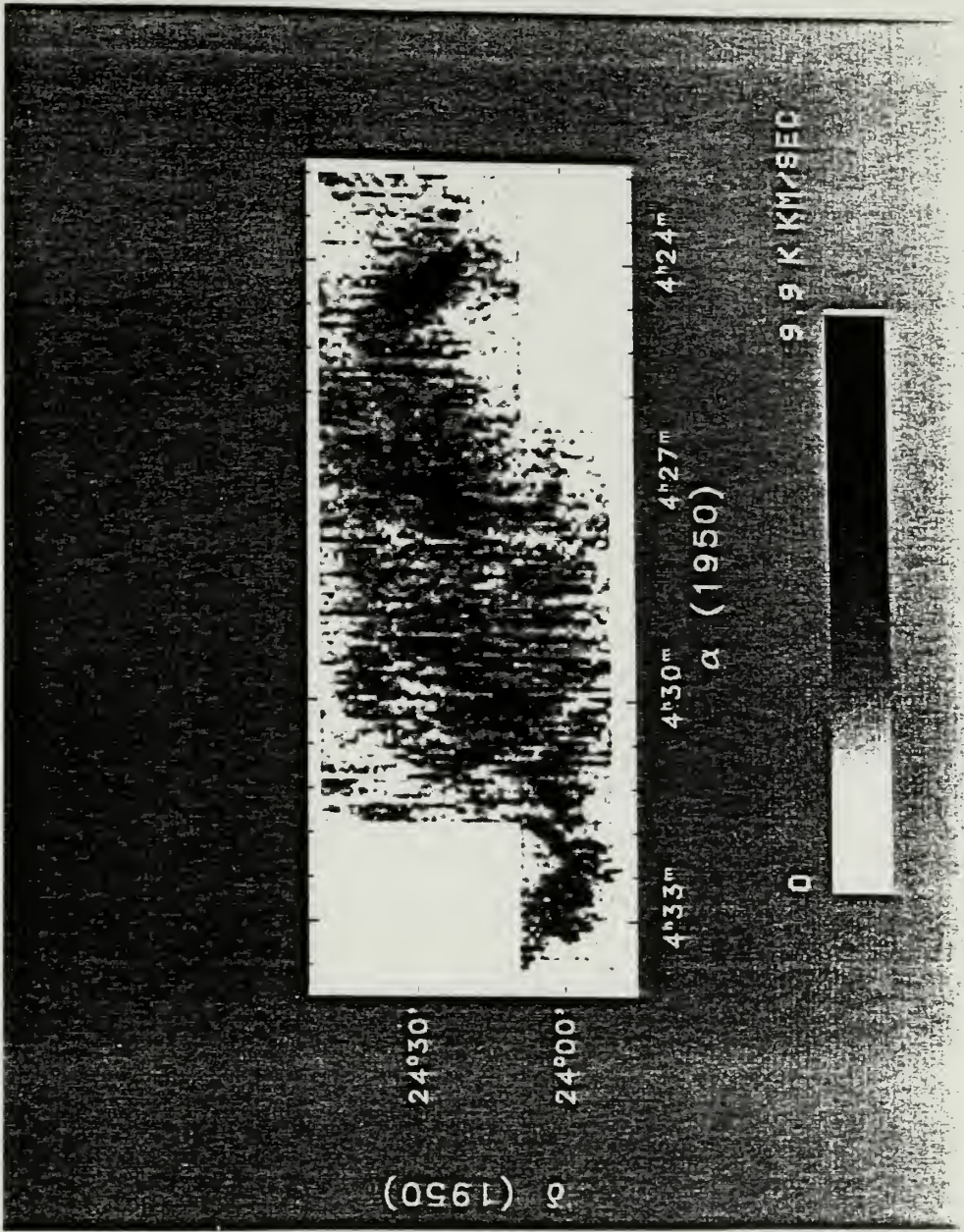
integrated intensities, the total mass is estimated to be 440 M_0. There is a marked similarity between features seen in ^{13}CO emission and those deduced from studies of visual extinction (Cernicharo et al. 1985). In Figure 7, we present a sequence of images, each representing the mean intensity within each velocity interval, which show the large scale velocity structure of the cloud. There is a tendency for emission to shift from east to west in images at increasing velocity, consistent with earlier claims that B18 is rotating (Crutcher 1973; Baudry et al. 1981; Murphy and Myers 1985). The gradient is more clearly seen in the spatial velocity diagram shown in Figure 8 which cuts across each of the major emission peaks. We calculate a mean velocity gradient of 0.1 km s^{-1} pc^{-1} across the cloud with a rotation axis position angle of 20°. It is also evident from Figure 8 that there are large deviations from a systematic velocity gradient suggesting that coherent rotation does not play a dominant role in the dynamics of B18 since these local deviations are much larger than the velocity shear over the same range due to rotation. In particular, there is peculiar red shifted emission from the eastern end of B18 and blue shifted emission from its western edge. Inspection of the ^{13}CO line profiles toward these localized regions indicate that the peculiar velocity emission is due to secondary velocity components often seen in the Taurus Clouds (Clark, Giguerre, and Crutcher 1977). It is these regions which exhibit multiple velocity components that comprise the ring of enhanced ^{12}CO line widths seen by Murphy and Myers (1985).

Figure 7 - A sequence of maps of the mean ^{13}CO J=1-0 intensity within each velocity interval demonstrating the large scale velocity structure of B18. Rotation of the cloud is indicated by the shift of the emission centroid from the southeast at low velocities to the northwest at higher velocities.
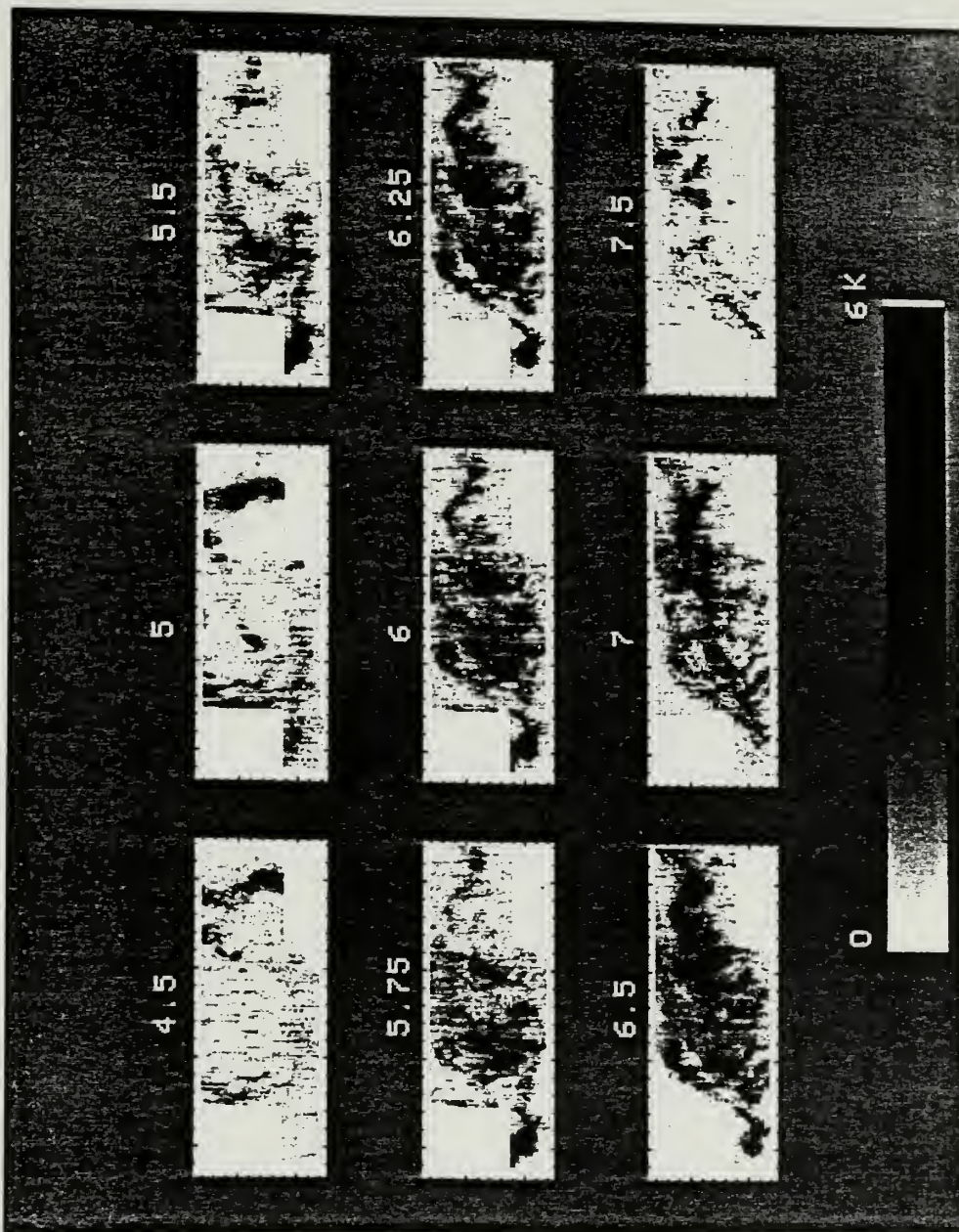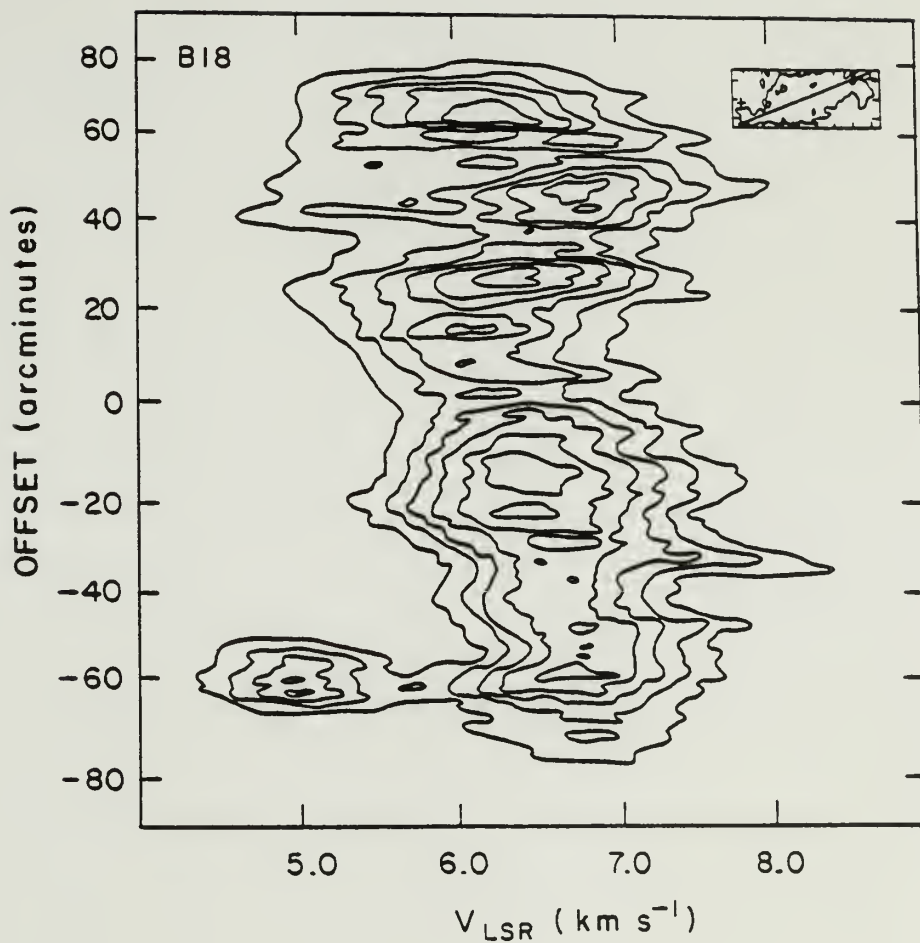
Figure 8 – A spatial velocity diagram of the ^{13}CO emission along a strip
through B18. The center and direction of the strip are
shown in the insert to the Figure.

A map of the magnetic field configuration determined from the polarization of 64 stars (Table 3) is displayed in Figure 9. From the distribution of polarization vectors, we calculate the mean position angle of the magnetic field direction to be 57° with a dispersion of 14°. There is a significant difference in the mean polarization position angles between B18 and B216-B217, located 1° north of B18 suggesting some distortion of the magnetic field lines over a 1 pc size scale. The orientations of the B18 cloud and its rotational axis exhibit larger offsets from the mean field direction than those of Heiles Cloud 2 or B216-B217 suggesting either a less important role of the field in the evolution of B18, or decoupling of the magnetic field from the gas at an earlier evolutionary stage.

d) L1517

The dark cloud L1517 is located toward the eastern end of the Taurus Complex. It is an isolated region of visual extinction viewed on the Palomar Sky Survey red print and is associated with several T Tauri stars and the Ae/Be star AB Aur. Figure 10 is an image of the integrated intensities of 1000 ^{13}CO J=1-0 spectra. The map is sampled at 1' spacing in the central region of the cloud and 2' spacing toward its periphery. The 2' sampled data are distinct as larger pixels. We estimate the mass of L1517 to be 42 M_0 from the observed ^{13}CO integrated intensities. The flattened structure seen in the larger clouds is largely absent in L1517 although a core detected in the 2' sampled data biases the axis of the cloud. The four fragments which possess most of the mass of L1517 are distributed with no preferred orientation.

Table 3

Polarimetry for B18

Star	α(1950)	δ(1950)	P	e(p)	θ
1	04 22 14.7	24 18 56.0	1.90	0.08	51
2	04 22 14.7	24 32 38.0	1.03	0.06	73
3	04 22 27.7	24 24 33.0	2.58	0.08	56
4	04 22 52.8	24 14 58.0	2.98	0.13	61
5	04 23 12.2	24 35 18.0	4.19	0.17	75
6	04 23 36.6	24 22 05.0	2.32	0.12	48
7	04 23 51.4	24 43 52.0	1.76	0.11	57
8	04 23 58.0	24 45 17.0	1.89	0.10	58
9	04 24 01.8	24 26 07.0	1.42	0.17	42
10	04 24 13.1	24 41 06.0	3.97	0.16	80
11	04 24 26.3	24 28 54.0	1.69	0.06	54
12	04 24 35.3	24 41 43.0	3.59	0.13	73
13	04 24 46.2	24 23 34.0	1.44	0.08	50
14	04 24 50.5	24 17 48.0	1.49	0.06	68
15	04 25 25.2	24 41 02.0	4.14	0.16	79
16	04 25 32.0	24 43 24.0	2.29	0.09	68
17	04 26 41.8	24 28 59.0	2.06	0.18	47
18	04 27 08.4	23 39 52.0	1.75	0.07	45
19	04 27 19.6	25 11 38.0	1.77	0.05	30
20	04 27 39.2	24 43 57.0	2.65	0.10	90
21	04 27 47.7	24 58 40.0	2.10	0.18	49
22	04 28 03.7	24 44 11.0	2.11	0.13	76
23	04 28 05.2	23 55 04.0	3.64	0.07	59
24	04 28 13.0	23 53 55.0	2.07	0.11	61
25	04 28 13.7	24 51 01.0	0.57	0.08	166
26	04 28 14.2	24 33 49.0	1.63	0.14	86
27	04 28 18.4	24 41 49.0	2.30	0.17	77
28	04 28 23.9	24 36 34.0	1.89	0.15	87
29	04 28 26.0	23 22 50.0	1.76	0.18	76
30	04 28 29.6	24 33 18.0	3.57	0.07	74
31	04 28 32.5	23 54 58.0	1.99	0.13	70
32	04 28 32.7	23 49 37.0	3.03	0.04	66
33	04 29 02.8	24 49 24.0	1.95	0.03	66
34	04 29 19.7	24 51 08.0	2.43	0.09	64

35	04 29 31.2	24 35 05.0	0.87	0.09	45
36	04 29 37.4	24 15 09.0	0.16	0.11	57
37	04 29 47.7	24 53 57.0	2.19	0.06	48
38	04 30 01.9	24 34 16.0	0.98	0.08	10
39	04 30 08.8	24 42 52.0	5.00	0.37	45
40	04 30 12.3	23 37 43.0	3.11	0.14	-8
41	04 30 25.4	24 49 07.0	2.85	0.07	53
42	04 30 41.1	24 40 43.0	2.73	0.04	43
43	04 30 51.1	23 37 07.0	3.27	0.16	51
44	04 30 53.0	24 27 58.0	3.53	0.07	52
45	04 31 00.2	24 25 38.0	2.11	0.11	49
46	04 31 05.4	23 51 27.0	2.11	0.11	49
47	04 31 11.9	23 58 56.0	2.25	0.08	57
48	04 31 28.8	24 32 44.0	2.39	0.13	53
49	04 31 54.8	23 59 34.0	2.83	0.07	51
50	04 31 56.2	24 17 20.0	3.89	0.14	48
51	04 32 02.0	24 14 41.0	3.03	0.09	50
52	04 32 06.1	24 03 28.0	3.04	0.30	56
53	04 32 17.3	24 09 29.0	4.37	0.13	57
54	04 32 18.7	24 08 09.0	4.40	0.13	57
55	04 32 30.3	24 21 00.0	4.31	0.13	38
56	04 33 05.3	23 52 17.0	3.85	0.13	49
57	04 33 06.8	24 19 04.0	3.60	0.10	40
58	04 33 08.9	24 16 46.0	2.80	0.11	41
59	04 33 12.3	23 51 44.0	3.14	0.11	66
60	04 33 26.3	24 02 47.0	4.35	0.16	58
61	04 33 40.0	24 05 45.0	2.26	0.04	60
62	04 33 42.0	24 20 03.0	3.48	0.10	43
63	04 33 51.5	24 10 56.0	5.40	0.18	52

Figure 9 - A map of the magnetic field geometry determined from visual
polarization measurements of starlight from background stars
toward B18.

5%

40

Figure 10 – A map of the ^{13}CO J=1-0 integrated intensity of the L1517 cloud over the velocity interval 4 to 8.25 km s^{-1}.
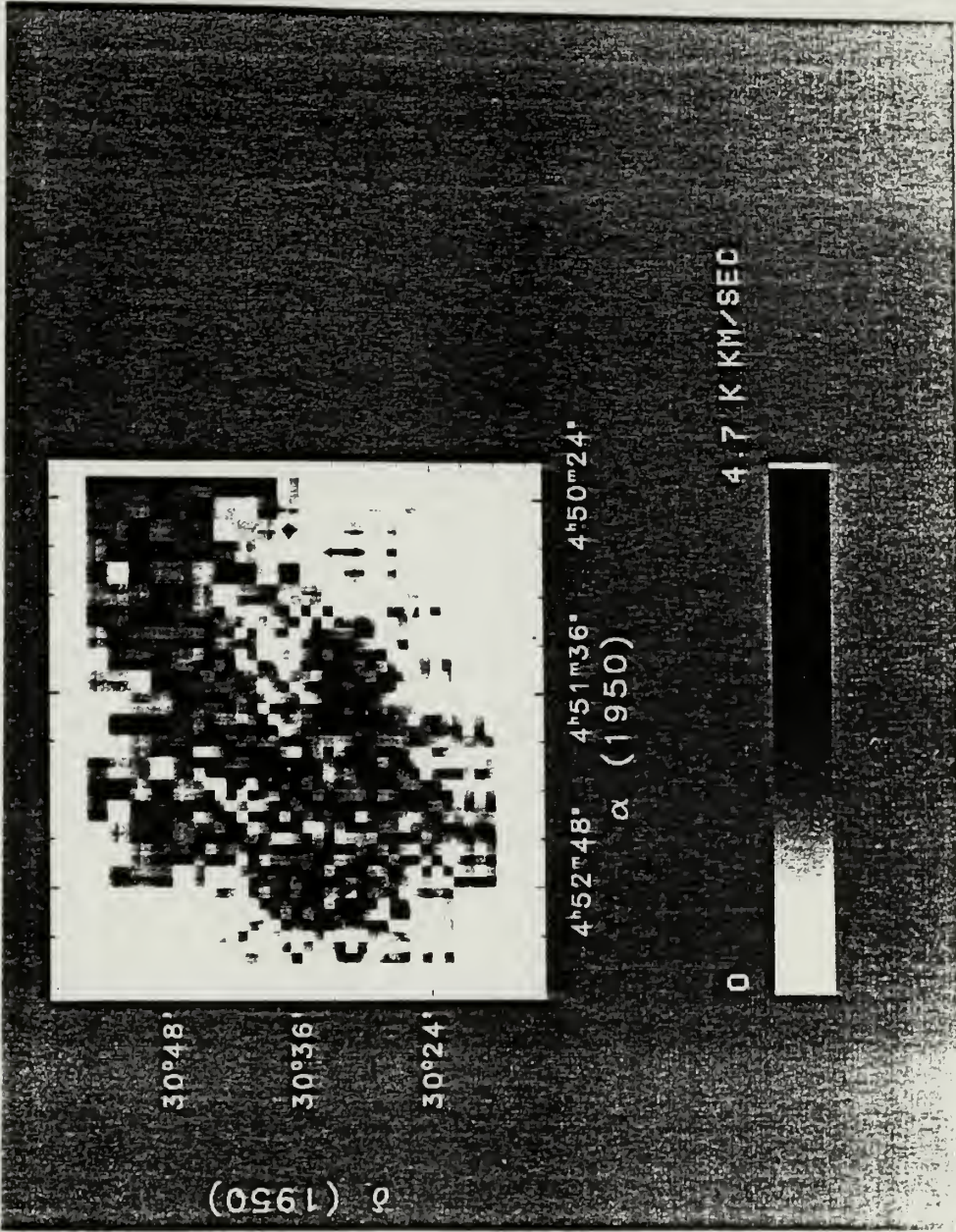
Figure 11 shows a sequence of intensity images in several velocity intervals. Most of the observed emission is from the 5.5 km s^{-1} velocity bin. There is a small velocity shear, seen more clearly in the spatial velocity diagram of Figure 12, from the southeast to the northwest. The gradient associated with the shear presumably due to rotation is 0.25 km s^{-1} pc^{-1} about an axis oriented at a position angle of 30°. The ^{13}CO full width half power line widths are uniform over the region mapped and generally are much narrower ($\Delta v = 0.8$ km s^{-1}) than those of most molecular clouds. There is no evidence for secondary velocity components as seen toward Heiles Cloud 2 and B18.

Both to examine the structure of the four fragments in more detail and to ascertain the saturation of the ^{13}CO emission, we have made a map of this region of the cloud in the J=1-0 $C^{18}O$ emission. A contour map of the integrated intensity of the $C^{18}O$ emission is shown in Figure 13 and, similar to the ^{13}CO emission, shows this region to be fragmented into clumps with enhanced column density. To determine if these fragments are also regions of increased space density we undertook observations of the J=10-9 transition of HC_3N, a good tracer of densities greater than $3x10^4$ cm^{-3} (Schloerb et al. 1983; Vanden Bout et al. 1983). Observations of HC_3N were made toward the most striking emission regions at offsets relative to the position $\alpha(1950)$ = $04^h52^m00^s$, $\delta(1950) = 30^o30'00"$ of (-1,-1), (-1,9), (-5,1), and (10,5) and toward the region of NH_3 emission (1.6,3.3) found by Myers and Benson (1983). HC_3N emission was detected only toward the known

Figure 11 – A sequence of maps of the mean ^{13}CO J=1-0 intensity within
each velocity interval demonstrating the large scale
velocity structure of L1517.
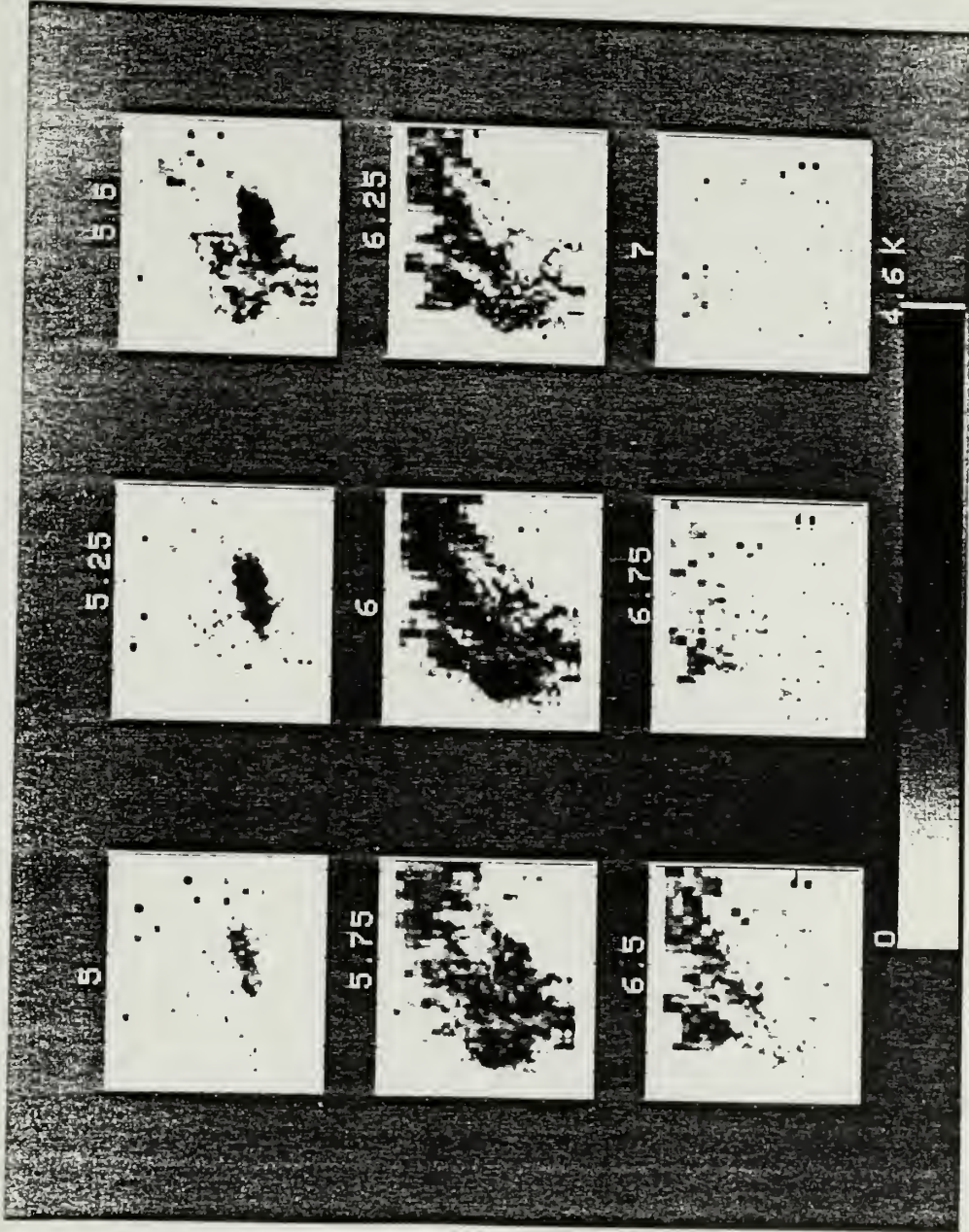
Figure 12 - A spatial velocity diagram of the ^{13}CO emission along a
strip of L1517. The center and direction of the strip is
shown in the insert to the Figure.

Figure 13 – A map of $C^{18}O$ J=1-0 emission of L1517 showing the similar features seen from the ^{13}CO maps. The inset shows HC_3N J=10-9 emission which traces gas space density but does not correspond to any column density peaks seen by ^{13}CO and $C^{18}O$ emission.
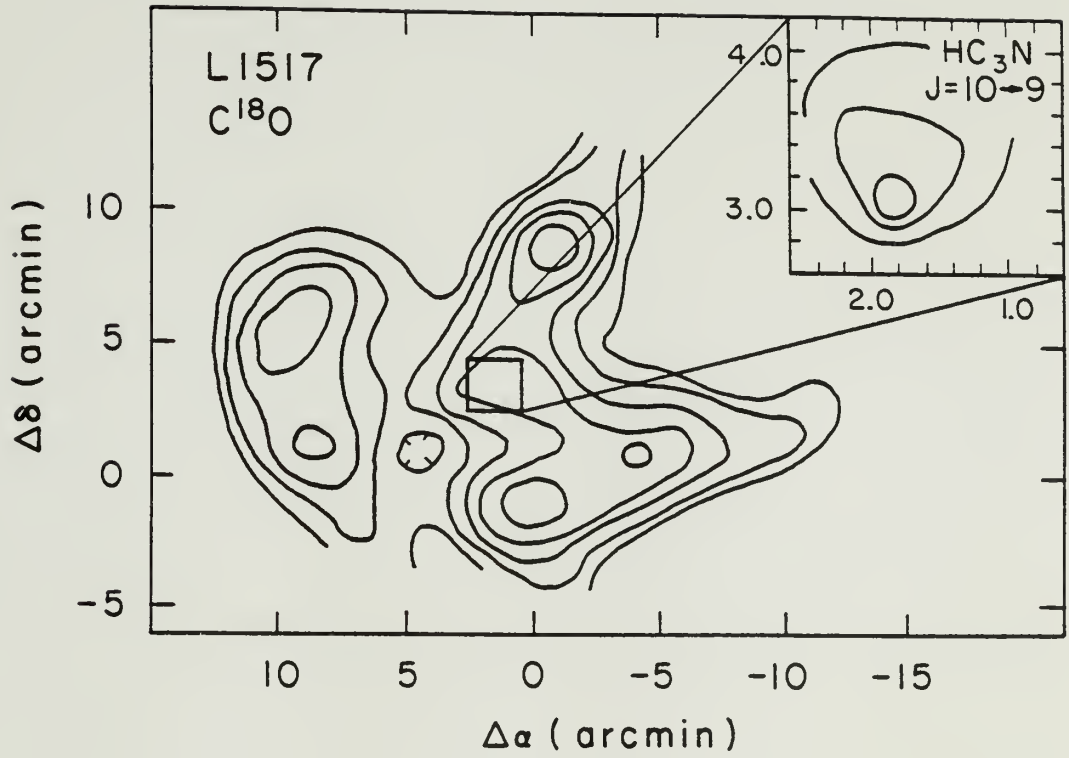
NH_3 emission region and was subsequently mapped; this map of the integrated HC_3N emission is shown as an insert to Figure 13. The line width of the HC_3N emission found for this region is only 0.3 km s^{-1}. The emission in other fragments was three to four times weaker and suggests that the highest density is found at the position not particularly distinguished in its $C^{18}O$ emission.

Further observations of the other fragments were made in the CS J=2-1 transition which requires densities of order 10^4 cm^{-3} to excite. CS emission was detected toward positions (1.6,3.3), (-1,-1), (10,5), (-1,9), and (-7,1) with intensities varying from $T_R^* = 0.6$ to 1.1 K and line widths typically 0.4 km s^{-1}. Thus, all of the high column density regions obvious in both ^{13}CO and $C^{18}O$ maps are also regions of enhanced space density. These fragments are likely to be sites of future star formation like the fragment near the position (8,1) where both the Ae/Be star AB Aur and several T Tauri stars are found (Figure 1).

The magnetic field structure is not well determined here since polarization maps of Moneti et al. (1984) and Hsu (1985) are not well sampled at the eastern end of the Taurus cloud. No additional observations are available from our survey. We estimate a mean direction of 55° to the magnetic field in this region based on the most easterly points of these earlier studies and the relatively small dispersion of the measured position angles of the electric field vectors throughout the complex.

e) L1544

The dark cloud L1544 is another isolated region of high visual opacity and defines the eastern edge of the Taurus Complex. Since it exhibits little evidence of recent star forming activity in the form of IRAS point sources (Figure 1), it offers a valuable comparison with more active star forming regions. Figure 14 shows the observed spatial distribution of ^{13}CO J=1-0 integrated intensity. The mass of L1544 is 43 M_0 based on the sum of ^{13}CO integrated intensities over the region mapped. Most of the mass is contained within the core in the southern part of the cloud with a smaller percentage of the mass distributed between two fragments in the northern region of the cloud.

The velocity structure of L1544 is shown in Figure 15 as a sequence of images of the mean ^{13}CO J=1-0 intensity within each velocity interval. The mean V_{lsr} of L1544 is 7 km s^{-1} which is peculiar with respect to the canonical V_{lsr} of 5.5 km s^{-1} for the eastern end of the Taurus Complex (Kleiner and Dickman 1985). There is a moderate shift in mean velocity between the cores as seen in the spatial velocity diagram (Figure 16) indicating a rotational axis position angle of 60°. In addition, the southern core appears to be rotating. We have also made further observations of L1544 in $C^{18}O$ and HC$_3$N emission to determine the density structure of the high column density region in the south-east end of the cloud. A contour map of the integrated intensity of the J=1-0 $C^{18}O$ emission in this region of L1544 is shown in Figure 17. Estimates of the density of this region based on H_2CO and HC$_5$N

Figure 14 – A map of the ^{13}CO J=1-0 integrated intensity of the L1544

cloud over the velocity interval 4 to 8.25 km s^{-1}.
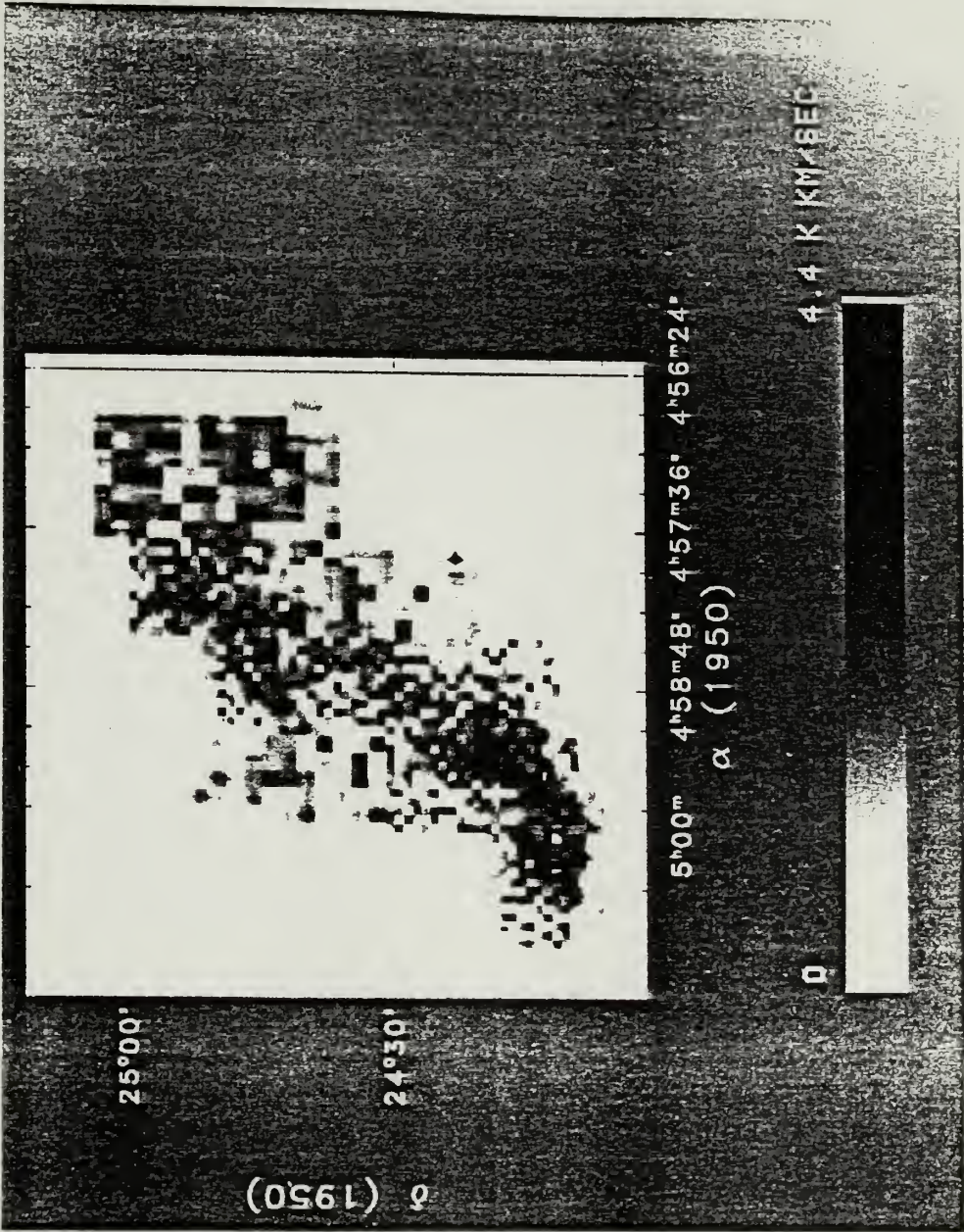
Figure 15 – A sequence of maps of the mean ^{13}CO J=1-0 intensity within
each velocity interval demonstrating the large scale
velocity structure of L1544.
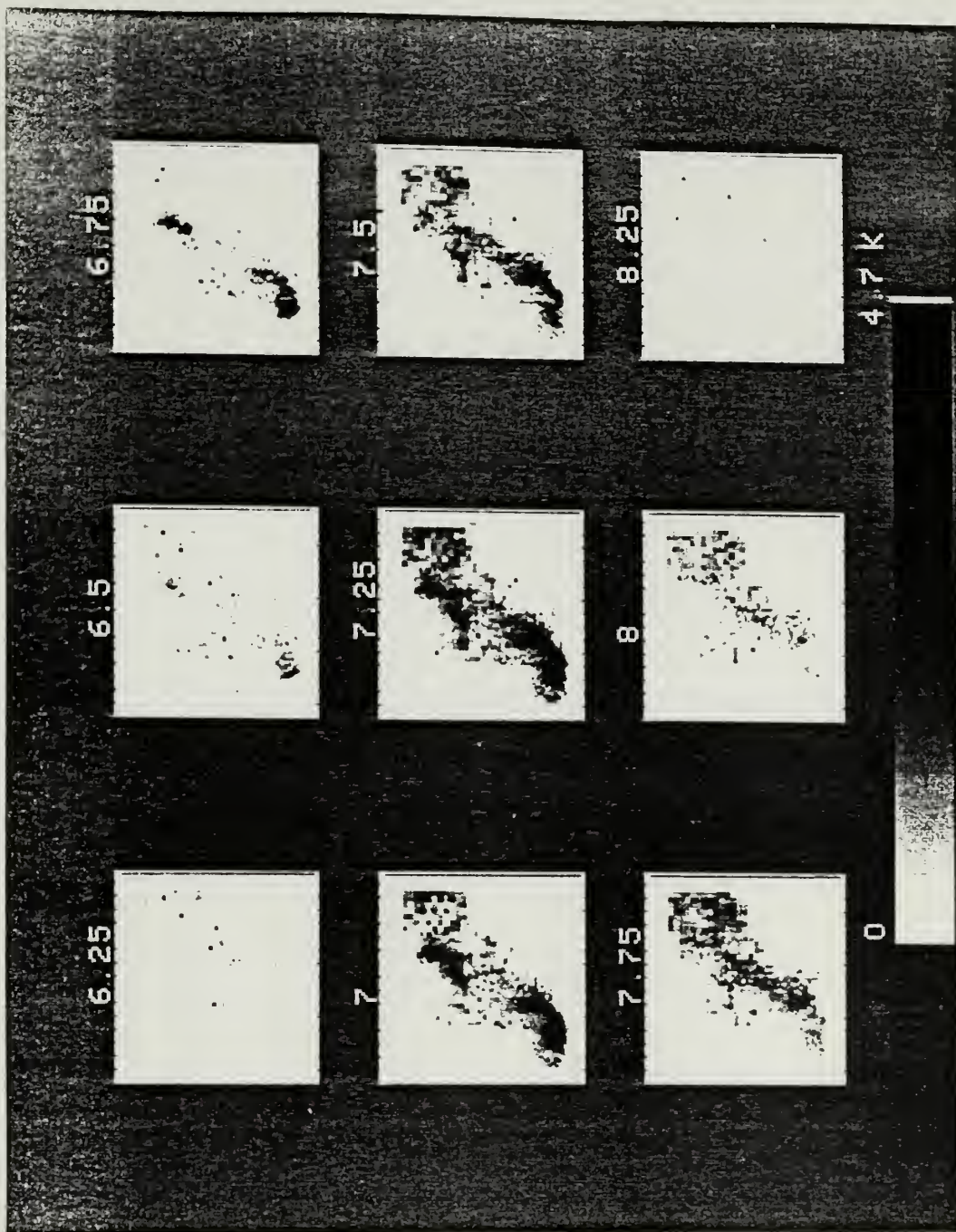
Figure 16 – A spatial velocity diagram of the ^{13}CO emission along a
strip of L1544. The center and direction of the strip is
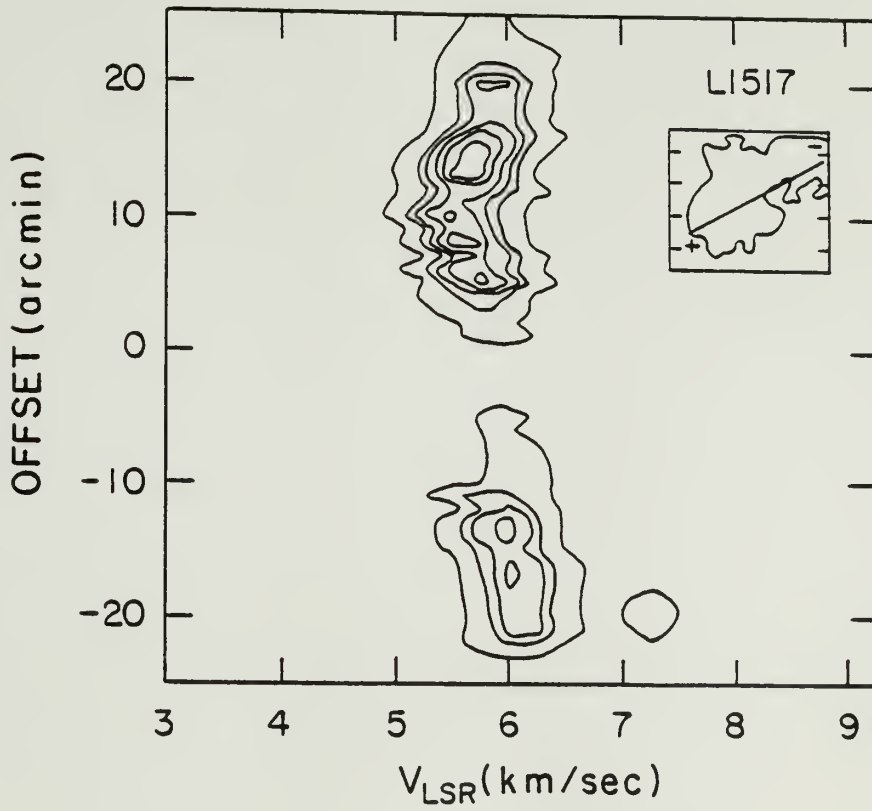shown in the insert to the Figure.
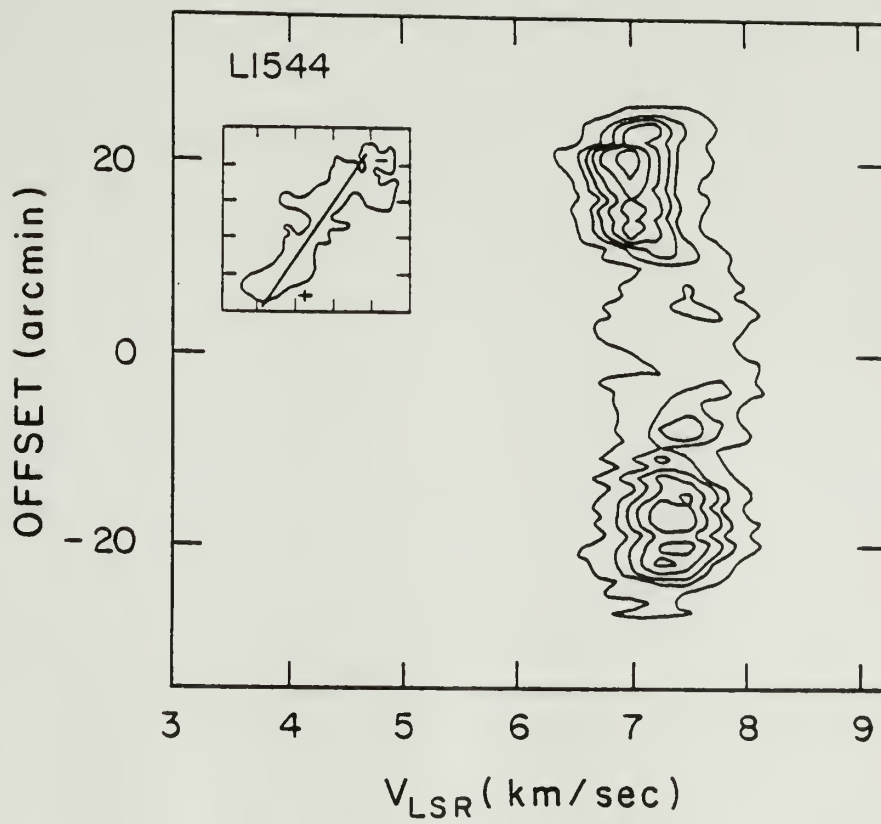
Figure 17 - A map of $C^{18}O$ J=1-0 emission of L1544 showing the similar features seen from the ^{13}CO maps. The inset shows HC_3N J=10-9 emission. Unlike L1517, the gas space and column density peaks spatially coincide.
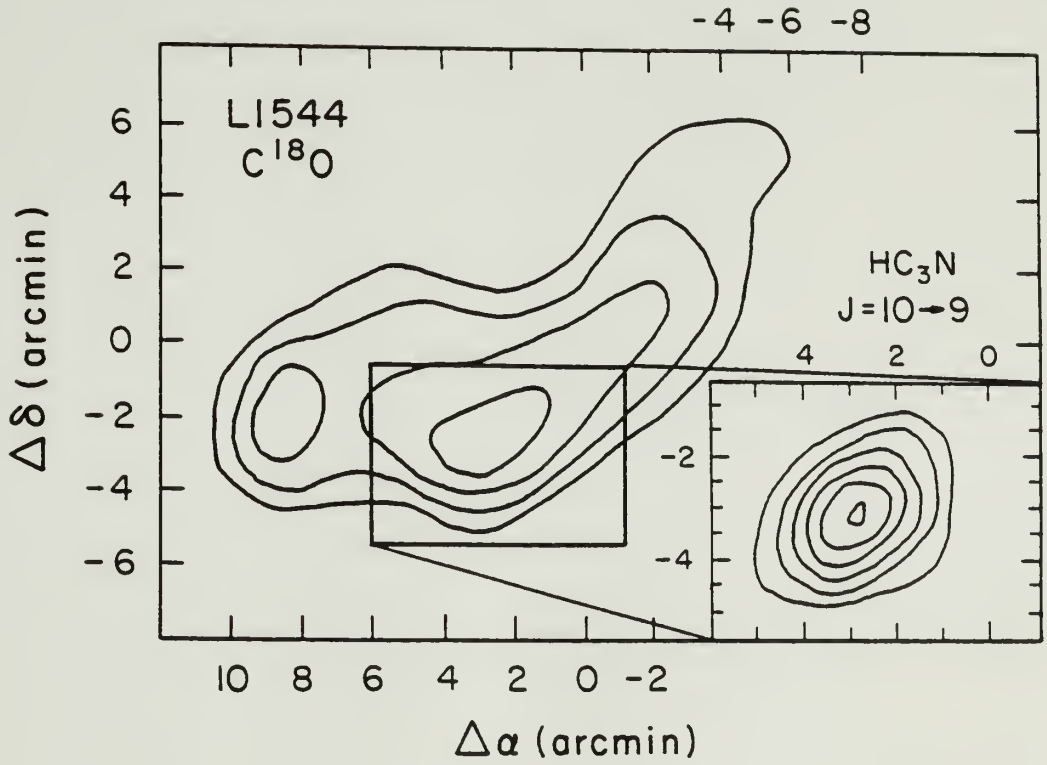
observations indicate values of $1-4 \times 10^4$ cm^{-3} (Snell 1981; Snell et al. 1981). Thus, the southeast end of this cloud contains not only much of the mass of the cloud, but also has a high column density and space density fragment. This region, though a prime location for star formation, has of yet no evidence of the formation of stars.

As in the case of the L1517 region, no previous polarization measurements have been taken toward L1544. Consequently, the direction of the magnetic field is uncertain. We have extrapolated the maps of Moneti et al. (1984) and Hsu (1985) to assign a mean magnetic field direction of 55°.

DISCUSSION

a) ^{13}CO Optical Depth

In is crucial to this study that our probe of the molecular gas is an adequate tracer of the gas column density. A compromise is reached between choosing an absolutely optical thin probe such as $C^{18}O$ and using a more abundant molecule such as ^{13}CO which is generally thin and readily detectable over the large extent of the cloud. To ensure that the ^{13}CO J=1-0 emission is thin, we have observed the $C^{18}O$ J=1-0 emission from selected regions within the clouds where the ^{13}CO emission is strongest and most likely to be saturated. Assuming that the excitation temperatures for the two molecules are equal, and that the $C^{18}O$ emission is optically thin, then the optical depth of the ^{13}CO radiation over the velocity interval of detectable emission can be

determined from the ratio of the ^{13}CO and $C^{18}O$ integrated intensities,

$$\frac{\int T_R^*(^{13}CO) \, dv}{\int T_R^*(C^{18}O) \, dv} = \frac{(1 - \exp(-\tau))}{\tau} X_{iso} \qquad (1)$$

where X_{iso} is the abundance ratio of ^{13}CO and $C^{18}O$ (terrestrially 5.5), and τ is the ^{13}CO optical depth. In Figure 18, we present a histogram of the ratio between ^{13}CO and $C^{18}O$ integrated intensities for all positions observed in $C^{18}O$. Values greater than 5.5 are due to weak or non detections of $C^{18}O$ emission. The mean of the distribution is 5.0 and consistent with relatively optically thin ^{13}CO emission even in the densest regions. The smallest ratio observed, 2, indicates the highest optical depths are only 2.5. Thus, while a few particular lines of sight may suffer from significant ^{13}CO opacity, we feel that the J=1-0 transition of this molecule can be used as a tracer of ^{13}CO column density.

b) Magnetic Evolution of the Taurus Clouds

The Taurus Molecular Cloud Complex, and presumably most molecular clouds, are composed of many sub clouds such as the regions studied here. A coarsely sampled map (15' spacing) of the entire Taurus Cloud Complex in ^{13}CO emission reveals that the component clouds are distributed along a filament with an axis of 55° and observed to be rotating about a similar axis (Kleiner and Dickman 1984). The apparent anisotropy of the gas configuration and kinematics at densities of 500 cm^{-3} with respect to the magnetic field geometry of the complex

Figure 18 — A histogram of the ratio between ^{13}CO and $C^{18}O$ integrated intensities observed toward the most opaque regions of the clouds. The histogram shows that the ^{13}CO emission is generally optically thin.
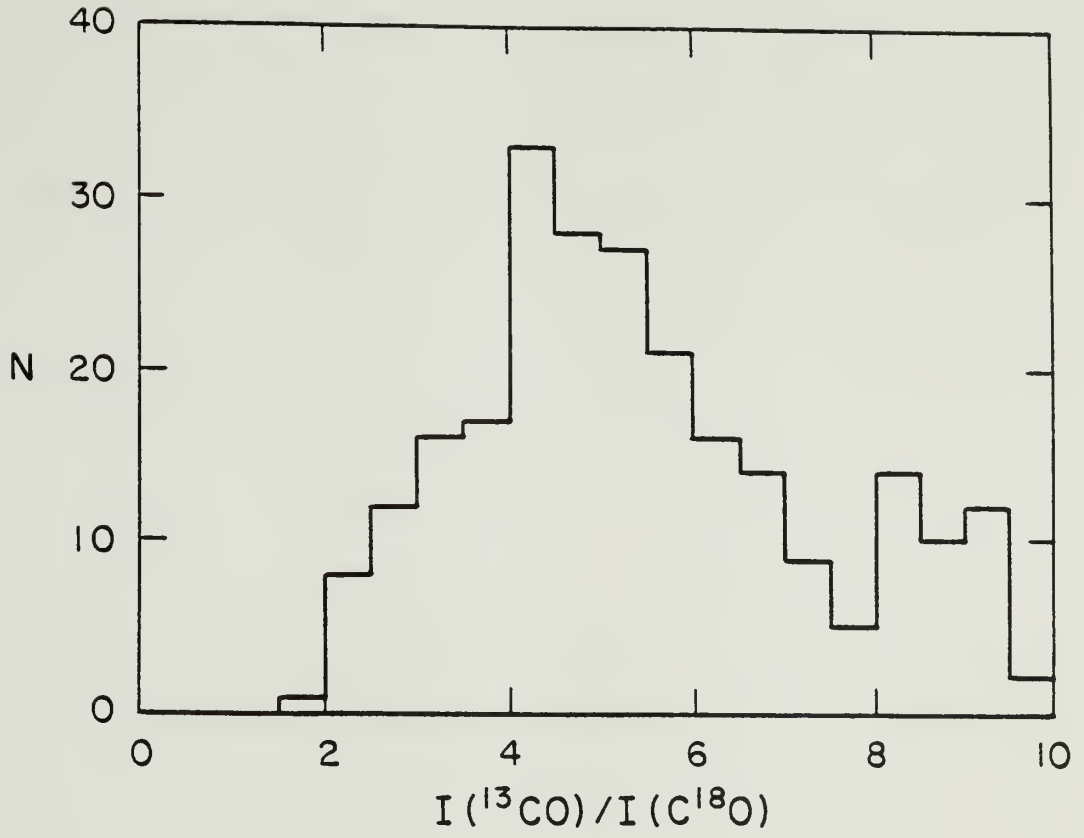
determined from earlier polarization data (Moneti et al. 1984; Hsu 1985) suggests that the global evolution of the Taurus Cloud is in part regulated by the interstellar magnetic field. A statistical analysis of the spatial distribution of molecular column densities indicates a characteristic spacing between the component clouds of 14 pc (Kleiner and Dickman 1984). Recent observations of HI absortion features reveal a distribution of atomic gas similar to that found from CO studies, that is, oriented along the magnetic field direction and with a characteristic spacing of 14 pc (R.L. Dickman, private communication). Such similarities between the molecular and atomic gas components of the Taurus Cloud suggests that (1) the magnetic force is the dominant stress in the pre-molecular HI cloud and (2) the component clouds formed when gas was predominantly atomic before further condensation into molecular clouds.

The Taurus clouds (Heiles Cloud 2, B216-B217, B18, L1517, and L1544) as seen by ^{13}CO emission exhibit flattened structure. It is difficult to determine the geometry (oblate or prolate) of the gas when seen projected onto the plane of the sky. Schneider and Elmegreen (1979) suggest that the flattened structures are prolate given the regular spacing between subcondensations whereas one might expect a more random spacing for a disk viewed edge-on. The oblate nature of Heiles Cloud 2 is exposed to the observer by its line of sight inclination. Moreover, the rotational axes of the clouds studied are parallel to their minor axes suggesting kinematics more readily explained by a disk

geometry than a prolate geometry. Thus, we believe that the flattened gas distributions denote oblate structures.

The most striking features found from the comparison of the ^{13}CO and polarization data are the general alignment of the clouds and rotational axes along the magnetic field lines (see Table 4) and the uniformity of the direction of the polarization vectors over size scales of 2 pc toward regions of larger visual extinctions than those of previous studies. The observations strongly suggest that turbulent motions do not dominate cloud dynamics on these size scales. Given the isotropic character of turbulence, one might expect either spherical gas distributions or cloud orientations and rotational axes randomly distributed. The presence of rotation can lead to flattening of an initially spherical object with a minor axis parallel to the rotational axis. Such systematic velocity fields are found in the five clouds studied here. However, with the exception of Heiles Cloud 2, the velocity shear due to rotation is small with respect to the observed ^{13}CO line widths. Thus, it is unlikely that the centrifugal stress is responsible for the observed flattened structure of the clouds. The relative unimportance of rotation in other clouds studied by Arquilla and Goldsmith (1986) confirms the inefficiency of the centrifugal stress on the gas at the sizes and densities which characterize molecular clouds. Rotation is expected to play a more significant role at smaller size scales during free fall collapse of a core assuming the angular momentum is not completely redistributed to the ambient medium via

Table 4

Cloud Orientations and Energies

Cloud	$\langle\theta_B\rangle$	θ (degrees)	θ_{rot}	dv/dr (km s^{-1} pc^{-1})	E_{grav}	E_{rot} (10^{45} ergs)	E_{turb}
Heiles Cloud 2	50	30	30	0.83	63	7	35
B216–B217	28	35	35	0.25	3	1	3
B18	57	10	10	0.10	15	2	10
L1517	55	30	30	0.18	0.2	0.03	0.3
L1544	55	60	60	0.25	0.4	0.06	0.3

magnetic braking. In addition, Cassen et. al. (1984) have noted that
the coherence of observed polarization vectors is indicative that
turbulence is either wavelike or insignificant with respect to the
magnetic field pressure otherwise the field lines would become tangled
and randomly oriented due to turbulent eddy currents.

While rotation has been demonstrated to be dynamically unimportant
on size scales greater than 0.5 pc, it is present in the clouds studied
here. In all cases, the inferred rotational axis is roughly parallel to
the magnetic field direction. Such alignment is consistent with the
redistribution of angular momentum via torsional Alfven waves in which
the component of angular momentum perpendicular to the magnetic field
direction is more efficiently transported to the surrounding medium than
the component parallel to the magnetic field direction. As such, it is
a signature of the significant influence of the magnetic field on the
dynamics of the cloud material (Mouschovias and Paleologou 1980). It is
worthy to note that the angular momentum axis of B216-B217 is peculiar
with respect to the other cloud rotational axes and that of the Taurus
Cloud Complex in that it is rotated by 180°. Such reversal may result
from the coupling of the filament to its neighbor clouds via magnetic
field lines and the reflection of radiated Alfven waves (Mouschovias et
al. 1985). Such a scenario appears unlikely here given the observed
magnetic field line morphology and the relative orientation of the
clouds. It seems even more unlikely that collisions could offset the
rotational axis within the lifetime of the cloud since many collisions
are likely required to reorient the rotational axis by 180°.

It appears plausible that <u>the elongated structures in the Taurus</u> <u>Cloud are</u> <u>a result of quasi-static collapse controlled by the</u> <u>interstellar magnetic field</u>. Such a magnetically regulated evolution produces oblate structures with minor axes parallel to the field direction as gas (neutrals and ions) tends to collapse along field lines while lateral contraction is inhibited (Mouschovias 1976). In addition, the rotational axis is expected to be preferentially aligned with the magnetic field direction (Mouschovias and Paleologou 1980) as is observed toward the clouds in this study.

Comparison of the clouds with each other reveals differences in their orientations and structures. In particular, Heiles Cloud 2 appears to be very well aligned with the magnetic field direction to within 10°, with only moderate density enhancements of the fragments with respect to the underlying ring structure. In contrast, B18 is not as well aligned with the magnetic field but has more distinctive fragments. We speculate that such differences may be due to varying stages of magnetic evolution of the individual clouds. Specifically, if a larger fraction of the gas associated with B18 has decoupled from the magnetic field, then collisions and gravitational interactions in the absence of magnetic restraining forces may tend to reorient the cloud from an initially aligned configuration. A direct consequence of such decoupling is the loss of magnetic support against gravitational forces and an enhanced rate of star formation. Subsequent stellar winds associated with young stellar objects provide a mechansim for the

removal of interfragment gas, leaving in their wake, the observed isolated cores of B18. The ring of enhanced line ^{12}CO line widths seen by Murphy and Myers (1985) may be a signature of such dispersal.

While it is difficult to distinguish evolutionary states of molecular clouds, there is evidence that B18 has evolved more rapidly than Heiles Cloud 2. From HI observations of the two regions, 21 cm absorption features are more pronounced in Heiles Cloud 2 than in B18 and are indicative of a higher abundance of atomic hydrogen in Heiles Cloud 2 (Batrla et al. 1983). The lower HI abundance in B18 may be due to the conversion to molecular hydrogen (Allen and Robinson 1976). From this argument, Batrla et al. (1983) estimated the ages of B18 and Heiles Cloud 2 to be 6×10^6 years and 3×10^6 years respectively. The properties of the embedded and T Tauri star populations within each of the clouds provides another estimate of their relative lifetimes though comparison of the ages of T Tauri stars reveals no evolutionary distinction between the two regions (Cohen and Kuhi 1979). However, ten out of eleven of the young stellar objects in B18 are either T Tauris stars or have far infrared spectral energy distributions similiar to that of T Tauri stars (Emerson 1985). In Heiles Cloud 2, the fraction of T Tauri and T Tauri-like stars among all associated young stellar objects is 6 out of 11 perhaps indicative of a younger stellar population and a more inhibited rate of star formation.

c) Virial Equilibrium

The longevity of molecular clouds with respect to their free fall collapse times indicates that these objects are supported against their own self-gravity and external pressure forces. Such a condition of support is reflected in the state of virial equilibrium typically observed in molecular clouds over a large range of sizes and densities (Larson 1981; Myers 1983). However, it is inaccurate to presume that the virial condition is satisfied everywhere within the cloud since star formation must occur in localized regions. In addition, evaluation of the virial theorem is only accurate to within factors of a few given the uncertainties of the density law and line of sight geometry of the clouds. Nevertheless, global equilibrium of the cloud as given by the virial theorem is expected.

We have investigated the equilibrium of the clouds using the virial theorem assuming they are self-gravitating objects. In Figure 19, we display the observed masses from ^{13}CO column densities versus the virial mass for a uniform density cloud calculated from

$$M_{virial} = 208 \ \Delta v^2 \ R \ M_0, \tag{2}$$

where Δv is the mean full width half power line width and R is a characteristic radius of the cloud in pc. We have calculated R from the relation,

$$R = (\sigma_\alpha \ \sigma_\delta)^{1/2} \tag{3}$$

where σ_α and σ_δ are the dispersions in the equatorial directions about

Figure 19 - A plot of the observed mass of each cloud determined from ^{13}CO column densities versus the virial mass determined from the observed ^{13}CO line width and extent of the emission. The clouds exhibit a tendency toward equilbrium.
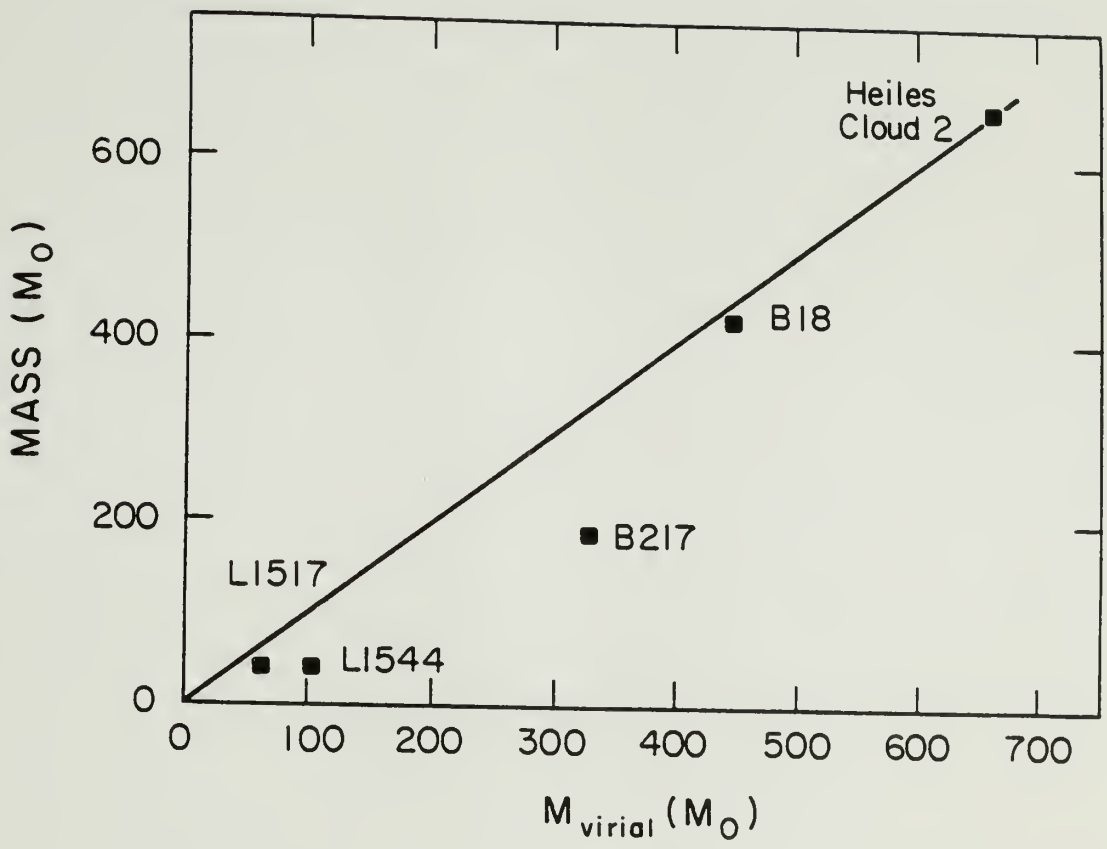
the geometric center. The equilibrium of the five clouds is indicated by their relative location from the line $M = M_{virial}$.

The observed line widths are likely a sum of thermal, turbulent, and Alfvenic motions. Given the relative importance of the magnetic field in the evolution of the clouds, the observed line widths must be characterized by Alfvenic disturbances. However, magnetic field lines must be perturbed in order to generate the magnetosonic or Alfvenic wave modes with amplitudes similar to the observed line widths. These perturbations may be produced by expanding HII regions, stellar winds, rotating cloud cores, or the relative motion between magnetically coupled clouds (Arons and Max 1975; Falgarone and Puget 1986). Such processes ought to give rise to a spectrum of magnetic disturbances within the cloud with the longer wavelength modes being less susceptible to dissipation (Zweibel and Josafatsson 1983). Thus, the turbulent pressure attributed to the support of the molecular cloud may in fact, be coupled to the interstellar magnetic field.

CONCLUSIONS

Results from extensive mapping of the ^{13}CO $J=1-0$ emission and polarization measurements indicate a probable magnetic evolution of the Taurus Cloud Complex. The component clouds exhibit flattening along the inferred magnetic field direction which is consistent with gas collapsing parallel to the magnetic field direction while lateral collapse is inhibited by magnetic pressures. Rotation is detected

toward the five clouds studied. The rotational axis is observed to be parallel to the magnetic field direction as expected for a cloud magnetically coupled to the external medium. It is proposed that the distinction of the B18 cloud with respect to the other clouds studied is due to the partial decoupling of the magnetic field from the gas. The clouds are observed to be in approximate virial equilibrium which may reflect the ringing of magnetic field lines by some disturbance.

CHAPTER III.

The Magnetic Evolution of the Taurus Cloud:
Decoupling of the Magnetic Field from the Gas

INTRODUCTION

Star formation occurs in the densest regions of molecular clouds.
These pockets of dense gas often referred to as cloud cores, represent
the smallest (r = 0.1 pc) size scale in the observed structural
hierarchy which characterizes the interstellar medium (Scalo 1985).
Since these regions likely denote the final stages before free fall
collapse to the protostellar state, the properties of dense cores such
as mass and angular momentum, may have significant implications for the
stars and associated circumstellar environments that eventually form
within their domain. For example, the angular momentum of the core most
likely leads to the formation of either a circumstellar disk or multiple
stellar system (Tereby, Shu, and Cassen 1984; Boss 1980). Consequently,
the evolution of diffuse molecular material to the dense core
configuration has received considerable study. In particular, some
investigators have attributed a prominent role to the interstellar
magnetic field in the formation and kinematics of cloud cores (Shu 1983;
Mouschovias and Paleologou 1981). However, there have been few direct
observations to date to characterize the role of magnetic fields in the
origin of cloud cores.

In an earlier study (hereafter Paper I), Heyer et al. (1986a) presented detailed observations of the molecular gas (maps of ^{13}CO J=1-0 emission) and the magnetic field geometry (based on visual polarization measurements of light from background or embedded stars) toward five major clouds within the Taurus Molecular Cloud Complex. These observations suggest that the evolution of the gas in the regions characterized by densities of 10^3 cm^{-3} is dominated by the stress of the interstellar magnetic field, based on both the flattened morphology and the alignment of the rotational axis of the component clouds with the magnetic field direction (Mouschovias 1976; Mouschovias and Paleologou 1980). However, such a dynamically active magnetic field is not expected to extend indefinitely to smaller regions since the effective force of the magnetic field on the neutrals via collisions with ions is reduced due to the smaller fraction of ionization at higher densities resulting from shielding of cosmic rays by the surrounding material.

In this study, we extend the analysis of Paper I to the dense ($> 10^4$ cm^{-3}) core regions to determine whether the magnetic field still plays an important role in the evolution of the gas at the higher densities which characterize these regions. The dense cores are delineated by enhanced ^{13}CO emission; Paper I describes the observations of these regions. The signature of a dynamically significant magnetic stress is a flattened core whose orientation (defined here as the position angle of the minor axis) and an angular momentum axis if rotating, lie parallel to the local magnetic field

direction. In Section II, we describe the procedure used to separate the cores from the parent cloud and present the properties of the isolated cores. In Section III, we discuss the ability of the magnetic field to account for these observed properties.

RESULTS

a) Isolation of Cloud Cores

Dense cores in dark clouds typically have mean densities of 10^4 cm^{-3} (Myers 1985). Consequently, such regions are primarily observed with tracers of high gas volume density such as emission from NH_3, H_2CO and CS molecules (Myers and Benson 1983; Snell 1981). From NH_3 observations, Myers and Benson (1983) note that dense cores are characterized by sizes of 0.1 pc, masses between 0.3 and 10 M_0 and kinetic temperatures ~ 10 K. The ^{13}CO J=1-0 emission is a reasonably good probe of column density although the actual distribution is subject to uncertainties arising from variations along the line of sight. In Paper I, it was demonstrated that the position of peak ^{13}CO and $C^{18}O$ emission coincided with HC_3N J=10-9 and CS J=2-1 emission which directly probe regions of high volume density. Thus, we believe that strong ^{13}CO emission is a reflection of a volume density enhancement within the cloud. The ^{13}CO emission is more extended than that of NH_3 and CS since lower densities (10^3 cm^{-3}) are required to excite the ^{13}CO J=1-0 transition and the ^{13}CO molecule is more abundant over a wide range of conditions (Myers and Benson 1983).

We choose in this investigation to make use of our extensive ^{13}CO maps of the Taurus Cloud to identify additional core regions. However, because the ^{13}CO emission is not restricted to the cores but is also observed on larger size scales as a plateau of low level emission, core emission must be isolated from the extended emission in order to quantitatively assess their properties. Inspection of the maps of Paper I of the ^{13}CO J=1-0 integrated intensity suggests that the cores can be isolated spatially from the parent cloud at values of integrated intensity larger than the mean plateau emission from the diffuse, ambient medium. To estimate the mean plateau value, Y_0, we define the distribution $F(Y)$ as the number of positions within the map with integrated intensity Y, binned in 0.1 K km s^{-1} intervals and estimate Y_0 as the minumum value of Y such that $(dF/dY)_{Y_0} > 0$ (Figure 1). Such a requirement ensures that the cores are defined as regions of enhanced emission, typically, $Y_0 = \langle Y \rangle + \sigma_Y$ where $\langle Y \rangle$ and σ_Y are the mean and dispersion of the distribution $F(Y)$. Since the five parent clouds studied exhibit a range of sizes (i.e. column density), the value for Y_0 is different for each cloud and are listed in Table 1. These values are somewhat arbitrarily determined and are not meant to correspond to a critical density associated with an instability mechanism but only provide a means to spatially isolate the cores from the parent cloud. The first step in the isolating procedure is to spatially separate the core by associating with a core region all positions within a given Y_0 contour level.

Figure 1. - The distribution of integrated intensities of ^{13}CO $J=1-0$ emission observed toward the B216-B217 cloud. The distribution is used to determine the plateau value of the ambient cloud in order to isolate the cores.
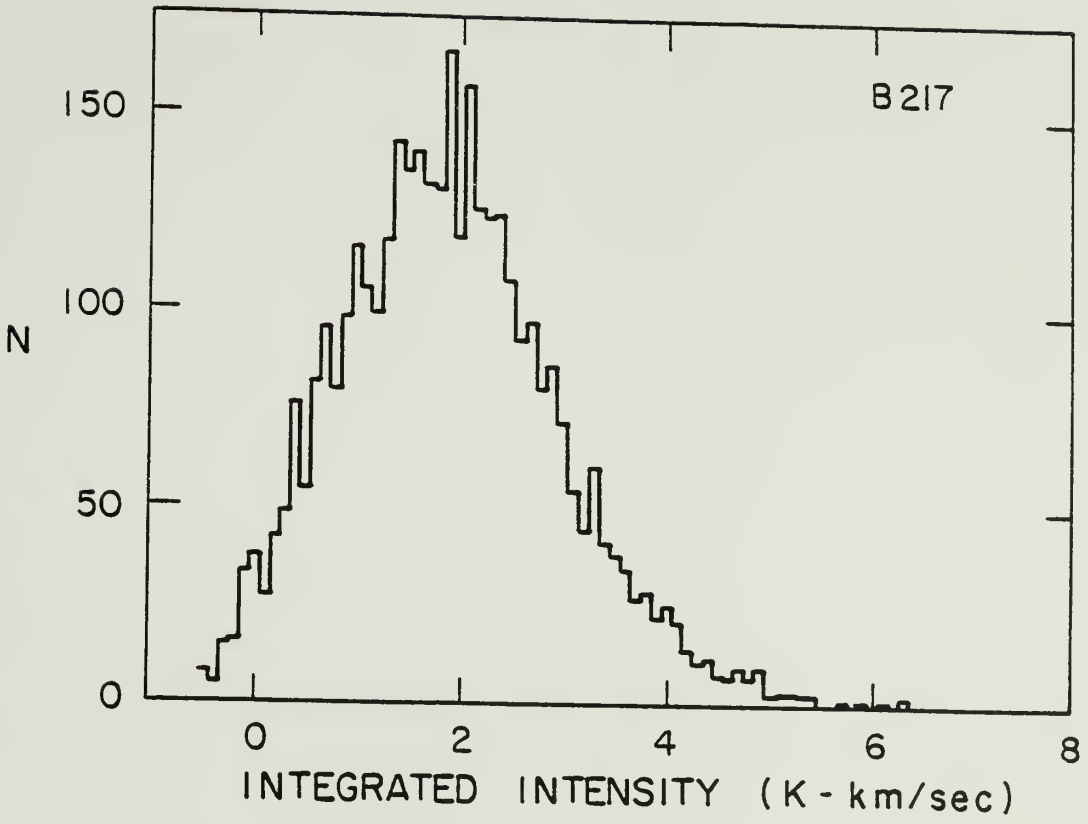
Table 1

Cloud Plateau Values

Cloud	Y_o (K km s^{-1})
Heiles Cloud 2	3.75
B216-B217	2.50
B18	3.00
L1517	1.20
L1544	1.20

Earlier studies of the Taurus Molecular Cloud have shown that multiple velocity components as seen in Figure 2, are a common feature to many molecular spectral lines (Clark, Giguerre, and Crutcher 1977; Baudry et al. 1981, Paper I). Such spectral features have been interpreted as two cores along the line of sight, possibly in orbital motion (Clark, Giguerre, and Crutcher 1977). We have attempted to identify such structure along the line of sight by fitting the sum of n Gaussian line profiles to the observed ^{13}CO spectra, where n is the number of velocity components separated by at least 0.75 km s^{-1}, determined to be present within a spatially isolated core. Because the presence of rotational motion is identified by a systematic shift in the centroid velocity, such a kinematic isolation procedure has the risk of diluting the signature of rotational motion if the total velocity shear across the surface of the cloud is greater than 0.75 km s^{-1}. However, in most cases, the separation between velocity components exceeds 1.0 km s^{-1}.

After the kinematic separation of a core, the integrated intensity associated with each velocity component in the spectrum is calculated from the fitted parameters (amplitude T_0, centroid velocity v_0, and full width half power line width Δv. The integrated intensity of each component is required to exceed the value Y_0 appropriate for the parent cloud. In most cases in which more than one velocity component is present, the spectrum associated with the peculiar velocity component with respect to the canonical velocity of the parent cloud is weak and

82

Figure 2. - An example of a ^{13}CO J=1-0 spectra which exhibits two

velocity components. The position of the spectrum is

α(1950) = 04^h 23^m 36^s; δ(1950) = 24° 33' 00" located within

the B18 cloud. The presence of secondary velocity

components necessitates a kinematic separation of cloud

cores.
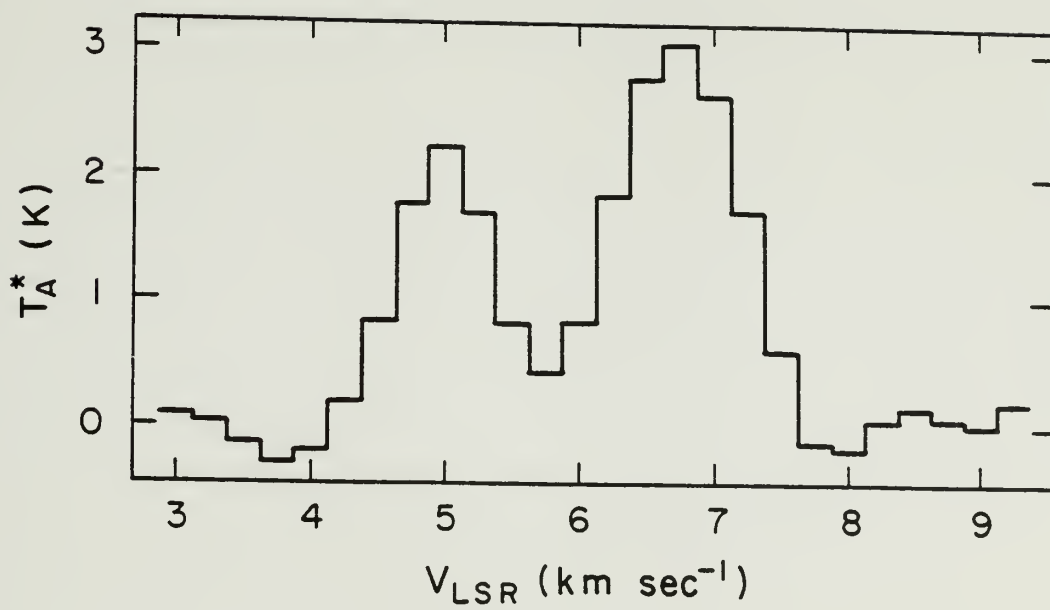
does not satisfy this last requirement. These secondary components are generally not detected with probes of high gas volume density such as NH_3 or CS (Myers and Benson 1983) indicating that the regions associated with these secondary velocity components are characterized by lower mean densities.

b) Core Properties

i) Morphology

After the spatial and kinematic separation of the cloud cores from the parent clouds, each core is described by a spatial distribution of the three fitted parameters T_0, v_0, and Δv. The mean values for these quantities as well as the geometric center positions for each core are listed in Table 2. A size r is calculated from the dispersion of positions about the geometric center, along the equatorial directions,

$$r = (\sigma_\alpha \sigma_\delta)^{1/2} \tag{1}$$

Masses for the cores are estimated from the integrated intensity of spectra generated from T_0, v_0, and Δv and the conversion factor between ^{13}CO and H_2 column densities described in Paper I. Mean densities are calculated from the relation

$$\langle n \rangle = \frac{3M}{4 \, \mu m_{H_2} r^3} \tag{2}$$

where M is the mass of the core. The mean density is likely a lower limit since we have not accounted for the flattened morphology of the cores nor the possibility of clumpy structures. Values for the core sizes, masses, and mean densities are also given in Table 2.

Table 2

Cloud Core Positions, Line Parameters and Physical Characteristics

Core	α(1950)	δ(1950)	T_0 (K)	v_0 (km s^{-1})	Δv	M (M_0)	$\langle n \rangle$ (cm^{-3})	r (pc)
HCL2-A	04 36 54	25 55 39	4.2	6.1	1.7	37.6	0.9	0.27
HCL2-B	04 36 39	25 41 15	4.6	6.6	1.1	4.0	0.2	0.20
HCL2-C	04 38 04	25 43 33	4.0	5.8	1.8	15.3	1.5	0.17
HCL2-D	04 36 53	25 34 09	4.0	6.2	1.7	5.2	2.6	0.10
HCL2-E	04 37 20	25 27 03	3.5	6.4	1.5	37.1	0.2	0.49
HCL2-F	04 38 44	25 33 15	4.0	5.9	1.6	7.6	1.7	0.13
HCL2-G1	04 38 58	25 17 03	4.3	5.5	1.1	0.6	0.1	0.18
HCL2-G2	04 39 02	25 21 45	3.4	6.9	1.6	0.3	1.2	0.05
B217-A	04 19 02	26 46 12	3.0	6.3	1.4	33.4	0.3	0.37
B217-B	04 20 35	26 29 18	2.8	6.5	1.4	30.0	0.3	0.35
B217-C	04 22 16	26 22 24	2.4	6.5	1.5	13.7	0.3	0.28
B217-D	04 23 53	26 02 00	3.0	6.3	1.1	17.6	0.4	0.27
B217-E	04 23 00	26 15 54	3.0	6.4	1.0	9.3	0.3	0.24
B217-F	04 26 15	26 08 00	3.4	6.7	1.2	5.0	0.7	0.15

B18–A	04 23 35 24 30 12	3.7	6.8	1.2	7.3	0.2	0.28
B18–B	04 26 09 24 28 54	3.7	6.5	1.4	12.3	0.4	0.24
B18–C	04 29 14 24 39 42	2.9	6.5	1.5	2.1	1.4	0.09
B18–D	04 25 00 24 35 42	3.2	6.8	1.3	1.6	0.8	0.10
B18–E	04 29 24 24 15 48	4.0	6.5	1.2	15.2	1.4	0.38
B18–F	04 28 28 24 04 24	2.9	6.0	1.6	1.4	2.0	0.07
B18–G	04 27 52 24 05 06	3.5	6.2	1.2	3.4	0.4	0.16
B18–H	04 30 57 24 03 42	3.5	6.8	1.3	2.2	0.5	0.13
B18–I	04 32 37 24 03 00	4.3	5.7	1.0	2.2	1.1	0.10
L1517–A	04 52 23 30 44 18	2.5	6.2	0.9	0.4	1.6	0.05
L1517–B	04 51 52 30 30 42	2.7	6.0	1.0	3.2	0.3	0.18
L1517–C	04 51 33 30 31 00	2.8	5.6	0.9	4.5	0.3	0.19
L1517–D	04 52 40 30 34 24	2.9	5.9	0.9	7.3	1.6	0.13
L1544–A	04 59 26 25 48 48	2.0	7.1	1.0	1.6	0.6	0.11
L1544–B	04 49 47 25 41 00	1.8	7.2	1.0	2.7	0.3	0.17
L1544–C	05 01 03 25 11 12	2.3	7.2	1.0	8.7	0.2	0.30

The observed morphology of the dense cores allows one to investigate the stresses which play a major role in their formation. The magnetic support of the parent cloud is expected to produce cores flattened along the magnetic field direction since both neutrals and ions freely collapse along the field lines restrained only by thermal and turbulent pressure while lateral collapse of the gas is inhibited by thermal, turbulent and magnetic pressures (Shu 1983). In this study, core morphology is determined from the observed column density distribution inferred from ^{13}CO $J=1-0$ emission. The two dimensional auto-correlation function (ACF) provides a useful and unbiased description of cloud structure for large data sets. Each core is individually well resolved and typically composed of several hundred data points. Following Kleiner and Dickman (1984), we define the two dimensional auto-correlation function of the spatial distribution $Y(\underset{\sim}{r})$, of a parameter as,

$$C_{ij} = \langle \langle Y_i(\underset{\sim}{r}) - \langle Y_i \rangle \rangle \langle Y_j(\underset{\sim}{r} + \underset{\sim}{r}') - \langle Y_j \rangle \rangle \rangle \tag{3}$$

where $\underset{\sim}{r}$ is the vector lag defined by a pair of positions and all brackets refer to mean quantities. We have used the intermediate bias for normalization described by Kleiner and Dickman (1984) as a compromise between the true ACF and one which suppresses large scale but low signal to noise correlations, that is, $N_c(\underset{\sim}{r}) = (N_T N_S(\underset{\sim}{r}))^{1/2}$, where $N_S(\underset{\sim}{r})$ is the number of pairs at the vector lag $\underset{\sim}{r}$ and N_T is the total number of pairs. In Figure 3, we present a contour map of the ^{13}CO $J=1-0$ integrated intensity of the isolated core B18-A and the associated ACF. The morphology of the core can be inferred from the structure of

Figure 3. - (a) Spatial distribution of integrated intensities

calculated from the amplitude, mean velocity, and velocity

width after core separation of B18-A. (b) The auto

correlation function of the spatial distribution described

by Figure 3a. Solid and dotted contours denote positive

and negative correlations respectively and are spaced by

0.1. The inner positive correlations are generally

elliptical indicative of the flattened structure of the

cloud core.
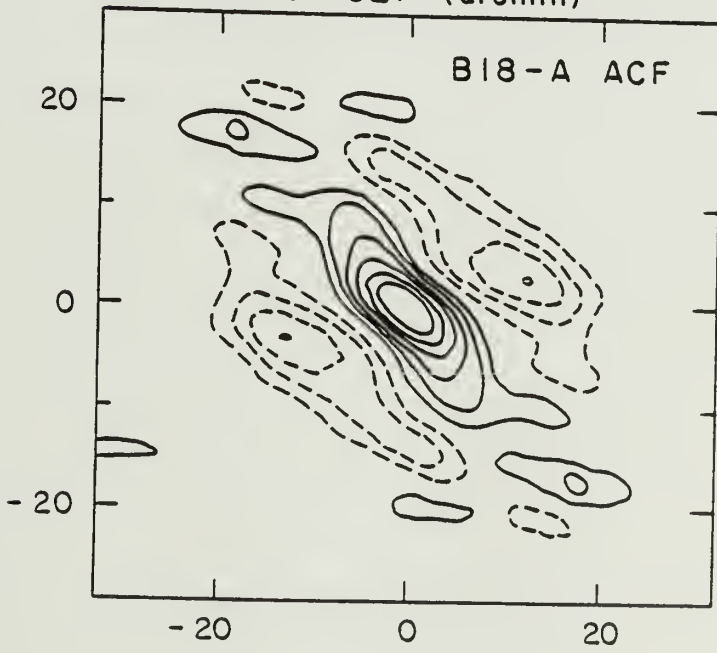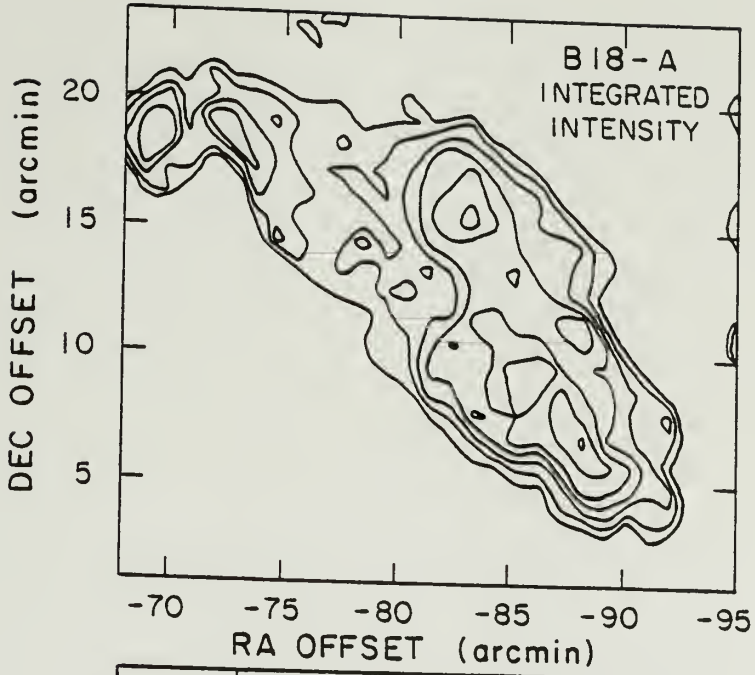
Table 3

Cloud Core Orientations

Core	b/a	B (deg)	θ (deg)	dv/dr (km s^{-1} pc^{-1})	θ$_{RT}$ (deg)
HCL2–A	0.64	50	100	0.32	140
HCL2–B	0.58	50	50	--	--
HCL2–C	0.68	50	40	1.03	130
HCL2–D	—	50	--	0.63	85
HCL2–E	0.48	50	10	0.59	110
HCL2–F	0.59	50	20	0.30	175
HCL2–G1	0.69	50	60	--	--
HCL2–G2	0.43	50	110	--	--
B217–A	0.39	31	30	0.41	120
B217–B	0.57	27	30	0.21	180
B217–C	0.75	28	60	1.19	335
B217–D	--	30	--	0.46	340
B217–E	0.92	23	170	0.37	250
B217–F	--	40	--	0.67	180
B217–G	0.72	20	20	1.40	45
B18–A	0.38	60	130	0.63	65
B18–B	0.45	66	60	0.10	225
B18–C	--	65	--	0.20	355
B18–D	--	65	--	0.75	45
B18–E	0.70	59	40	0.13	265
B18–F	--	62	--	2.69	15
B18–G	--	62	—	0.73	195
B18–H	0.74	52	50	0.67	290
B18–I	0.85	52	0	0.28	15
L1517–A	0.75	55	10	0.82	325
L1517–B	0.49	55	60	0.37	245
L1517–C	0.58	55	10	0.69	310
L1517–D	0.54	55	100	0.13	175
L1544–A	0.76	55	70	0.78	200
L1544–B	0.84	55	90	0.25	185
L1544–C	0.68	55	70	0.22	305

positive correlations centered on $(0,0)$. These small scale positive correlation features are typically elliptical in shape which is indicative of flattened cores. The orientation θ (the position angle of the minor axis) and sizes (a,b the semimajor and semiminor axes respectively) of the cores are determined by fitting an ellipse to the shape of the inner correlations at the 0.3 (3σ) level. In most cores, there is a measureable oblateness such that the orientation of the core is well defined (a typical 1σ error for θ is 10°). The orientations of the cores are summarized in Table 3.

In Figure 4, we present the observed probability distribution $P(\Delta\theta)$ of finding a core oriented with an observed magnitude offset from the magnetic field, $\Delta\theta = \theta - \theta_B$. The local field direction θ_B, is determined from the mean position angle of nearby polarization vectors presented in Paper I. The absolute value is used because of the 180° uncertainty in the magnetic field direction. From a sample of 24 cores, there is a tendency of the cores to be aligned with the direction of the magnetic field ($\Delta\theta \sim 0$). The mean and median of the distribution are 20° and 18° respectively although the dispersion is large (30°) indicating that there is no systematic alignment of the cores along the magnetic direction. Conclusions from the distribution must be drawn with caution given the small sample size.

Many of the cores exhibit a fragmented appearance denoting structure on sizes comparable to our resolution limit of 0.04 pc. While such fragmentary structure is generally not seen from NH_3 observations of

Figure 4. - The probability distribution $P(\Delta\theta)$ of finding a cloud core whose orientation θ, (defined by the position angle of the minor axis) is offset from the local direction of the magnetic field θ_B, by $\Delta\theta = \theta - \theta_B$ from a sample of 24 cores within the Taurus Cloud Complex. There is a tendency of the cores to be aligned along the magnetic field direction.
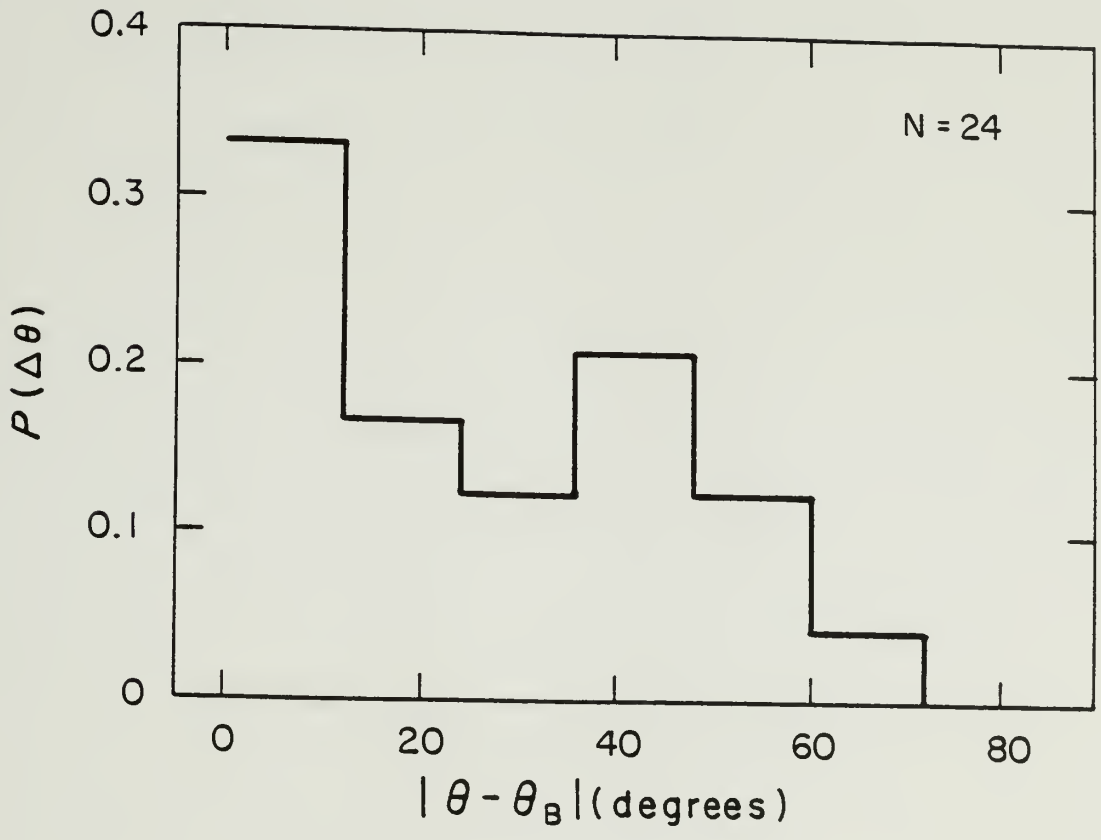
cloud cores, studies of cores which utilize CS as a probe of dense gas do detect several emission peaks (Heyer et al. 1986b) and indicate that the cores have yet to achieve a stable configuration. It is of doubtful utility to determine a density law to characterize the cloud cores given the presence of significant density inhomogeneities within the cores.

ii) Core Rotation

In Paper I, it was shown that the parent clouds exhibit systematic rotational motions with axes which are generally aligned with the magnetic field. Such alignment is consistent with models of magnetic braking in which angular momentum perpendicular to the magnetic field is more efficiently redistributed than the parallel component (Mouschovias and Paleologou 1980). Based on our sample of cores, we can extend this study to investigate the rotational motion of the gas at higher densities.

Rotational motion of an interstellar cloud is generally inferred from a systematic velocity gradient as denoted by changes in the emission centroid velocity across the cloud face (Arquilla and Goldsmith 1986). Gradients are often displayed as spatial velocity diagrams along a chosen axis of the map. Such methods are restricted to a limited, chosen strip of the data and consequently, do not define the rotational axis very accurately. In this study, it is desireable to determine the rotational axis with more precision to compare with the magnetic field direction. We have determined the direction of the rotational axis of a

core, v_{rt}, by rotating the coordinate axes $(\alpha, \delta) \rightarrow (x', y')$ such that the difference between velocity gradients along the two coordinate axes is a maximum, that is $dv_0/dy' - dv_0/dx'$ is a maximum where dv_0/dy' and dv_0/dx' are the velocity gradients determined from a least squares fit to all core centroid velocities. In addition, we require that the total velocity shear across the length of the core exceed 0.2 km s^{-1} (local sound speed) to ensure that the shift is not due to random, thermal motions. Such a requirement sets a lower limit to the velocity gradient to which we are sensitive of 0.1/r km s^{-1} pc^{-1} where r is the radius of the core in pc. In Figure 5, we present evidence for rotation of the core B217-G, defined by this procedure. A summary of the rotational properties of the cloud cores is given in Table 3. Most of the cloud cores show some evidence for rotational motion with velocity gradients ranging from 0.1 to 2.7 km s^{-1} pc^{-1}. In all cases, the total velocity shear is small with respect to the ^{13}CO line widths indicating a small role of the centrifugal stress in the dynamics of cloud cores.

Caution must be given to determining rotation in the presence of secondary velocity components. In one case, (B18-E or L1535), claimed by Goldsmith and Sernyak (1984) to be rotating about an axis with a positional angle of -45°, the process of kinematic separation suggests that this earlier claim of rotation is a reflection of the shift between two distinct velocity components. While the bulk of the angular momentum may reside in the orbital motion of two cores, as given by the two velocity components, the spin axis of the core associated with

Figure 5. - A plot of the emission centroid velocity v_o, versus offset from the geometric center along an axis y', rotated from the equatorial coordinates such that $dv_o/dy' - dv_o/dx'$ is a maximum, indicative of rotation of the cloud core.
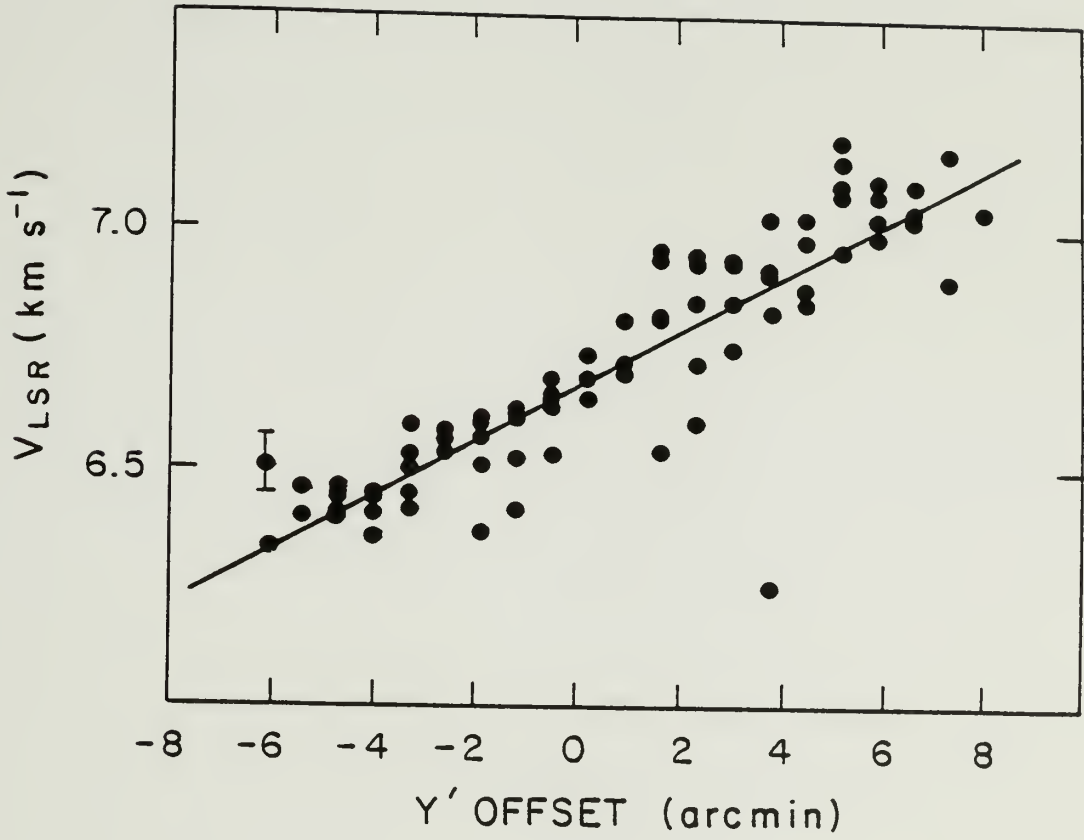
embedded NH_3 core (by virtue of similar mean velocities) is parallel to the axis inferred from the NH_3 emission.

In Figure 6, we present the observed probability distribution, $R(\Delta\theta_{rt})$, of finding a core with a rotational axis direction offset from the direction of the magnetic field by an angle, $\Delta\theta_{rt} = \theta_{rt} - \theta_B$. From a sample of 18 cores which showed evidence for rotational motion, there appears to be no tendency for alignment of rotational axes along the magnetic field direction. The apparent random distribution of rotational axes suggests that the process of magnetic braking is not important in redistributing angular momentum at the densities which characterize cloud cores. In addition, the values of the calculated velocity gradients indicate that a significant amount of angular momentum is still present in these regions.

DISCUSSION

i) Decoupling of the Magnetic Field

The large dispersion of the core orientation and the apparent random distribution of rotational axes are puzzling since the parent clouds are so well ordered. Toward the dense cores we find (1) only a small trend for the minor axes of the cores to be aligned along the direction of the magnetic field, and (2) randomly distributed rotational axes. Given the apparent magnetically dominated evolution of the parent clouds, we believe that the magnetic field has fully decoupled from the gas at the

Figure 6. – The probability distribution $R(\Delta\theta_{rt})$ of finding a core with

a rotational axis direction θ_{rt} offset from the local

magnetic field direction $\Delta\theta_{rt} = \theta_{rt} - \theta_B$ from a sample of 18

rotating cores in the Taurus Cloud Complex. The

distribution appears random suggesting that the magnetic

field has decoupled from the gas and that magnetic braking

is not responsible for fully redistributing angular

momentum on the sizes and densities of cloud cores.
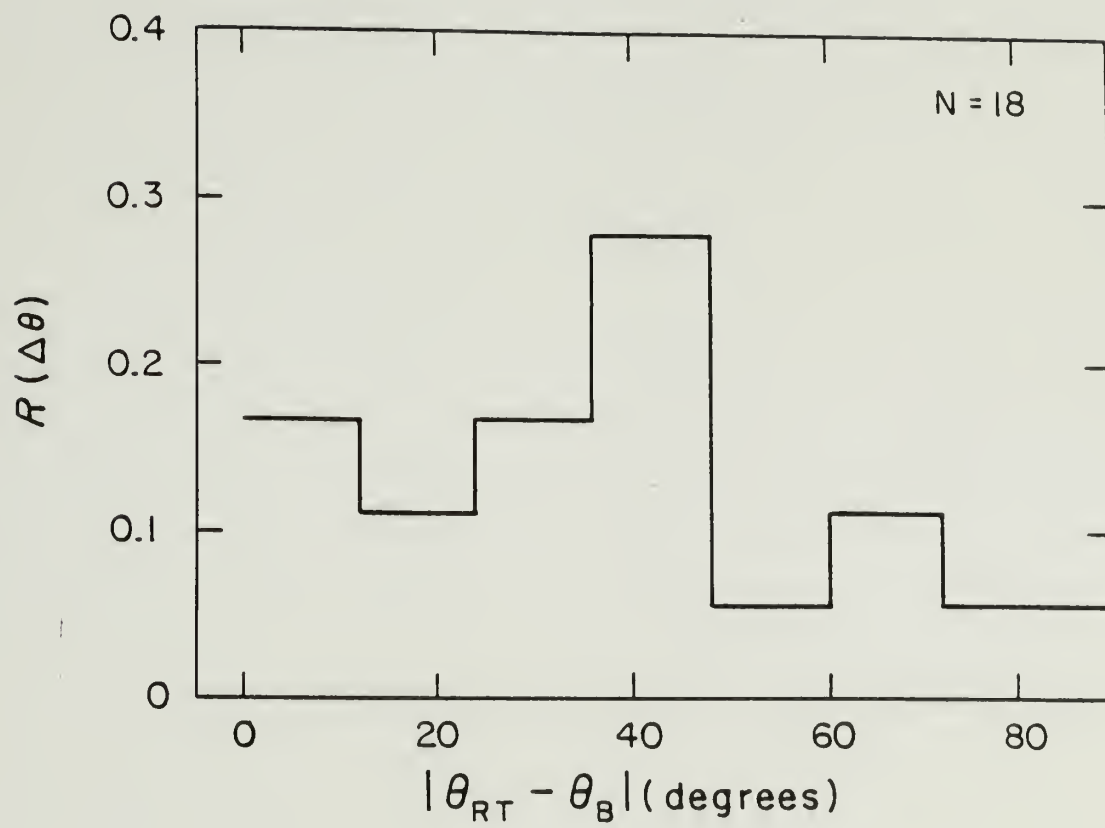
<u>characteristic densities of cloud cores, 10^4 cm^{-3}.</u> Theoretical

arguments on the critical densities at which the magnetic field

decouples from the gas based on detailed calculations have suggested

similar mean values (Mouschovias and Paleologou 1980). In particular,

calculations which account for the momentum exchange assuming both slow

and rapid ionization rates with respect to the cloud free-fall time

scale indicate critial densities $< 10^6$ cm^{-3} (Mouschovias and

Paleologou 1981). Mouschovias (1977) estimates a range of critical

densities $7.5 \times 10^3 < n_c < 2.2 \times 10^6$ cm^{-3} to account for the observed range

of periods for binary stars (100 years to 10 hours). In this scenario,

magnetic braking is an effective mechanism in the redistribution of

angular momentum until the magnetic field decouples from the gas. After

magnetic field decoupling, only fragmentation of the core, which

ultimately results in a binary or multiple system, allows the angular

momentum to be redistributed into the orbital motion of the fragments.

Hence, our observed estimate of the critical density at which the field

decouples from the gas is consistent with theoretical estimates though

somewhat toward the low end of this range. The time scale τ_D for the

magnetic field to diffuse from the neutral gas component is given by

$\tau_D = 5 \times 10^{13}$ x years where x is the degree of ionization of the cloud

(Spitzer 1978). A lower limit to the value of x in molecular clouds can

be determined from the abundance of one of the dominant ions HCO$^+$. The

fractional abundance of HCO$^+$ has been determined by Guelin et al. (1982)

to be 8×10^{-9}. Thus, the minimum time scale for the magnetic field to

diffuse from the cloud is 4×10^5 years. Chemical modeling of dense

molecular clouds suggests that the ionization fraction is more likely 10^{-7}, (Graedel et al. 1982) which would increase the diffusion time scale to 5×10^{6} years.

ii) Core Formation

The result of the magnetic field decoupling from the gas component is a density enhancement with respect to the surrounding medium based on one dimensional calculations (Shu 1983). While a more realistic model of the cores must await detailed three dimensional studies of ambipolar diffusion, one might expect the cores, as determined from ^{13}CO observations, to be flattened along the magnetic field direction. In regions of low densities required to excite the ^{13}CO J=1-0 transition, the gas is presumably sufficiently ionized to be strongly coupled to the magnetic field. In regions of high density, the field no longer provides a mechanism of support from gravity. Rather, thermal and turbulent pressures are likely to be the dominant internal stress counteracting gravity and provide isotropic pressure which might shape the dense core into the round, symmetric configurations usually seen in maps (resolution > 0.03 pc) of NH_3 emission (Myers and Benson 1983; Gaida et al. 1984). While there exists a trend of the cores to be oriented along the magnetic field direction, it is not so striking as to confirm the role of ambipolar diffusion in the formation of cloud cores.

It is possible that fragmentation mechanisms have contributed to the clumpy nature of molecular clouds (Scalo 1985). Mestel (1977) has

demonstrated that the gravitational force exceeds the magnetic force if collapse of the parent cloud is uniform, non-isotropic, and the magnetic flux is frozen into the gas (B $\propto n^k$, $1/3 < k < 1/2$, Mouschovias 1976). Since the magnetic Jeans' mass is proportional to the quantity B^3/n^2, such a scaling of the magnetic field strength with density allows fragments to condense as the parent cloud collapses quasi-statically. In the event of non-flux freezing conditions, the value of k can be even less than the lower limit of Mouschovias (1/3, 1976) and fragments can more readily condense from the parent cloud.

Alternatively, numerical calculations show that rotating, interstellar clouds are inherently unstable to non-axisymmetric perturbations (Boss 1980). Such perturbations may be common in a turbulent medium which may characterize molecular clouds (Dickman 1985). However, it is not certain that such instabilities produce the flattened cores that are observed here.

iii) Angular Momentum Problem

The observed core rotational rates, ι^{-14} rad s^{-1} indicate a significant amount of angular momentum present at the sizes and densities of cloud cores. Such a large angular frequency of the cores implies a stellar rotational rate of $\Omega = 0.1$ rad s^{-1} if angular momentum is rigorously conserved in the collapse of the core to the radius associated with a star. The observed rotational frequencies of pre-main sequence stars is typically 4×10^{-5} rad s^{-1} (Vogel and Kuhi 1981;

Hartmann et al. 1986). In Paper I, it was demonstrated that the rotational axes of the parent clouds are approximately aligned with the magnetic field direction suggesting that magnetic braking is a very efficient process at densities less than 10^3 cm^{-3}. The apparent random distribution of core rotational axes seen in Figure 6 and the values of inferred rotation rates suggest that magnetic braking has not slowed the cores to values associated with observed stellar angular momenta and has not solved the angular momentum problem. Furthermore, since the magnetic field has likely decoupled from the gas at these high densities, it can no longer efficiently redistribute angular momentum. Mechanisms for redistributing angular momentum must apparently operate at smaller sizes or during free fall collapse. Boss (1980) has shown that a significant fraction of the original angular momentum of the core may be redistributed into the orbital motion of fission products that are predicted as a result of dynamical collapse. Alternatively, the residual angular momentum may be lost via the stellar winds which are associated with young stellar objects (Hartmann and MacGregor 1980). These winds effectively transport angular momentum and can provide the necessary braking to account for the rotational velocities observed in pre-main sequence stars.

Since the rotation of the stars is derived from the initial angular momentum of the parent cloud, one might expect alignment of the rotational axes of cores, stars, and binary orbits within a star forming region in the absence of collisions. Such alignment is not present in

the cloud cores studied nor is it seen in the stellar population of the Orion association (Kraft 1970). It is likely that the randomization of rotational axes occurs during the dense core phase via gravitational interactions with other cores, physical collisions, or coupling to turbulent eddy currents. The time scale for a collision between cores is given by

$$\tau_{coll} = \frac{4R_p^3}{3Nr^2 \langle v \rangle} \tag{1}$$

where R_p is the parent cloud radius, r is a typical core radius, N is the number of cores within the parent cloud, and $\langle v \rangle$ is the relative velocity between cores. For the parent clouds and cores in this study, $R_p = 1$ pc, r = 0.25 pc, and N = 8. We estimate $\langle v \rangle$ from the dispersion of the mean velocities of the cores within the parent cloud, tabulated in Table 1 and apply a correction factor $(3)^{1/2}$ to account for motion in three dimensions and find $\langle v \rangle = 0.6$ km s^{-1}. The collision time scale is estimated to be 4×10^6 years. Thus, cloud cores must be long lived (several collision time scales) in order to experience one or more collisions to randomize the rotational axis directions. Such longevity may indicate the presence of substantial non-magnetic internal pressure (thermal or turbulent) to counteract the gravitational force and prevent the dynamical collapse of the core over this time scale.

CONCLUSIONS

In this study, we have attempted to characterize the properties of molecular cloud cores defined by enhanced ^{13}CO emission in terms of

their morphology and kinematics with respect to the local magnetic field direction in order to assess the role of the interstellar magnetic field in the evolution of the gas at densities greater than 10^4 cm^{-3}. The cores are found to be generally flattened with a distribution of minor axis core orientations only moderately aligned with the magnetic field direction. Evidence for rotation is found in 18 cores but with rotational axes randomly distributed with respect to the direction of the local magnetic field. We believe that the random orientations of the cloud morphology and rotational axes in the plane of the sky are a reflection of the decoupling of the magnetic field from the gas at densities characteristic of these regions and collisions between cores which tend to reorient the cores' rotational axes. However, it is not possible to distinguish with certainty, the role ambipolar diffusion has played in the formation of cloud cores from fragmentation processes. The values of the velocity gradients ($\Omega \sim 0.5$ km s^{-1} pc^{-1}) due to rotation determined to be present in the cloud cores suggest that the angular momentum problem associated with star formation is not completely resolved by magnetic fields at the time of dense core formation by magnetic braking.

CHAPTER IV.

Mass Outflows and the Kinematics of Molecular Clouds

INTRODUCTION

Our understanding of the internal kinematics of interstellar clouds
remains incomplete owing to the complex velocity fields typically
observed. These motions are characterized by supersonic line widths
seen in most spectral lines and the presence of multiple velocity
components along the line of sight (Clark, Gigurre, and Crutcher 1977;
Baudry et al. 1981; Heyer et al. 1986). Attempts to resolve these
motions as systematic free-fall collapsing motion (Goldreich and Kwan
1974) have failed since such universal and rapid collapse of molecular
clouds would predict a star formation rate incompatible with the value
observed in the Galaxy (Zuckerman and Evans 1974). Rather, the observed
kinematics are often attributed to a random velocity component or
turbulent motion. The observed line widths may reflect the relative
motion of many small clumps, each having a nearly thermal line width
along the line of sight (Zuckerman and Evans 1974; Kwan and Sanders
1986). However, such supersonic gas motions are expected to be rapidly
dissipated by radiative energy losses due to strong shocks which result
from the inevitable collisions between the clumps. Scalo and Pumphrey
(1982) have shown that most of these collisions are in fact oblique and
consequently, the turbulent motion is not subject to such large

radiative losses. They estimate a time scale for turbulent dissipation
of approximately seven free-fall time scales or typically 10^7 years.

In order for turbulent motion to be responsible for the longevity
of molecular clouds, there must be a source which feeds energy into the
gas motions at a rate comparable to the dissipation rate. There are
many possible sources in the interstellar medium. Rotational shear,
ultimately generated by the differential rotation of the Galaxy can
externally inject energy into the larger size scales of the interstellar
medium which presumably cascades and finally is dissipated at the
smallest scales (Fleck 1981). However, such Kolmogorov type turbulence
may not be applicable to the interstellar medium (ISM) since it requires
dissipationless energy transfer between each scale in the hierarchy of
interstellar cloud structures, a condition unlikely to be present in the
compressible and radiative ISM. Norman and Silk (1980) have suggested
that winds from T Tauri stars, inferred from P Cygni line profiles of
Hα emission, which have formed within the clouds are responsible for
providing an internal source of turbulent energy. If the star density
exceeds a critical value, then the expanding shells driven by the
stellar winds can intersect, coagulate and eventually evolve as sites of
future star formation. More recently, it has been realized that most
pre-main sequence stars directly interact with the environment from
which they condensed via stellar winds. Such outflow activity is
observed as broad line wing ^{12}CO J=1-0 emission (Snell, Loren, and
Plambeck 1980; Goldsmith et al. 1984) due to accelerated ambient cloud

gas and optically as collimated jets of shock excited emission (Mundt and Fried 1983; Strom et al. 1986). Energies of the winds from these young stellar objects are much larger than those associated with T Tauri stellar winds and may provide a more potent source of energy. Moreover, this more energetic phase may occur at an earlier epoch of pre-main sequence evolution, when the stars are still deeply embedded within the parent cloud, possibly allowing more efficient transfer of the wind energy to the parent cloud. A recent study of the B5 cloud has found that the stellar winds from four embedded protostars have injected energy into the 340 M_0 cloud comparable to the gravitational energy of the cloud and in two regions, have significantly dispersed the local material (Goldsmith et al. 1986).

To investigate the role of protostellar winds as a source of turbulent energy, we have studied local star forming regions within the Taurus Molecular Cloud. The Taurus Cloud contains the prototype of mass outflow from a young stellar object in IRS5-L1551 (Snell, Loren and Plambeck 1980) as well as outflows associated with HL/XZ-Tau (Calvet et al. 1983), T Tau (Edwards and Snell 1983) and L1489-FIR (Myers et al. 1986). In addition, there are several young stellar objects with associated shock excited nebulosity in the form of stellar jets (Strom et al. 1986). In earlier studies (Heyer et al. 1986; Heyer 1986), it was demonstrated that the magnetic field has played an important role in the evolution of the gas at low densities in the Taurus Cloud but has since decoupled from the gas in the more condensed regions allowing star

formation to proceed uninhibited by the magnetic stress. Thus, it is important to the subsequent evolution of the region whether mass outflows can support the cloud against further collapse.

Essential to this model of stellar wind driven turbulence are the number and mean energetics of outflows within the cloud. Using the IRAS Point Source Catalog (1985) as a guide to recent star forming regions, we have surveyed the ^{12}CO and ^{13}CO J=1-0 emission within the 4'x4' region surrounding 30 young stellar objects within the Taurus Molecular Cloud. A description of the data acquisition is presented in Section II and in Section III, we discuss the survey strategy and present maps of three newly detected molecular outflows. In Section IV, the role that the stellar winds play in providing the neccessary energy to support the cloud against gravitational collapse is discussed, and the implications for future star formation in the Taurus Cloud are presented.

OBSERVATIONS

Molecular line observations were obtained with the 14 meter telescope of the Five College Radio Astronomy Observatory. A quasi-optical single sideband filter and a 256 channel spectrometer with 100 KHz (0.26 km s^{-1}) resolution per channel were employed with a cryogenic Schottky diode mixer receiver. Calibration of the data was obtained with the use of a chopper wheel which allowed switching between sky and an ambient load. The data were taken in a position switching mode between the source and a nearby reference location in the sky with no detectable CO emission.

Measurements of the Moon and Jupiter were used to determine the full width half power beam width (θ_{FWHP}) and the efficiency on a spatially extended source (η_{FSS}) much larger than the main beam. At the rest frequency of the ^{12}CO (115.271203 GHz) and ^{13}CO (110.20137 GHz) J=1-0 transitions, the values for θ_{FWHP} and η_{FSS} are 45" and 0.70 respectively at the ^{12}CO frequency and 47" and 0.70 respectively at the ^{13}CO frequency. Temperatures T_R^* quoted in this study have been corrected for ambient temperature losses, effects of the Earth's atmosphere, and for forward spillover and scattering losses (η_{FSS}, Kutner and Ulich 1981). To determine the radiation temperature T_R, a further correction is necessary to account for the source brightness distribution to fill the error pattern of the telescope (η_C). For the source sizes observed in this study, 2', $\eta_c(2') = 0.70$. In calculating luminosities and CO parameters, we have used the distance of 140 pc to the Taurus Cloud Complex (Elias 1978).

RESULTS

a) Survey

The sample of far infrared sources was selected from the IRAS Point Source Catalog (1985). Initially, the sources chosen were ones which exhibited strong 60μ and 100μ emission and located near or within a region of high visual extinction. Additional sources were observed later which showed a steep rise in flux between the 25μ and 60μ bands. In Table 1, the IRAS positions, fluxes, and far infrared luminosities

Table 1

IRAS Point Sources: Positions and Fluxes

IRAS Name	α(1950)	δ(1950)	S12	S25	S60	S100	L (L_O)
				(Janskys)			
04108+2803	04 10 48.0	28 03 49	0.87	3.88	7.38	10.57	0.4
04112+2820 FN Tau	04 11 8.6	28 20 27	0.59	1.40	1.70	-15.42	0.5
04112+2803	04 11 11.5	28 03 26	2.26	3.61	3.24	-15.42	0.5
04145+2812 Elias-1	04 15 34.5	28 12 01	33.50	91.80	65.40	151.50	20.0
04166+2706	04 16 38.3	22 53 13	-0.46	1.25	5.70	15.75	0.3
04169+2702	04 16 54.6	27 02 48	0.78	5.22	16.81	17.07	0.6
04189+2650 Haro6-5	04 18 57.6	26 50 28	1.46	3.83	6.94	-10.71	0.4
04239+2436	04 23 55.2	24 36 54	1.71	7.00	15.06	15.49	0.7
04240+2559 DG Tau	04 24 00.4	25 59 30	9.29	19.57	38.84	45.15	2.3
04243+2253	04 24 20.7	22 53 13	-0.46	1.25	5.70	15.75	0.3
04248+2612 HH31	04 24 53.2	26 12 39	-0.36	1.33	4.55	9.03	0.2
04264+2426 Haro6-10	04 26 21.7	24 26 26	14.91	38.87	59.31	46.40	3.7
04264+2433 Elias-6	04 28 28.0	24 33 23	0.44	2.91	5.29	-8.85	0.3
04278+2435 ZZ Tau	04 27 50.6	24 35 24	0.77	1.33	3.31	4.19	0.2

			0.38	1.03	2.51	5.55	0.1
04288+2417 HK Tau	04 28 48.7	24 17 58	0.38	1.03	2.51	5.55	0.1
04292+2422 Haro6-13	04 29 13.2	24 22 39	1.06	3.98	7.05	9.54	0.4
04297+2923	04 29 39.6	29 23 38	1.30	5.95	39.38	51.68	1.2
04299+2915	04 29 55.3	29 15 26	-0.47	1.44	13.57	34.95	0.5
04319+2422 AA Tau	04 31 53.5	24 22 44	0.39	0.61	1.20	-10.18	0.1
04325+2402	04 32 31.6	24 02 08	-0.25	2.11	12.69	21.86	0.4
04329+2248	04 32 53.1	22 48 18	2.06	3.67	8.34	16.16	0.5
04353+2604 DO Tau	04 35 23.9	26 04 51	1.91	3.89	5.84	6.30	0.4
04362+2547	04 36 09.4	25 47 27	1.82	18.89	44.45	34.74	1.6
04365+2535	04 36 31.0	25 35 52	1.19	8.64	35.73	38.51	1.1
04368+2557	04 36 49.3	25 57 16	-0.25	0.75	17.58	72.18	0.7
04369+2539 IC 2087	04 36 54.6	25 39 17	5.03	6.81	7.16	17.74	0.9
04380+2553	04 38 02.3	25 53 51	0.74	1.06	10.84	17.87	0.4
04381+2540	04 38 07.6	25 40 48	0.44	2.70	10.15	13.55	0.4
04385+2550 Haro6-31	04 38 34.2	25 50 43	0.54	1.55	2.83	-7.80	0.2
04525+3028 AB Aur	04 52 33.8	30 28 20	27.17	48.09	105.30	112.80	6.1
Ref #1	04 28 40.0	24 00 00	--	--	--	--	--
Ref #2	04 30 40.0	24 50 00	--	--	--	--	--

(based on the 12, 25, 60, and 100µ fluxes) are given for the thirty point sources studied. We note that the point source 04145+2812 is the sum of two known pre main sequence stars (Elias 1 and Hubble 4), that are not resolved in the IRAS Point Source Catalog but can be distinguished in the IRAS co-added data. For our study, it is useful to use the far infrared color index criteria described by Emerson (1985) to distinguish between T Tauri stars and young stellar objects deeply embedded within the cloud. Presumably, the embedded objects represent an earlier evolutionary phase than the T Tauri stars.

Our strategy to search for high velocity molecular gas was to make 3x3 point maps with 2 arcminutes spacing of the ^{12}CO J=1-0 emission centered on each of the young stellar objects of interest. It is important to search over an extended region since the high velocity gas is often displaced several arcminutes from the central source (Snell, Loren, and Plambeck 1980; Goldsmith et al. 1984). A similar 3x3 point map was made of the local ^{13}CO emission to define the ambient cloud velocity structure. In addition, results from previous studies of extensive ^{13}CO mapping of the Taurus Cloud, indicate that most of the emission from the parent clouds of the young stellar objects studied is restricted to the V_{lsr} range 3.5 to 7.5 km s^{-1} (Schloerb and Snell 1984; Heyer et al. 1986). Thus, emission outside of this velocity range might be due to the presence of high velocity outflow.

Toward most regions in our survey, the ^{12}CO J=1-0 line shapes are complex, showing evidence for multiple velocity components and self

absorption. The line widths are typically $2 - 3$ km s^{-1} and in many cases, the lines are broadened by the presence of secondary velocity components. Many of these secondary velocity components exhibit weak ^{13}CO emission relative to ^{12}CO emission with respect to the values typically observed toward dark clouds. Several examples of spectra exhibing such kinematic structure are shown in Figure 1 (04291+2923, 04108+2803 and 04264+2426). To determine if the presence of secondary velocity features are unique to regions of local star formation, we have also observed two reference locations within the Taurus Cloud which appear to have no star formation taking place nearby. We found that these spectra also exhibit multiple velocity components. Thus, multiple velocity components are possibly not unique to regions within the cloud associated with young stellar objects.

To characterize the regions associated with the IRAS point sources, and the two reference positions, we have calculated an average spectrum from the nine individual ^{12}CO J=1-0 spectra that make up the 3x3 map. A summary of the observed line parameters including the peak antenna temperature T_0, the centroid velocity v_0, the full width half power line width, v_{FWHP} and the line width measured at the 200 mK level $\Delta v(200$ mK) determined from the averaged spectrum is given in Table 2.

The nine point maps were extended if any of the spectra showed significant line wings or velocity components outside of the velocity range in which most of the ^{13}CO emission was confined. The maps of six sources were supplemented with additional observations. To be certain

Figure 1. – ^{12}CO and ^{13}CO spectra toward several IRAS point sources
showing secondary velocity components with peculiar ^{12}CO
opacities or broad line wings. These sources are typically
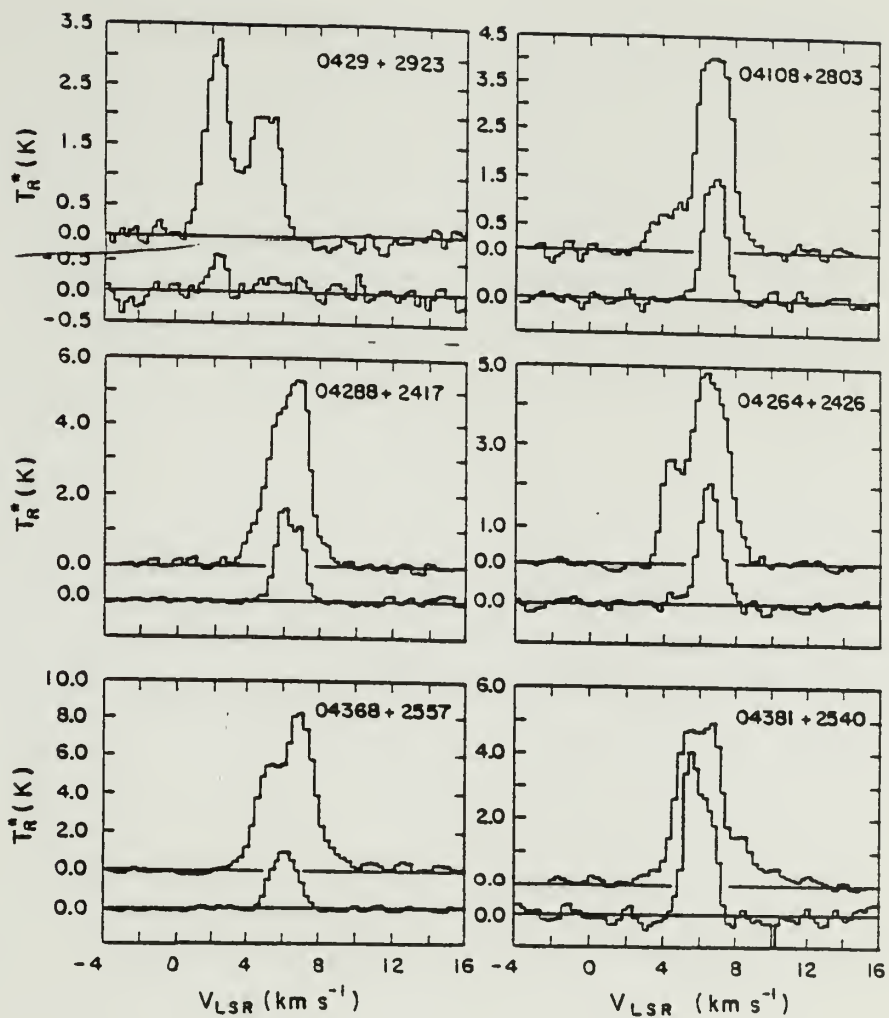embedded objects based on the far infrared colors.

Table 2

^{12}CO Line Parameters

Source	T_o (K)	v_o	Δv_{FWHP} (km s^{-1})	$\Delta v(200$ mK)
04108+2803	4.7	6.5	2.2	7.0
04112+2820 FN Tau	6.2	6.6	2.2	6.4
04112+2803	5.9	6.3	2.7	6.5
04145+2812 Elias-1	7.3	6.8	2.0	5.3
04166+2706	4.7	6.5	2.8	4.7
04169+2702	5.1	6.3	2.5	4.8
04189+2650 Haro6-5	4.0	6.2	2.5	4.4
04239+2436	6.1	6.3	2.1	5.7
04240+2559 DG Tau	5.1	6.5	2.0	4.8
04243+2253	3.3	5.9	1.8	3.0
04248+2612 HH31	4.5	7.1	2.2	4.8
04264+2426 Haro6-10	6.9	6.3	3.1	5.4
04264+2433 Elias-6	6.1	6.2	3.0	6.4
04278+2435 ZZ Tau	5.5	6.2	2.4	5.2
04288+2417 HK Tau	7.6	6.1	2.6	5.7
04292+2422 Haro6-13	5.4	5.9	3.0	5.2
04297+2923	4.7	2.7	2.5	5.7
04299+2915	4.2	3.7	2.8	5.9
04319+2422	5.5	5.4	2.1	6.0
04325+2402	7.4	6.3	2.0	4.3
04329+2248	4.4	5.5	2.6	5.0
04353+2604 DO Tau	5.4	6.1	2.8	5.9
04362+2547	6.0	6.2	2.7	5.1
04365+2535	6.8	6.1	2.5	5.2
04368+2557	6.5	6.4	3.2	6.3
04369+2539 IC 2087	6.9	6.6	2.8	7.3
04380+2553	5.1	5.9	2.8	4.6
04381+2540	5.3	6.4	3.2	7.4
04385+2550 Haro6-31	4.1	5.8	2.5	4.9
04525+3028 AB Aur	7.4	5.7	1.1	3.3
Ref #1	7.2	5.9	2.7	5.8
Ref #2	4.3	5.5	2.1	3.6

that the large gas motions that were found were really the result of mass outflow from that source, we required that the signature for high velocity gas be confined to a region immediately surrounding the IRAS source. Only three sources were found to contain localized high velocity emission; these are 04278+2435 (ZZ Tau), 04325+2402, and 04369+2539. In addition, three sources, 04362+2547, 04368+2557, and 04381+2540 showed striking line wings (see Figure 1). These could be additional outflows in Taurus, but based on our observations, we can not be certain. The three outflows that were followed up in more detail are discussed in the following section.

b) Individual Outflow Sources

i) IRAS 04278+2435 (ZZ Tau)

ZZ Tau is a T Tauri star located within the dark cloud filament Barnard 18 (B18). Herbig and Rao (1972) identify its spectral type as M4 but note that only the H and K CaII lines are seen in emission. Its far infrared spectrum identifies it as a T Tauri star from the color index criteria described by Emerson (1985). It appears relatively isolated from regions of high visual extinction as viewed on the red Palomar Sky Survey photographs. Indeed, the position of ZZ Tau coincides with the center of a region with low column density with a radius of 0.5 pc seen in the maps of ^{13}CO emission presented by Heyer et al. (1986).

A sequence of ^{12}CO spectra whose positions trace the high velocity gas is displayed in Figure 2. Red wing emission near the star develops

Figure 2. - A sequence of ^{12}CO spectra at positions along the red lobe
toward ZZ Tau showing the spatial dependence of high
velocity emission. The asymmetric line shape close to the
star develops into a distinct velocity component.
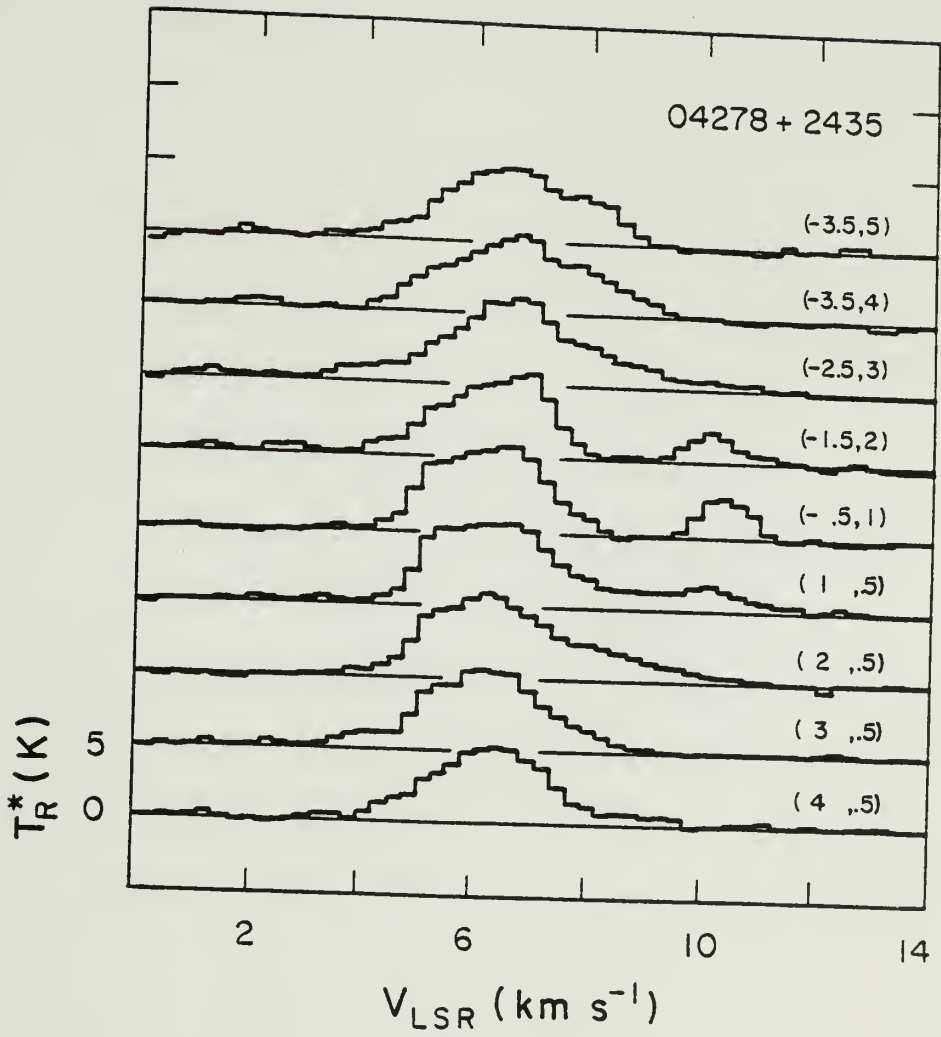
into a distinct velocity component at 10.25 km s^{-1} at positions several arcminutes from ZZ Tau and then rapidly diminishes. This component may be emitted from a shell of swept-up ambient gas located at the periphery of the outflow. A similar structure is also seen in the outflows associated with IRS5-L1551 (Snell and Schloerb 1985) and T Tau (Edwards and Snell 1982). The symmetric region of low column density that surrounds ZZ Tau may be the result of the outflow effectively dispersing the ambient material. There is little evidence for any significant blue shifted emission. A map of high velocity gas sampled at 1' spacing of 52 ^{12}CO J=1-0 spectra over the velocity interval 8 to 12 km s^{-1} is shown in Figure 3. The high velocity red wing emission has a maximum at an offset (1,1) with a secondary peak at (-2,3) where the 10.25 km s^{-1} component is most prominent.

ii) IRAS 04325+2402

The IRAS source 04325+2402 is located within the L1535 dark cloud, a small fragment located at the eastern end of the B18 cloud complex. It is the only IRAS point source within B18 that has been identified with certainty (based on its far infrared colors, Emerson 1985) as an embedded object. It is not associated with any optical object on the Red Palomar Sky Survey Plate. The star is within the boundaries of a dense core delineated by the NH$_3$ observations of Menten et al. (1984). From ^{13}CO observations, Heyer (1986) found two distinct velocity components present in the region at velocities 5.7 and 6.7 km s^{-1}.

Figure 3. - A map of integrated ^{12}CO intensity over the velocity interval 8 to 12 km s^{-1} toward ZZ Tau. There is no significant blue wing emission present in the region.
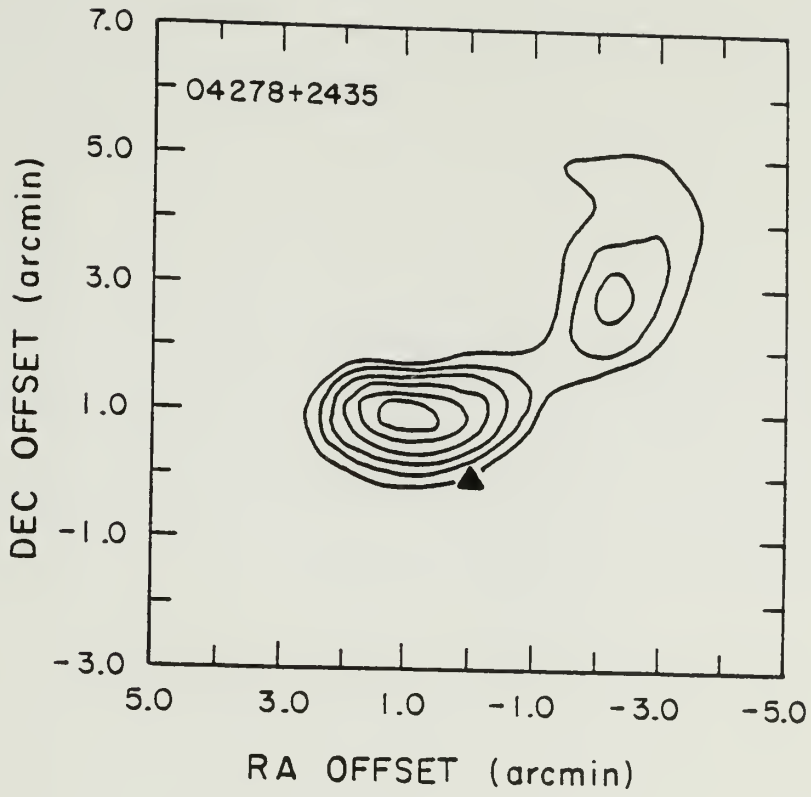
Evidence for high velocity motions in the ^{12}CO and ^{13}CO spectra obtained at two locations near 04325+2402 is shown in Figure 4. Figure 5 displays a sequence of ^{12}CO spectra along the flow which demonstrates similar spatial structure of the high velocity component as seen toward ZZ Tau. Close to the star, the mass outflow appears as asymmetric red wing emission. At positions more distant from the star, the high velocity emission is manifested as a distinct velocity component at a velocity of 8.0 km s^{-1} which is seen as only weak ^{13}CO emission. This component may be due to emission from material in a slow moving shell but the velocity is only 1 km s^{-1} higher than the known components of the ambient cloud. A map of the high velocity emission of 64 positions, sampled every 2', and integrated over the velocity interval 8.5 to 12 km s^{-1} is shown in Figure 6. We have conservatively limited the velocity range to 8.5 to 12 km s^{-1} to exclude the strong 8 km s^{-1} feature. The outflow appears large (0.6 pc), well collimated and monopolar.

iii) IRAS 04369+2539 (IC 2087)

The IRAS source 04369+2539 lies within the area of Heiles Cloud 2. Allen (1972) first detected the star at 2μ. The optical counterpart to the star was identified by Allen and Penston (1975) on the Red Palomar Sky Survey plate. Subsequently, Elias (1978) measured its near infrared spectrum and determined that the visual extinction, A_v to 04369+2539 is 17 magnitudes although this could be due in part to circumstellar material. Its far infrared spectrum measured from IRAS indicate its

Figure 4. - ^{12}CO and ^{13}CO spectra toward the peak position of high velocity emission toward the IRAS source 04325+2402.
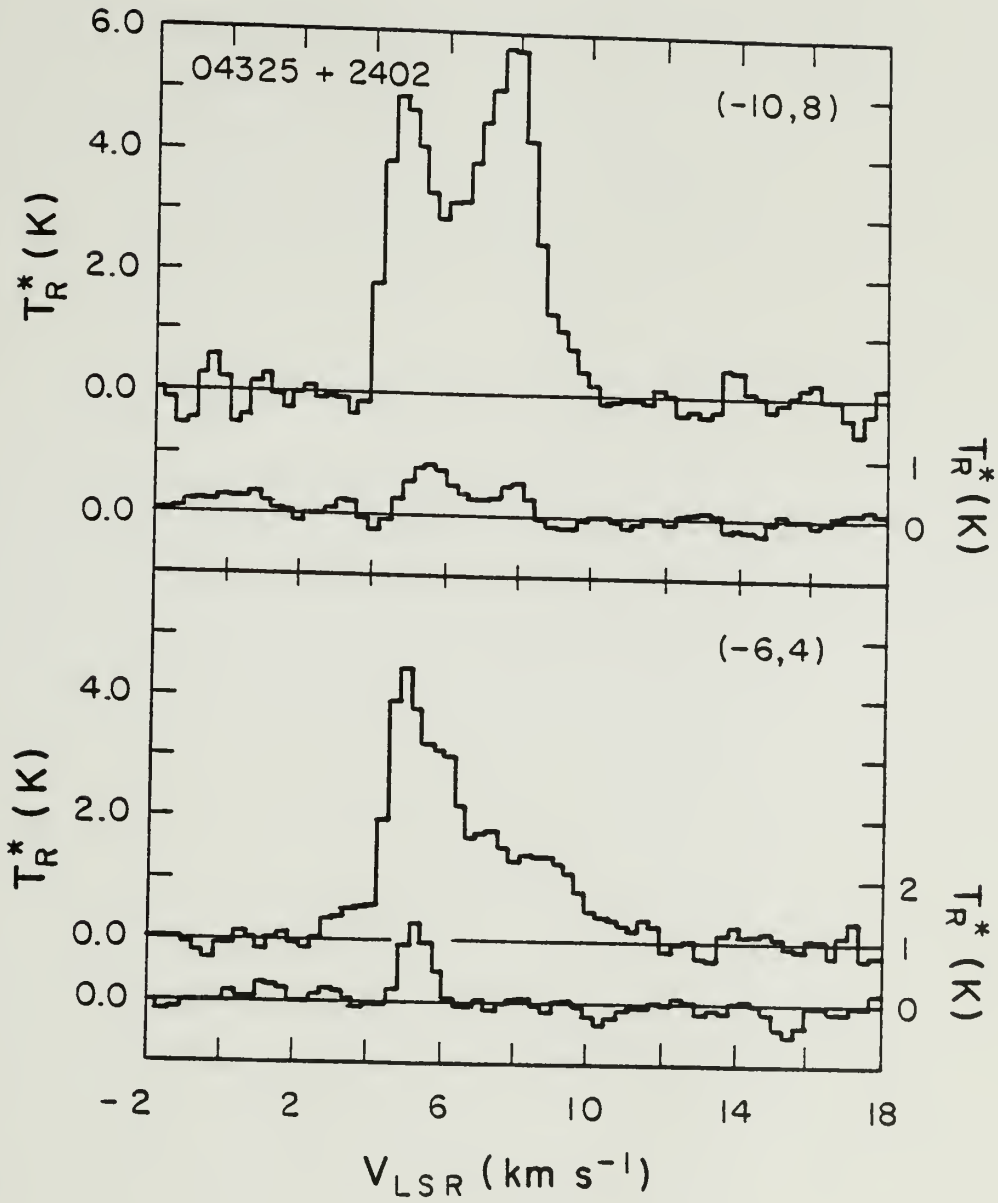
Figure 5. - A sequence of ^{12}CO spectra at positions along the red lobe of high velocity outflow toward 04325+2402. The asymmetric line shape develops into a distinct velocity component in regions 0.2 pc from the star.

Figure 6. - A map of integrated ^{12}CO J=1-0 intensity over the velocity

interval 8.5 to 12 km s^{-1} toward 04325+2402 showing the

spatial extent of the high velocity emission. The outflow

is well collimated over 0.6 pc.
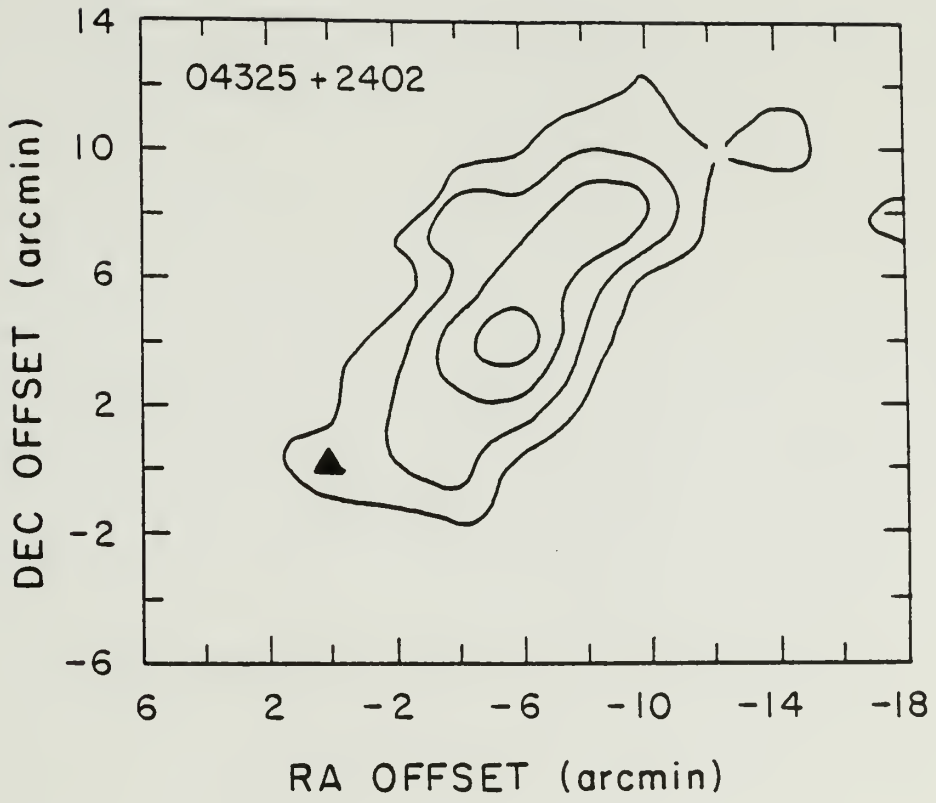
colors are similar to that of a T Tauri star using the criteria of Emerson (1985). This source is presumably responsible for illuminating a cone shaped, optically visible reflection nebula and perhaps indicating that it lies close to the front surface of the cloud.

In Figure 7, we present ^{12}CO and ^{13}CO spectra which show the presence of broad red shifted emission within the velocity interval 8 to 12 km s^{-1}. A map of integrated ^{12}CO J=1-0 wing emission over the velocity of 8 to 12 km s^{-1} comprised of 113 points sampled at 2' spacing is shown in Figure 8. The high velocity gas is dominated by red shifted emission relative to the velocity of the ambient cloud of 6.0 km s^{-1}. Thus, the outflow is characterized by a well collimated, red shifted jet. The red lobe of high velocity emission extends 0.5 pc to the north of the central source. Given the apparent location of the star near the front surface of Heiles Cloud 2, the absence of blue-shifted emission may indicate that the outflow has emerged from the front face of the cloud boundary and has accelerated little molecular material.

(c) Large Scale Expansion of B18

The presence of secondary velocity components as a signature of mass outflow has been previously utilized by Murphy and Myers (1985) to denote the large scale expansion of the B18 cloud. They find a ring of enhanced ^{12}CO J=1-0 line widths centered approximately on the central cluster of T Tauri stars in B18. The size and mass of the ring are 0.8 pc and 140 M_0 respectively. The enhanced line widths are due to the

Figure 7. - ^{12}CO and ^{13}CO spectra toward the peak position of high
velocity emission toward the IRAS source 04369+2539.

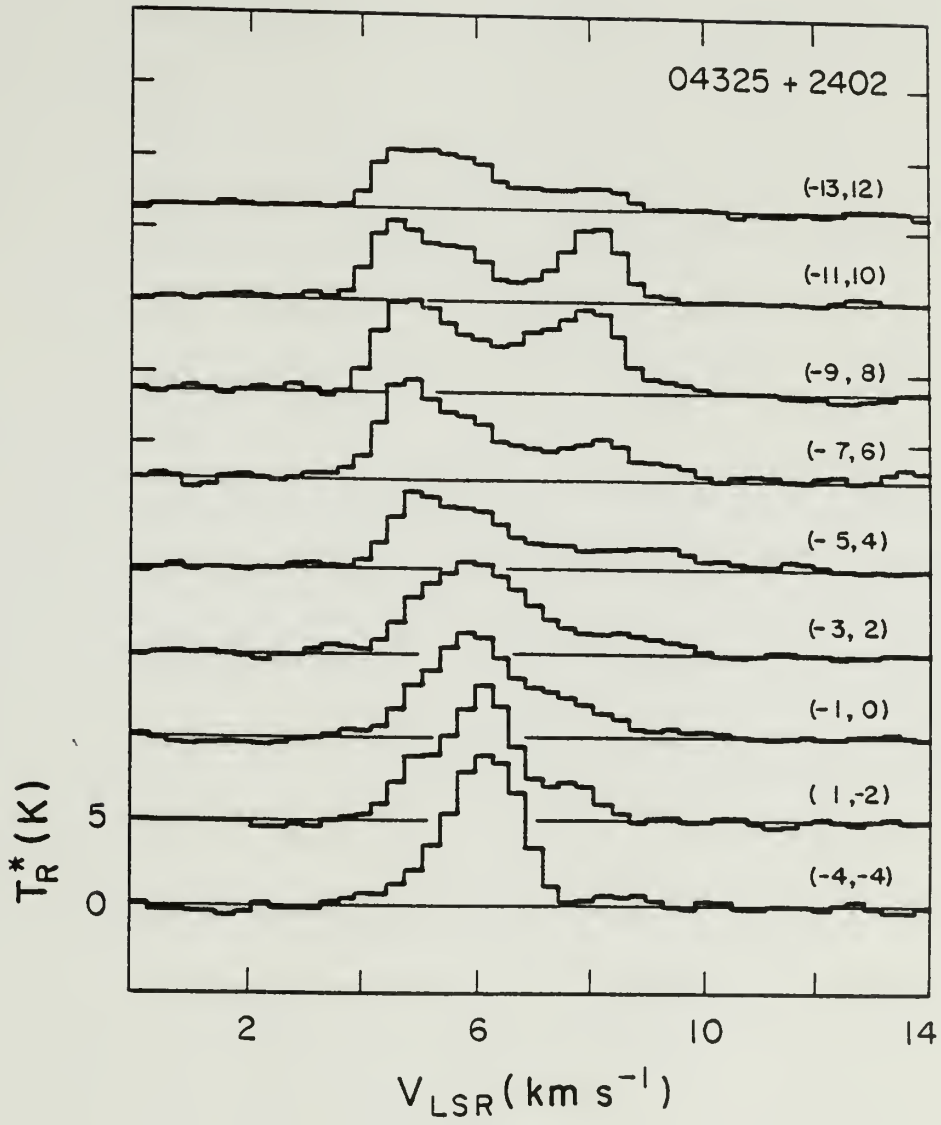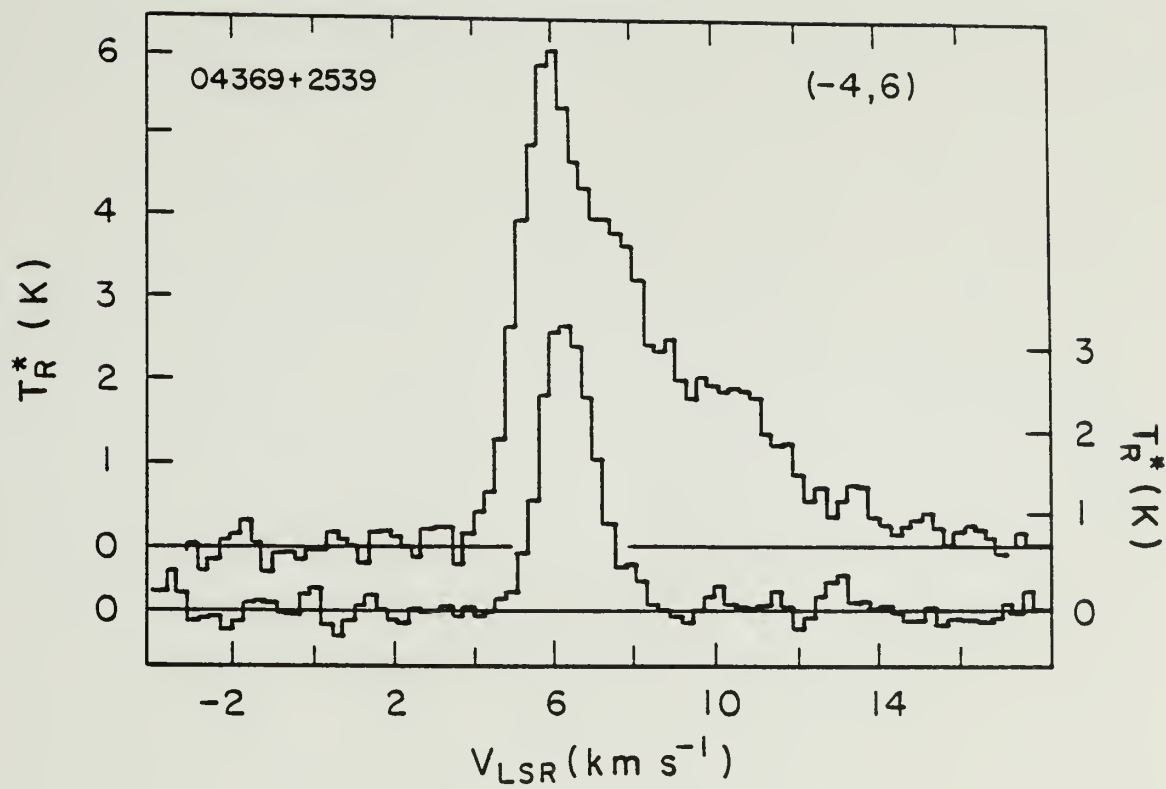Figure 8. - A map of integrated ^{12}CO intensity over the velocity
interval 8 to 12 km s^{-1} of 113 specra, sampled every 2'
toward the IRAS source 04369+2539.
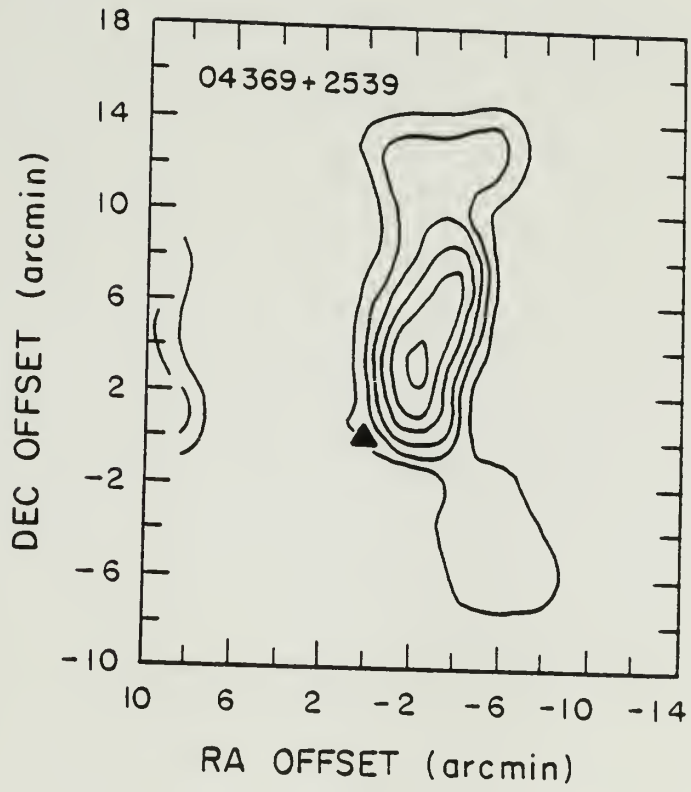
secondary velocity features in the observed ^{12}CO J=1-0 spectra. Murphy and Myers (1985) attribute the observed structure to a shell of swept-up material driven by the stellar winds of the associated T Tauri stars. Thus, the expanding shell and parent cloud are superimposed along the line of sight and are observed kinematically as two distinct velocity components.

From the higher spatial resolution map of ^{13}CO J=1-0 emission of B18, described by Heyer et al. (1986), we confirm the coherent structure of enhanced line width. In Figure 10, we show a map of ^{13}CO J=1-0 line widths toward B18 in which the shaded areas are regions with observed line widths greater than 1.75 km s^{-1} and present representative ^{13}CO J=1-0 spectra from the selected regions within the map. It is shown more conclusively that the line widths are broadened by the presence of multiple velocity components within the velocity range 4 to 7.5 km s^{-1}. While these features are not restricted to the ring, they appear much more prominently near the periphery of the cloud. The mass contained within these secondary velocity features as determined by ^{13}CO emission is 130 M_0 which is a signifcant fraction of the total mass of B18, determined by Heyer et al. (1986) to be 440 M_0. While secondary velocity components are seen toward Heiles Cloud 2 (Schloerb and Snell 1984), there is no evidence for similar coherence of the line widths over its surface.

Figure 9. - A map of ^{13}CO J=1-0 line width of the B18 cloud with

representative spectra from each region. The shaded areas

denote regions with line widths greater than 1.75 km s^{-1}

and form a ring with a radius of 0.8 pc. The line widths

are enhanced due to the presence of secondary velocity

features which may result from the cumulative effect of

several evolved mass outflows from T Tauri stars located

within the cloud boundaries.
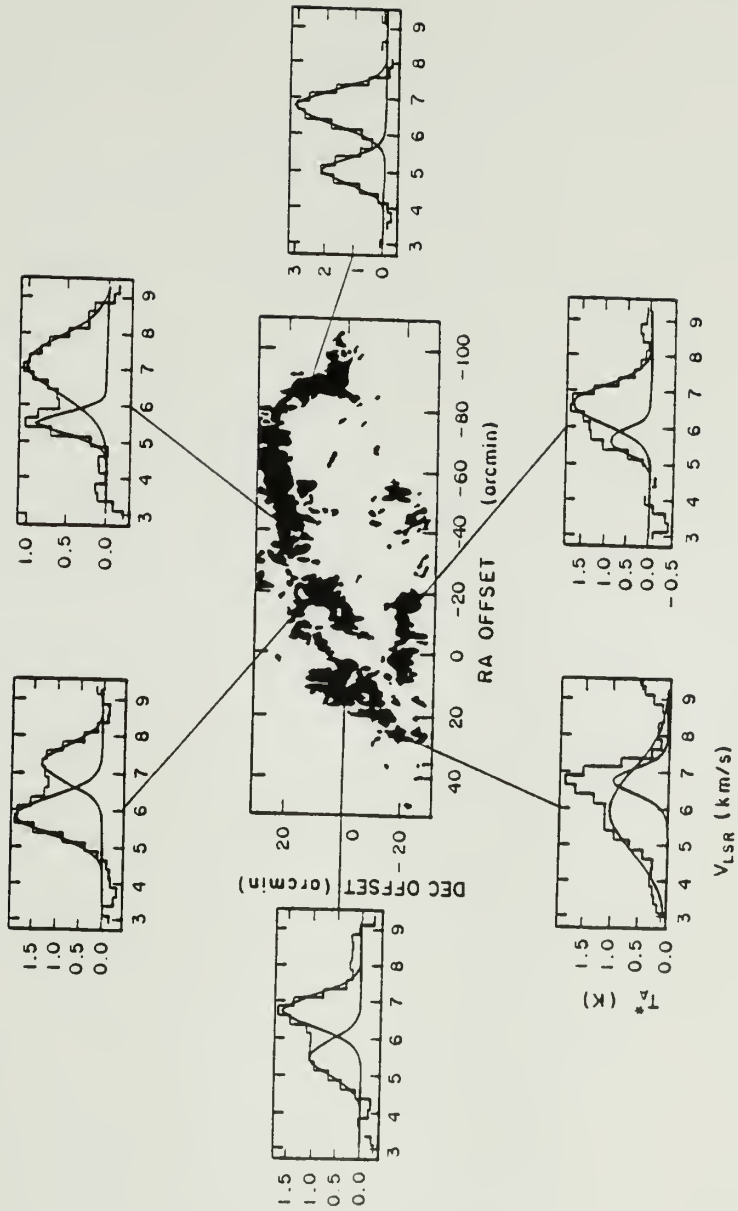
DISCUSSION

From the previous section, we find evidence for mass outflow associated with two T Tauri-like stars and one embedded star within the Taurus molecular cloud. All three outflows are dominated by high velocity red shifted emission. These sources are not associated with optical, shock excited nebulosity seen toward several T Tauri stars in the Taurus Cloud (Mundt and Fried 1983; Strom et al. 1986). The other sources (04381+2540 and 04368+2557) which show peculiar line wing emission (see Figure 1), are also very young objects, based on far infrared colors, that are still embedded within the dense cores from which they condensed. These sources may have associated outflows. In addition, secondary velocity features seen in ^{13}CO J=1-0 emission within the B18 cloud are spatially correlated over the surface of the cloud.

The detection rate of molecular outflows in the present study is small (10%) with respect to a similar survey for high velocity molecular gas associated with dense cores in which 26% of the regions sampled showed evidence for mass outflow (Myers et al. 1986). The stars studied by Myers et al. (1986) are still associated with dense cores from which they formed and presumably are in an early state of pre-main sequence evolution. Most of the young stellar objects sampled in this study are either identified as optical T Tauri stars or emit a far infrared spectrum similar to known T Tauri stars. T Tauri stars are thought to represent a more evolved state of pre-main sequence evolution from their locations toward the low end of convective tracks. Cohen and Kuhi

(1979) find a typical age of T Tauri stars within the Taurus-Auriga complex to be 5×10^5 years. Since mass outflows are short lived ($\sim 10^5$) years and may occur early in the accretion phase of a young stellar object (Heyer et al. 1986), the episode of energetic stellar winds which interact with the ambient material may have long since passed for these stars. Alternatively, the shell of accelerated material typically traced by broad line ^{12}CO emission, may have propagated far from the central star responsible for driving its motion. Our nine point maps (2' spacing) probe gas within only 0.08 pc of the sources in Taurus and would not detect the energetic outflow associated with more evolved young stellar objects. In addition, the velocity of the shell would be very low and difficult to separate from the ambient gas.

We have calculated the energetics of the outflows discovered in our survey in the manner described by Goldsmith et al. (1984) and we summarize the results in Table 3 but have not applied the statistical corrections to account for the projection of the outflows on the plane of the sky. The values of the energetics associated with the outflows detected in this study are intermediate to the values determined of the four other outflows within the Taurus Cloud compiled from the results of previous studies in Table 4 (Schloerb and Snell 1984; Calvet et al. 1983; Edwards and Snell 1982; Myers et al. 1986).

a) Expanding Shells

The wind from a young star is expected to evacuate a cavity within the parent cloud as the wind accumulates ambient gas into an expanding

Table 3

Outflow Properties

Source	M (M_O)	P (M_O kms^{-1})	E (ergs)	$\langle v \rangle$ (kms^{-1})	R (pc)	τ (yr)	F (M_O kms^{-1})	L_{mech} (L_O)	$\mathring{M}_*$ (M_O yr^{-1})
04278+2435	0.04	0.11	3.0×10^{42}	2.8	0.1	3.6×10^{5}	3.1×10^{-6}	0.0007	3.1×10^{-8}
04325+2402	0.06	0.17	5.0×10^{42}	2.8	0.6	1.9×10^{5}	9.0×10^{-7}	0.0002	9.0×10^{-9}
04369+2539	0.28	0.72	2.0×10^{43}	2.7	0.5	1.9×10^{5}	3.8×10^{-6}	0.0008	3.8×10^{-8}

Table 4

Energetics of Taurus Outflow Sources

Source	P (M_O km s^{-1})	E (10^{43} ergs)	$\dot{M}_*$ (10^{-8} M_O yr^{-1})	τ (10^5 yr)	Reference
IRS5-L1551	5.3	30	40	0.8	a
HL Tau	0.003	0.01	6	0.1	b
T Tau	0.38	1.5	10	0.2	c
L1489	0.04	0.1	0.2	1.3	d
04278+2435	0.11	0.3	3	0.4	e
04325+2402	0.17	0.6	0.9	2.0	e
04369+2539	0.72	2.0	4.0	4.0	e
Mean	1.0	5.0	9.0	1.0	

References - a) Schloerb and Snell (1984), b) Calvet et al. (1983), c) Edwards and Snell (1982), d) Myers et al. (1986), e) this study

shell (Castor, McCray, and Weaver 1975). Such a cavity may have been created by the outflowing motions of the stars studied here, accounting for the symmetric, low density environment immediately surrounding ZZ Tau (Heyer et al. 1986). An estimate to the velocity of a spherical shell as it accumulates material from a uniform medium is given by Steigman et al. (1975),

$$v = 6.6 \ (q v_3 \dot{M}_6 / \rho_{24})^{1/4} \ t_6^{-1/2} \quad km \ s^{-1} \tag{1}$$

where v_3 in the wind velocity in units of $10^3 \ km \ s^{-1}$, $\dot{M}_6$ is the stellar mass loss rate in units of $10^{-6} \ M_0 \ yr^{-1}$, ρ_{24} is the mass density of the parent cloud in units of $10^{-24} \ g \ cm^{-3}$, and t_6 is the time in units of 10^6 years. Expected values for these parameters are: $v_3 = 0.5$, $\dot{M}_6 = 0.1$, $\rho_{24} = 3300$. The estimated velocity and radius of the shell after 1×10^5 years are 1.3 km s^{-1} and 0.3 pc respectively. These values are lower limits since less mass is accumulated within the shell if 1) a collimated wind is present or 2) the density of the ambient medium decreases with increasing distance from the star. The distinct high velocity components with velocity offsets greater than 1.5 km s^{-1} from the ambient cloud component seen toward ZZ Tau and 04325+2402 may be due to emission from the shell of swept up material. As the shell accumulates more ambient material with time, its velocity decreases according to equation 1. Moreover, given the space density of young stellar objects within a cloud, the expanding shell associated with a particular young stellar object will have likely collided and coalesced with shells driven by other nearby young stellar objects. Thus, the association of a high velocity feature with one star may not be possible since the shell may shed information to its origin after an interaction.

Such a scenario of expanding shells may then explain the peculiar ring of secondary velocity components found in the B18 cloud within the velocity interval 4 to 7.5 km s^{-1}. The presence of multiple velocity components, separated by only a few km s^{-1} often observed toward molecular clouds are commonly interpreted as two fragments along the line of sight in orbital motion (Clark, Giguerre, and Crutcher 1977). If this is correct, one might expect a random spatial distribution of superimposed fragments and no systematic differences between the two fragments. However, it is unlikely that the presence of multiple velocity components should be coherent over several parsecs and located more prominently toward the periphery of the cloud as seen in Figure 9 if they simply denote fragments along the line of sight. In addition, comparision of the ^{12}CO and ^{13}CO ratio implies that the column densities associated with the secondary velocity features are much smaller than the column densities associated with the ambient cloud velocity component. Probes of high gas density such as emission from NH$_3$ and CS molecules, are generally not detected within the secondary velocity interval (Myers and Benson 1983) indicating low mean densities associated with these regions.

Rather, the interpretation of the ring of secondary velocity components as due to expanding shells first suggested by Murphy and Myers (1985) is consistent with the observed properties. The velocity offset of $\sim$ 1 km s^{-1} from the ambient cloud component is comparable to the velocity expected for a shell accumulating material over a time

scale of 5×10^5 years. An estimate of the mass within the shell accelerated by a spherical stellar wind snowplowing into a medium characterized by a density profile, $n(r) = n_0(r/r_0)^{-\alpha}$ assuming a mean velocity of a shell of 1 km s^{-1} over the observed age τ of the T Tauri star (5×10^5 years) is

$$M_{shell} = \frac{4 \, n_0 r^{\alpha} m_{H_2} \, (v\tau)^{(3 - \alpha)}}{(3 - \alpha)} \tag{2}.$$

The calculated mass accumulated in the shell is 13 M_0 for a uniform medium ($\alpha = 0$), and 154 M_0 for an isothermal sphere ($\alpha = 2$) which may more accurately describe the density of star forming regions. While these values decrease in the liklihood of inefficient acceleration of the ambient cloud or if the medium is inhomogenous, the cumulative effect of several T Tauri stars may account for the 130 M_0 observed within the secondary velocity components in B18. Stahler (1983) has determined a birthline on the HR diagram at which a T Tauri star first becomes visible as a result of stellar winds dispersing the ambient material previously enshrouding the star. Thus, the winds may act as a mechanism to disperse the local dense core from which the star formed as well as to evacuate material between other dense cores within the cloud. Such a dispersal mechanism may account for the enhanced nature of the cores with respect to the ambient cloud in B18 relative to the core enhancement in Heiles Cloud 2 where there are fewer T Tauri stars and no observed large scale expansion (Heyer et al. 1986).

It is important to the subsequent evolution of the cloud whether this large scale expansion will be destructive. Specifically, if the

clouds become unbound, then the typical lifetime of molecular clouds may not exceed 3×10^7 years (Blitz and Shu 1980). The virial mass associated with the expanding motions ($\Delta v = 1.25$ km s^{-1}, R = 0.8 pc), is $M_{virial} = 325$ M_0 and is comparable to the parent cloud mass, 310 M_0 associated with the ambient cloud velocity component. Thus, it is likely that the expanding shell will remain bound to the cloud. In addition, the subcondensations that form within the shell may provide sites of future star formation (Norman and Silk 1980). At present, there is no evidence to suggest that star formation has commenced within the shell. There are only two possible IRAS sources (04239+2436, 04325+2402) whose spectra denote deeply embedded stars (Emerson 1985). However, these sources are located within dense core boundaries whose mean velocities correspond to velocities of the ambient cloud.

b) Stellar Winds as a Source of Turbulent Energy

From virial analyses, it is commonly observed that the gravitational energy of molecular clouds is comparable to the internal energy (thermal, magnetic, and turbulent) determined from the observed line width (Larson 1981; Myers 1983; Heyer et al. 1986). That is,

$$\Delta v_{obs} = (c^2 + v_A^2 + v_{turb}^2)^{1/2} \qquad (3),$$

where c is the sound speed of the medium, v_A is the Alfven velocity, and v_{turb} is the velocity associated with turbulent motion. If most of the internal energy is in the relative supersonic motions between clumps, then this energy is expected to rapidly dissipate in the radiative shocks due to collisions. Scalo and Pumphrey (1983) estimate the time

scale for dissipation to be roughly $7\tau_{ff}$ or $\sim 10^7$ years for the clouds studied here. Without a source to replenish this lost energy, collapse of the interstellar cloud may result.

In this study, we have investigated the role of stellar winds as an energy source to support the cloud against its self gravitational force. Since the Taurus Molecular Cloud Complex is in approximate virial equilibrium, we can estimate the internal energy from the gravitational energy associated with the complex determined by Kleiner and Dickman (1984) to be 1.5×10^{47} ergs. If this energy is dissipated in 10^7 years, then the rate of energy loss, $L_{diss} = 0.13\ L_0$. From Table 4, we have calculated the mean energy of an individual outflow to be 1.4×10^{44} ergs. This value is weighted toward the highly energetic outflow associated with the infrared source IRS5-L1551. The mean dynamical time scale of the seven Taurus outflows is 6×10^4 years. We note that the mean values for the outflow energy and time scale have been corrected for the projection of the flow in the plane of the sky. Thus, we calculate the energy injection rate, L_{in} from stellar winds to be $0.02\ L_0$. The number of outflows, N, required at any one time to replenish the energy lost to the cloud by radiative collisions is given by $N = L_{diss}/L_{in} = 6.5$. Thus, it is plausible that the number of outflow sources presently seen in the Taurus Cloud is sufficient to maintain the internal energy of the cloud and can provide a significant contribution to the overall internal energy budget of a molecular cloud.

It is not clear how this energy is ultimately distributed within the cloud and reflected in the observed line widths. Since the kinetic

temperatures do not, in general, show any significant local enhancement near the outflowing regions, it is unlikely that the energy is deposited into the thermal reservoir of the cloud. Norman and Silk (1980) suggested that the shells driven by the stellar winds eventually intersect with expanding shells driven by other nearby pre-main sequence stars and that the observed line widths are a superposition of these coagulated structures along the line of sight. Alternatively, the expanding shells of accelerated material may transfer energy to the local magnetic field which would tend to excite magnetosonic wave motion (Arons and Max 1975). Shu and Tereby (1983) have noted that any internal turbulent motion within the cloud must be wavelike to account for the uniform direction of observed polarization vectors which describe the magnetic field geometry. The magnetic energy induced by the stellar winds may be reflected in the line widths of the ambient cloud velocity component but is not observed as high velocity wing ^{12}CO emission. Given the apparent magnetic evolution of the Taurus clouds (Heyer et al. 1986), such an interpretation is appealing but must await more detailed studies of the coupling between the expanding shell and magnetic field. We note that stellar winds can not be the only energy source since there are examples of molecular clouds (L134, Swade et al. 1986) in which no star formation is occuring but whose molecular line widths are still supersonic. For these clouds, the source of energy is likely to be external.

CONCLUSION

From a sample of thirty far infrared point sources, selected from the IRAS Point Source Catalog (1985), we have searched for evidence of mass outflow using the ^{12}CO J=1-0 emission to trace the accelerated ambient cloud material. In general, there are complex line shapes and peculiar ^{12}CO to ^{13}CO ratios. We find evidence for mass outflow toward three far infrared point sources, two of which are identified as T Tauri-like based on far infrared colors. The three outflows are dominated by red shifted emission, typically 3 km s^{-1} offset from the ambient cloud velocity indicative of monopolar morphologies. The energies of the new outflows are calculated and found to be intermediate to those of other outflows present within the Taurus Cloud. We estimate that the stellar winds presently occurring within the cloud can provide a significant fraction of the cloud's energy reservoir. We also find evidence for the large sale expansion of the B18 cloud from a detailed map of ^{13}CO J=1-0 emission, presumably driven by previous energetic winds of the T Tauri stars present within the cloud.

CHAPTER IV.
SUMMARY AND PERSPECTIVES

The three previous chapters have discussed several interstellar processes which may dominate distinct sequences in the evolution of a molecular cloud leading to the formation of a star. In Chapter II, from large scale maps of the gas distribution and kinematics and the magnetic field geometry, we have studied regions characterized by mean densities, 10^3 cm^{-3}, and which likely reflect the long term evolution of the clouds based on the crossing time scales. In addition, by studying several clouds, we have found distinctions between clouds which may result from differences in the evolutionary state of these regions. In Chapter III, we investigated the properties of dense core regions which are characterized by small (0.1 pc) sizes and larger mean densities (> 10^4 cm^{-3}) relative to those regions studied in Chapter II. In many of these regions star formation has already occured based on their association with an IRAS point source but all are probable sites of star formation within the next 5×10^5 years. Finally, post star-formation processes such as energy feedback to the cloud from stellar winds are discussed in Chapter IV. With the results of these investigations, we can speculate upon the evolutionary scenario for the Taurus Molecular Cloud.

From the large scale but coarsely sampled maps of ^{13}CO J=1-0 emission of the Taurus Complex by Kleiner and Dickman (1984) and the

preliminary results of similar HI 21 cm observations (Dickman, private communication), it appears likely that the influence of the magnetic field was significant in the early phases of the cloud when it was composed primarily of atomic gas given the orientation of the HI distribution relative to the magnetic field direction. In addition, the size scale (14 pc) which represents the separation between atomic gas clumps is similar to the characteristic spacing between the molecular clouds which suggests that the parent clouds studied here (Heiles Cloud 2, B216-B217, B18, L1517, L1544) are a result of the fragmentation of an atomic gas cloud. The gas within these individual fragments is subsequently converted into the molecular phase as the fragments further condense.

The results of Chapter II suggests that these parent clouds are subject to the magnetic stress based on the flattened morphologies and systematic alignment of the minor and rotational axes along the magnetic field direction. As the stress of the magnetic field becomes diluted in time, external perturbations such as cloud collisions, become more efficient as mechanisms to reorient the cloud's axes as seen in B18 where the observed alignment is not so sriking as that of the other clouds. Each of the parent clouds exhibit evidence for subfragmentation although it can not be conclusively determined here whether these core regions are a direct consequence of ambipolar diffusion or a result of a gravitational instability in response to an external perturbation. From the observed line widths and spatial extent of the ^{13}CO J=1-0 emission

from the clouds, these regions exhibit an equilibrium between self gravitational forces and internal, non-thermal pressure. Thus, the parent clouds are expected to be long lived with respect to the free fall collapse time of 10^6 years.

In Chapter III, we investigated the role of the magnetic field in the subcondensations within the parent clouds. The dense core regions do not exhibit systematic alignment of their orientations and rotational axes as seen in the lower density, parent clouds. Thus, we have established that one need not include the stress of the magnetic field when considering the dynamics of the gas at densities greater than 10^4 cm^{-3}. The inevitable collapse of the dense core to form a protostar is moderated only by thermal or subsonic pressure and the centrifugal stress.

Given the decoupling of the magnetic field from the gas in the denser regions and its reduced influence in time on the parent clouds, the fate of the molecular cloud beyond the magnetic flux diffusion time scale (10^7 years) is dependent on the ability of other forces to counteract self-gravity. In Chapter IV, the role of stellar winds as a source of turbulent energy is discussed. Three additional outflows were detected from our survey of the local ^{12}CO J=1-0 emission toward IRAS far infrared point sources. The energies of the stellar winds can provide a significant contribution to the cloud's internal energy reservoir. If this energy is efficiently converted into random motions or tubulence, then the collapse of the cloud may be inhibited. These

stellar winds from newborn stars also act as a mechanism to disperse the low density, interfragment gas. After 5×10^5 years, the interfragment gas that has accumulated within a shell, may be observed as a distinct velocity component as seen in the map of ^{13}CO line widths of B18. These swept up shells may provide sites of future star formation as the densities within the shell increase inducing a self-regulated rate of star formation within the cloud (Norman and Silk 1980).

The evolutionary scenario just described is consistent with the observed properties of the Taurus Molecular Cloud but may not provide a unique interpretation. It is dangerous to extrapolate the results of an individual region to a universal conclusion given the wide spectrum of properties presented to us by the interstellar medium. The Taurus Cloud is likely to be representative of low mass star forming regions but the proposed evolutionary model may not be applicable to giant molecular clouds where high mass star formation occurs. It is these regions of massive star formation which trace the spiral structure of external galaxies and whose evolution need be determined in the future in order to provide a complete picture of the star formation process.

APPENDIX

Comparison of ^{13}CO Integrated Intensity and Visual Extinction

Star counts have been made of the regions surrounding the two
relatively isolated Taurus clouds L1544 and L1517. These star counts
can be used to estimate the visual extinction within these clouds which
then can be compared with our ^{13}CO observations to determine the
relationship between integrated intensity and total gas column density.
Star counts were made in each cloud over an area 67'x 67' using the POSS
red prints in a reseau with a resolution of 2.24'x2.24'. To improve
statistics, the star count data were co-added in blocks of 4 reseau
elements to provide a final resolution of 4.5'x4.5'. The reduction of
the star counts from the red POSS prints to visual extinction is
described in detail by Dickman (1978). The red extinction (A_R) can be
derived from the star counts in the target field (n) and the star counts
in a reference field (n_{ref}), assumed to be free of extinction, using the
following relation from Dickman (1978):

$$A_R = b^{-1} \log(n_{ref}/n), \qquad\qquad (A1)$$

where b is the slope of the roughly linear relation between the
logarithm of the total number of stars and the limiting magnitude.
This latter relation is taken from van Rhijn (1929) based on his star
counts to photographic magnitude 18. We must assume that van Rhijn's
sequences can be extrapolated to our limiting counting magnitude from
the red POSS prints of 19.5 and that the slope of the van Rhijn
sequences is appropriate for our red star counts. The van Rhijn

sequence is extremely linear so that our extrapolation to magnitude 19.5 seems reasonable safe. We have fitted van Rhijn's star counts for $b^I = -10°$ and $l^I = 40°$ (old galactic coordinates) to determine a value of $b = 0.364$. Thus, red extinctions can be derived using the star counts in the target field, the star counts in several reference regions which surround L1544 and L1517 that have been selected to determine the unextincted star density, and the slope of the van Rhijn sequence. Finally, to determine the visual extinctions within these clouds the measured red extinctions must be corrected for the ratio of red to visual extinction; we have used the relation: $A_v = 1.21 \ A_R$ (Dickman 1978).
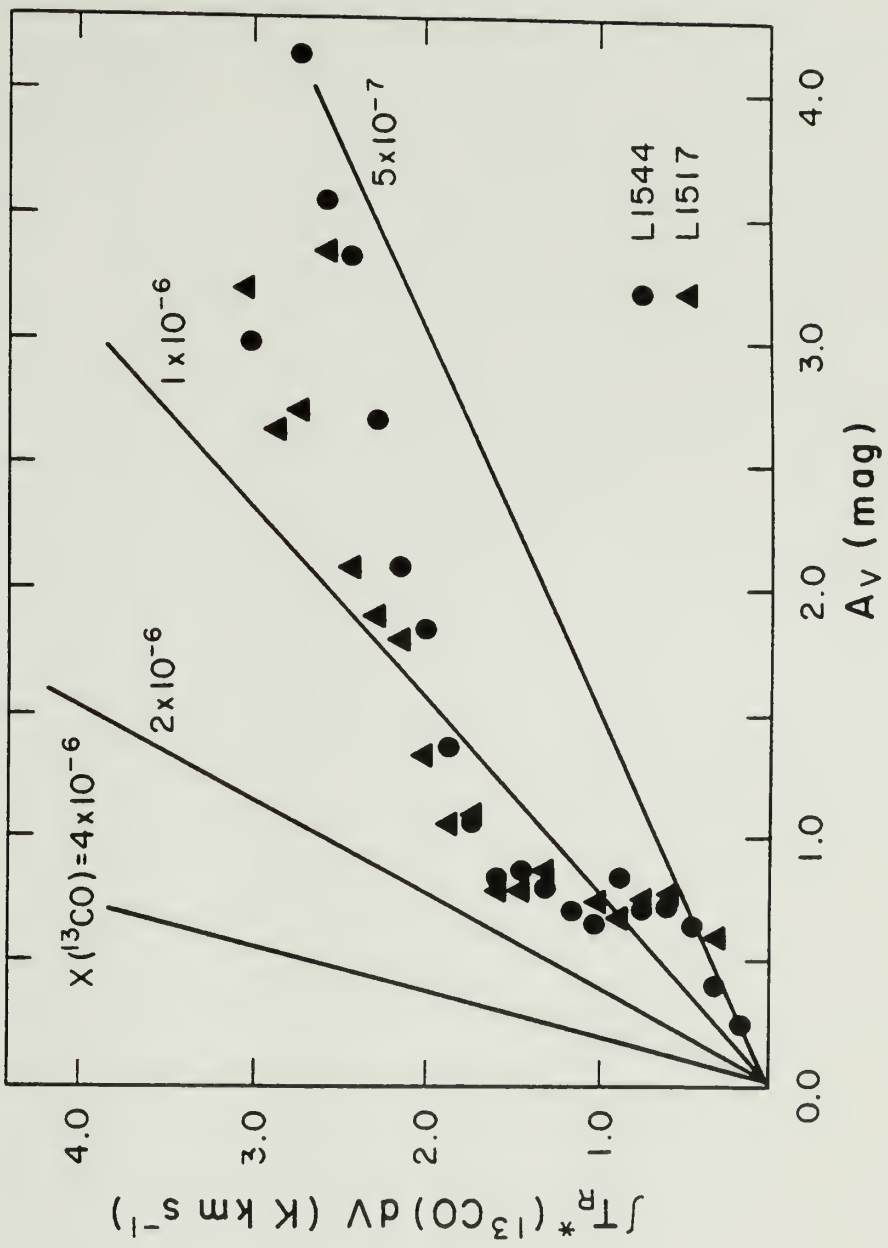
The ^{13}CO integrated intensity data has also been averaged and sampled at the same resolution and locations as the star count data. Based on these data a comparison can be made of the visual extinction and integrated intensity. Though the integrated ^{13}CO intensity is well determined within the 4.5'x4.5' regions (roughly 20 spectra go into these averages), the visual extinction is not as well determined and there is a large uncertainty in A_v primarily due to the statistical errors in the star counts (Dickman 1978). In fact, the uncertainty in the visual extinction due to counting statistics alone in the unextincted regions where the star counts are the largest is 0.7 magitudes. The uncertainty in the visual extinction becomes larger in regions of greater extinction where the star density is lower. Therefore, to determine the relationship between A_v and integrated

intensity more accurately we have separately binned the data for L1544 and L1517 in small intervals of integrated intensity and averaged over all values of the visual extinction. Thus due to the large number of individual measurements, we can better define this relation. The data so binned is presented in Figure A1 and show that the relationship between A_v and ^{13}CO integrated intensity is similar for both clouds. A simple relationship between these two parameters is given by:

$$A_v = 0.77 \int T_R^*(^{13}CO) \, dv.$$

In the text, we have estimated the total ^{13}CO column density using the formula given by Schloerb and Snell (1984) which assumes that the ^{13}CO emission is optically thin and that the rotational levels are populated in LTE at 10 K. Using our relation between A_v and integrated intensity and the relation found by Bohlin, Savage, and Drake (1978) between $E(B-V)$ and the total hydrogen column density, we can can estimate that the factor needed to scale the ^{13}CO column densities to total molecular hydrogen column densities is roughly 10^6. If our ^{13}CO column densities were accurate, the fractional abundance of ^{13}CO relative to H_2 would be 10^{-6}. Lines of various "fractional abundances" have been indicated in Figure A1. Caution must be taken in literally interpreting these values as abundances, since the column densites have been derived using a number of assumptions that are almost certainly not correct. Though, we have concluded earlier that the ^{13}CO emission toward most lines of sight is optically thin, it is unlikely that all lines of sight are in LTE at 10 K. In fact, the strong ^{13}CO emission at

Figure A1 - A plot of the integrated ^{13}CO J=1-0 intensity versus the
visual extinction determined from star counts. We estimate
the conversion factor between ^{13}CO column density and H_2
column density is 10^{-6}.

$X(^{13}CO) = 4 \times 10^{-6}$

2×10^{-6}

1×10^{-6}

5×10^{-7}

L1544

L1517

A_V (mag)

$\int T_R^* (^{13}CO) \, dV \, (K \, km \, s^{-1})$

small values of A_v may be due to a larger fraction of the population in lower lying rotational states than that at higher values of A_v. However, the most important result of our analysis is the relationship between integrated ^{13}CO intensity and total molecular hydrogen column density which is independent of our ability to derive either ^{13}CO column densities or the fractional abundance of ^{13}CO. We find that over the range in integrated intensity of 1 to 3 K km s^{-1} (which includes most of the data for the Taurus clouds studied) there is a roughly linear relation between integrated intensity and total molecular hydrogen column density and, thus, our total gas column densities and masses for the Taurus clouds should be reasonably accurate.

BIBLIOGRAPHY

Allen, D.A. 1972, Ap. J. Letters, 172, L55.

Allen, D.A. and Penston, M.V. 1975, MNRAS, 172, 245.

Allen, M. and Robinson, G.W. 1976, Ap. J., 207, 745.

Arons, J. and Max, C.E. 1975, Ap. J. Letters, 196, L77.

Arquilla, R.A. and Goldsmith, P.F. 1986, Ap. J., 303, 356.

Bash, F.N., Green, E., and Peters, W.L. 1977, Ap. J., 217, 464.

Batrla, W. Wilson, T.W., and Rahe, J. 1983, Astron. and Astrophys., 96, 202.

Baudry, A., Cernicharo, J., Perault, M., de la Noe, J., and Despois, D. 1981, Astron. and Astrophys., 104, 101.

Bohlin, R.C., Savage, B.D., and Drake, J.F. 1978, Ap. J., 224, 132.

Boss, A.P. 1980, Ap. J., 237, 866.

Blitz, L. and Shu F.H. 1980, Ap. J., 238, 148.

Calvet, N., Canto, J., and Rodriguez, L.F. 1983, Ap. J., 268, 739

Cassen, P. Shu, F.H., and Tereby, S. 1985, in Protostars and Plants II, eds. D.C. Black, and M.S. Matthews, (Tuscon: University of Arizona Press), p.90.

Castor, J., McCray, R., and Weaver, R. 1975, Ap. J. Letters, 200, L107.

Cernicharo, J., Guelin, M., and Askne, J. 1984, Astron. and Astrophys., 138, 371.

Cernicharo, J., Bachiller, R., and Duvert, G. 1985, Astron. and Astrophys., 149, 273.

Clark, F.O., Giguerre, P.T., and Crutcher, R.M. 1977, Ap. J., 215, 511.

Clark, F.O. and Johnson, D.R. 1978, Ap. J., 220, 500.

Cohen, M. and Kuhi, L.V. 1979, Ap. J. Suppl., 41, 743.

Crutcher, R.M. 1973, Ap. J., 185, 857.

Davis, L. Jr. and Greestein, J.L. 1951, Ap. J., 114, 206.

Dickman, R.L. 1978, Ap. J. Suppl., 37, 407..

Dickman, R.L. and Clemens, D.P. 1983, Ap. J., 271, 143.

Dickman, R.L. and Kleiner, S. 1985, Ap. J., 295, 479.

Dickman, R.L. 1985, in Protostars and Planets II, eds. D.C. Black and
    M.S. Matthews, (Tuscon: University of Arizona Press), p. 150.

Edwards, S. and Snell, R.L. 1982, Ap. J., 261, 151.

Elias, J.H. 1978, Ap. J., 224, 857.

Elmegreen, B.G. 1979, Ap. J., 232, 729.

Emerson, J.P. 1985, in Star Forming Regions, eds. M Peimbert and
    J. Jugaka, (D. Reidel)

Falgarone, E. and Puget, J.L. 1986, Astron. and Astrophys., 162, 235.

Fleck, R.C. 1981, Ap. J., 246, L151.

Gaida, M., Ungerechts, H., Winnewisser, G. 1984, Astron. and Astrophys.,
    137, 17.

Goldreich, P. and Kwan, J. 1974, Ap. J., 189, 441

Goldsmith, P.F. and Sernyak, M.F. 1984, Ap. J., 283, 140.

Goldsmith, P.F., Snell, R.L., Hemeon-Heyer, M., and Langer, W.D. 1984,
    Ap. J., 286, 599.

Goldsmith, P.F., Langer, W.D., and Wilson, R.W. 1986, Ap. J. Letters,
    303, L11.

Graedel, T.E., Langer, W.D., Frerking, M.A. 1982, Ap. J. Suppl., 48,

321.

Hartmann, L. and MacGregor, K.B. 1982, Ap. J., 259, 180.

Hartmann, L., Hewett, R., Stahler, S., Mathieu, R., 1986, submitted to
    Ap. J.

Heiles, C. and Katz, G. 1976, A.J., 287, 200.

Henrikson, R.N. and Turner, B.E. 1984, Ap. J., 287, 200.

Herbig, G.H. and Rao, N.K. 1972, Ap. J., 174, 401.

Heyer, M.H., Vrba, F.J., Snell, R.L., Schloerb, F.P., Strom, S.E.,
    Goldsmith, P.F., and Strom, K.M. 1986, submitted to Ap. J.

Heyer, M.H. 1986, submitted to Ap. J.

Heyer, M.H., Snell, R.L., Goldsmith, P.F., Strom, S.E., and Strom, K.M.
    1986, Ap. J., in press.

Hsu, J.-C., 1985, Ph.D. thesis, University of Texas.

IRAS Point Source Catalog 1985, Joint IRAS Science Working Group,
    (Washington, D.C.: U.S. Government Printing Office).

Kleiner, S. and Dickman, R.L. 1984, Ap. J., 286, 255.

Kleiner, S. and Dickman, R.L. 1985, Ap. J., 295, 466.

Kraft, R.P. 1970, in Spectroscopic Astrophysics, ed. G.H. Herbig,
    (Berkeley: University of California Press), p. 385.

Kutner, M.L. and Ulich, B.L. 1981, Ap. J., 250, 341.

Kwan, J. 1979, Ap. J., 229, 567.

Kwan, J. and Sanders, D.B. 1986, Ap. J., in press.

Larson, R.B. 1981, MNRAS, 194, 809.

Magahles, M., Benedetti , E., and Roland, E.H. 1984, PASP, 96, 383.

Menten, K.M., Walmsley, C.M., Krugel, E., and Ungerechts, H. 1984,

Astron. and Astrophys., 137, 108.

Mestel, L. and Spitzer, L. 1956, *MNRAS*, 416, 503.

Mestel, L. 1977, in *Star Formation*, eds. T de Jong and A. Maeder, (Dordrecht: D. Reidel), p. 213.

Moneti, A. Pipher, J., Helfer, H.L., McMillan, R.S., and Perry, M.L. 1984, *Ap. J.*, 282, 508.

Mouschovias, T. Ch. 1976, *Ap. J.*, 207, 141.

Mouschovias, T. Ch. 1977, *Ap. J.*, 211, 147.

Mouschovias, T. Ch. and Paleologou, E.V. 1980, *Ap. J.*, 237, 877.

Mouschovias, T. Ch. and Paleologou, E.V. 1981, *Ap. J.*, 246, 48.

Mouschovias, T. Ch. and Morton, S.A. 1985, *Ap. J.*, 298, 205.

Mundt, R. and Fried, J.W. 1983, *Ap. J. Letters*, 274, L59.

Murphy, P.C. and Myers, P.C. 1985, *Ap. J.*, 298, 818.

Myers, P.C. and Benson, P.J. 1983, *Ap. J.*, 266, 309.

Myers, P.C. 1983, *Ap. J.*, 270, 105.

Myers, P.C. 1985, in *Protostars and Planets II*, eds D.C. Black and M.S. Matthews, (Tuscon: University of Arizona Press), p. 81.

Myers, P.C., Heyer, M.H., Snell, R.L., and Goldsmith, P.F. 1986, *Ap. J.*, in preparation.

Norman, C.A. and Silk, J. 1980, *Ap. J.*, 238, 158.

Scalo, J.M. and Pumphrey, W.A. 1982, *Ap. J. Letters*, 258, L29.

Scalo, J.M. 1985, in *Protostars and Planets II*, eds D.C. Black and M.S. Matthews, (Tuscon: University of Arizona Press), p. 201.

Schloerb, F.P., Snell, R.L., and Young, J.S. 1983, *Ap. J.*, 267, 163.

Schloerb, F.P. and Snell, R.L. 1984, *Ap. J.*, 283, 129.

Schneider, S. and Elmegreen B.G. 1979, Ap. J. Suppl., 41, 87.

Shu, F.H. 1983, Ap. J., 273, 202.

Shu, F.H. and Tereby, S. 1983, in Workshop on Cool Stars, Stellar Systems, and the Sun, eds. S. Balinus and Hartmann, L., (Berlin: Springer-Verlag), p.90.

Snell, R.L., Loren, R.B. and Plambeck, R.L. 1980, Ap. J. Letters, 239, L17.

Snell, R.L. 1981, Ap. J. Suppl., 45, 121.

Snell, R.L., Schloerb, F.P., Young, J.S., Hjalmarson, A., and Friberg, P. 1981, Ap. J., 244, 45.

Snell, R.L. and Schloerb, F.P. 1985, Ap. J., 295, 490.

Spitzer, L. 1978, Physical Processes in the Interstellar Medium, (New York: Wiley), p. 295.

Stahler, S.W. 1983, Ap. J., 274, 822.

Steigman, G., Strittmatter, P.A., and Williams, P.E. 1975, Ap. J., 198, 575.

Strom, K.M., Strom, S.E., Wolff, S.C., Morgan, J., and Wenz, M. 1986, submitted to A.J.

Swade, D.A., Schloerb, F.P., Snell, R.L., and Goldsmith, P.F. 1985, in Masers, Molecules, and Mass Outflows, ed A.D. Haschick, p. 73.

Tereby, S., Shu, F.H., and Cassen, P. 1984, Ap. J., 286, 529.

van Rhijn, P.J. 1929, Gronigen Pub., Vol 43.

Vanden Bout, P.A., Loren, R.B. Snell, R.L., and Wootten, A. 1983, Ap. J., 271, 161.

Vogel, S.N. and Kuhi, L.V. 1981, Ap. J., 245, 960.

Vrba, F.J., Strom, S.E., and Strom, K.M. 1976, A.J., 81, 958.

Young, J.S., Langer, W.D., Goldsmith, P.F., and Wilson, R.W. 1982,
Ap. J. Letters, 251, L81.

Zuckerman, B. and Evans, N.J. 1974, Ap. J. Letters, 192, L149.

Zweibel E.G. and Josafatsson, K. 1983, Ap. J., 270, 511.